Supplemental Material to "Why is Chemical Synthesis and Property Optimization Easier than Expected?"

Katharine W. Moore, Alexander Pechen, Xiao-Jiang Feng, Jason Dominy, Vincent J. Beltrani and Herschel Rabitz
Department of Chemistry, Princeton, NJ, 08544

This document presents the results found in the literature that give chemical synthesis or property fitness landscapes (not including those discussed in the main work), along with a brief description of the target objective and variables employed. The studies are grouped by objective target, in accordance with the tables in the main paper.

Some basic aspects of the generally expected trap-free fitness landscape behavior must be reiterated before examining the reported results in the literature. Fundamentally, all chemical optimization problems have an infinite-dimensional variable space. Choosing any finite set of variables (as is done in any practical application) inherently constrains the search space to some finite-dimensional portion of the full infinite-dimensional space. As the trap-free fitness landscape conclusion of OptiChem theory rigorously holds only if no constraints are placed on the variables, it may be expected that finding traps in highly constrained experimental chemical fitness landscapes would be the norm. Physical limitations such as solubility limits of reagents or phase transitions of solid state materials may also limit the range of the accessible variables. Processing conditions also play an important role in the fitness landscape. As a most extreme example, a study of epoxidation catalytic activity found entirely different fitness landscapes for the *same* ternary metal alloy library, depending on the method used to synthesize the library (Figure 1) [1]. Depending on the processing procedure, the optimal regions of the three landscapes (a), (b), and (c) shown in Figure 1 are at different compositions of the material. Additionally, the finite sampling resolution of experimental fitness landscapes may obscure landscape features, possibly including traps. The issue of finding a local maximum, instead of the global maximum, also lies in the background. For reaction control, the global maximum is at 100% yield, but most studies do not fully achieve this value, yet the results are considered successful. Where available, the absolute yield, and comparison to other literature results by the original authors, is reported here; we assume that a high ($\geq 80\%$) yield constitutes the global maximum. For chemical property objectives, the theoretical maximum objective value is generally not known, so it is not possible to affirm whether the global maximum has been found. Finally, for cases where the highest reported yields occurs at the boundary of a variable's domain, expanding the domain of exploration may further improve the yield.

Despite these practical limitations on finding trap-free landscapes in chemical optimization problems, the overwhelming observation is that the vast majority of the fitness landscapes reported in the literature are, in fact, trap-free. A few exceptions have been found, and are discussed below as they arise. In some cases, the quality of the graphical reproductions is less than ideal, and the specific cited figures can be found in the indicated references.

1 Synthesis: Optimization of Reaction Conditions

The optimization of reaction conditions for a particular synthetic target is a common goal in chemistry; these studies often employ methods such as response surface methodology and factorial design to produce fitness landscapes using concentrations of reagents and processing conditions such as temperature and reaction time as variables. Generally, the reported fitness landscape surfaces are interpolated from a small number of experimental data points using a polynomial fit. Polynomial fitted landscapes can

identify traps, provided that the polynomials are third-order or higher. Thus, in examining fitted fitness landscapes, we only consider studies that employed higher-order polynomial fits or performed direct interpolation of the recorded data points to obtain landscapes. With the one possible exception discussed in the main work, however, all observed fitness landscapes are trap-free. A sampling of such surfaces is presented below, but the literature contains many more studies that report trap-free landscapes (although many use only second-order polynomials for fitting). Further examples in a variety of fields can be found in the references cited in the review articles [2, 3, 4, 5, 6]. The optimization of reaction conditions using such response methods is often achieved in ∼100 experiments or fewer; some studies report the number of experiments required, as described below.

1.1 Optimization of Organic Synthesis Reactions

Two studies compiled rate data for product formation from which we constructed fitness landscapes. The rates were measured for the hydrolysis of substituted phenyl benzoates with varying substituents on the two phenyl rings (X and Y, shown in Figure 2) as variables [7]. The hydrolysis rate was found to correlate to the donor character of the substituents (i.e., the Hammett constant as a chemometric), as shown in Figure 2. Another study compiled rate data for nucleophilic substitution of CH_3-X (X=F, Cl, Br, I) with various nucleophiles [8]. The resulting fitness landscape is trap-free (Figure 3), but displays the interesting trend in reactivity for the substrate leaving group X, with Br>I>Cl>F, which does not follow the general nucleophilicity rule I>Br>Cl>F. The authors comment that the rate behavior is "not in a well-behaved halogen sequence... in spite of the fact that the halogens form one of the most regular series in the periodic table" [8]. In this case, the nucleophilicity chemometric does *not* determine the reaction rate; this result shows that the reaction follows a more complicated mechanism [8].

The asymmetric sulfoxidation of an aryl ethyl sulfide in high enantioselectivity was optimized in 16 experiments [9] using concentrations of titanium isopropoxide and diethyl-*D*-tartrate as variables. The objective was reported as the excess percentage of the desired enantiomer, and the experimental data points are plotted in Figure 4. Although no surface fit was explicitly made to these data points, the landscape is evidently trap-free with a maximal region at 90% e.e.

A Mizoroki-Heck reaction to produce 3-phenyl cinnamaldehyde was optimized using Pd catalyst concentration and solvent volume (i.e., dilution of reagents) as variables [10]. The temperature was also varied, but not shown in the response surface. The resulting surface has a large optimal region (i.e., a level set), as shown in Figure 5. Optimization was accomplished in 30 experiments, with 99% maximal yield.

The synthesis of mitosis inhibitor monasterol was optimized in 29 experiments [11]. The variables were temperature, reaction time, and catalyst $LaCl_3$ concentration. The resulting fitness landscapes with temperature and reaction time as variables are shown for (a) conversion to product and (b) product purity in Figure 6. The fitness landscapes with respect to temperature and catalyst concentration are shown in Figure 7. Interestingly, for both sets of variables, there are level sets of optimal conditions (the red areas in Figure 8). The absolute yield at these conditions was 95%, representing essentially the global optimum.

Optimization of the oxidative coupling of methane was performed [12]. The observables consisting of $C_2{}^+$ yield (i.e., hydrocarbons of C_2 or greater), $C_2{}^+$ selectivity, and ethylene:ethane ratio produced were optimized using as variables the temperature, CH_4/O_2 ratio, dilution ratio (solvent content), gas hourly space velocity (GHSV) of CH_4, and pretreatment time of Na-W-Mn/SiO_2 catalyst. All resulting fitness landscapes are trap-free. The observable ethylene:ethane ratio is shown as a function of temperature and CH_4/O_2 ratio and as a function of GHSV and the dilution ratio in Figures 9 and 10, respectively. $C_2{}^+$ selectivity is shown as a function of GHSV and catalyst pretreatment time in Figure 11. The C_2+ yield is shown as a function of GHSV and CH_4/O_2 ratio and as a function of dilution ratio and CH_4/O_2 ratio in Figures 12 and 13, respectively. With an optimal methane conversion rate of 42.14% and a C_{2+} selectivity of 77.45%, the optimal C_{2+} yield was only 32.24%, but this maximum occurs at the boundary of the landscapes in Figures 12 and 13.

The Koenigs-Knorr glucuronidation of a nitrophenol was optimized with mole fractions of Ag_2CO_3 and HMTTA (1,1,4,7,10,10-Hexamethyltriethylenetetramine) as variables [13]. The resulting trap-free fitness

landscape is shown in Figure 14. The reported optimum of 87.5% yield lies at the boundary of the search space.

Optimization of the synthesis of methyl glucoside polyester (MGPE) was performed using the molar ratio of fatty acid methyl ester/methyl glucoside subtrates, reaction time, and temperature as variables in a total of 27 experiments [14]. Fitness landscapes for MGPE yield as a function of the variable pairs temperature/substrate ratio, reaction time/substrate ratio, and reaction time/temperature are shown in Figures 15 through 17, respectively. These landscapes are also trap-free. Although the optimal yield was only 55%, the authors comment that to improve the yield, higher temperatures must be used, which changes the color of the product MGPE and makes it unacceptable for industrial use.

The synthesis of cetyl oleate ester using the concentration of a zeolite catalyst and temperature as variables was optimized [15]. The interpolated surface of experimental data points is shown in Figure 18 with the maximum yield of 73% being on the boundary of the fitness landscape.

1.2 Optimization of Polymer Synthesis Conditions

Optimization of the synthesis of poly((*RS*)-3,3,3-trifluorolactic acid), or poly((*RS*)-TFL) was conducted in 15 experiments using temperature and mole fraction of 1,3-diisopropylcarbodiimide condensing reagent as variables [16]. The two employed catalysts were 4-(dimethylamino)pyridinium 4-toluenesulfonate (DPTS) or 4-(dimethylamino)pyridinium triflate (DPTL). Figures 19 and 20 show the yield of polymer as a function of temperature and mole fraction of carbodiimide reagent for reaction with DPTS and DPTL, respectively. The solution viscosity (i.e., molecular weight of polymer) is plotted versus the same variables in Figures 21 and 22, also yielding trap-free fitness landscapes. The optimal regions (maximal yield=41.3%) are at the boundaries of the search space studied.

The synthesis of high-molecular weight polymer chitosan was optimized using reaction time, temperature, and mole fraction of NaOH reagent as varaibles [17]. The resulting 3-dimensional fitness landscapes for molecular weight of chitosan and degree of deacetylation of chitosan are shown in Figures 23 and 24, respectively (the absolute maximum is not known). As these are three-dimensional plots, each surface corresponds to a level set at the recorded objective value.

The synthesis of single-walled carbon nanotubes from acetylene over a FeMo/MgO catalyst was optimized [18]. The variables used were mole ratio of Fe to MgO in the catalyst, flow rate of argon gas in the reaction chamber, and temperature. Fitness landscapes for each pair of variables recording QDN (quality descriptor number, a measure of the fraction of nanotubes synthesized that are single-walled) and C% (carbon deposit percentage) are shown in Figure 25. All of the fitness landscapes are trap-free.

1.3 Optimization of Enzyme-Catalyzed Reactions

Many studies, often in the food industry, optimize reaction conditions for enzyme-catalyzed reactions using response surface methodology. The examples below are only a small sample of the literature on this topic.

The optimization of lipase-catalyzed regioselective esterification of pyridoxine was performed [19]. The variables were reaction time, temperature, mole fractions of water and enzyme, and vinyl acetate/pyridoxine molar ratio. The fitness landscapes for pairs of these variables are shown in Figures 26 through 29. All of the landscapes are trap-free and have large optimal regions at $> 99\%$ conversion, indicating optimal level sets.

The lipase-catalyzed synthesis of betulinic acid ester from betulinic acid and benzoyl chloride was optimized using the variables reaction time, temperature, and mole fraction of enzyme [20]. Surfaces of reaction yield versus pairs of these variables are shown in Figures 30 through 32. All are trap-free; the maximal yield of 48.5% is on the boundary of all fitness landscapes, suggesting that expanding the variable range may improve yield.

The esterfication of ascorbic acid (vitamin C) using lipase was optimized using reaction time, temperature, enzyme concentration, substrate (ascorbic acid) concentration, and water content as variables [21]. Fitness landscape plots of yield versus each variable and enzyme concentration are shown in Figure 33, and plots of yield versus other pairs of variables are shown in Figure 34, all of which are trap-free.

A three-dimensional fitness landscape of yield versus water content, substrate concentration, and temperature is shown in Figure 35. This plot is also trap-free with a global maximum near the center of the space. The maximal conversion was 48%, but this existed at the boundary of all of the enzyme concentration plots (Figure 33).

The enzyme-catalyzed synthesis of isopropyl esters using enzyme concentration and alcohol/oil molar substrate ratio as variables was optimized [22]. The experimental landscape is shown in Figure 36 to be trap free with a maximal yield of 84%

The lipase-catalyzed synthesis of the acylation of L-lysine with palmitic acid and oleic acid was optimized [23]. The variables consisted of temperature, solvent hydrophobicity (LogP), enzyme amount, molecular sieve amount and fatty acid substrate concentration. The yield of acylated lysine is plotted versus pairs of variables for the palmitic acid product (left) and oleic acid product (right) in Figures 37 through 41. The fitness landscapes are the result of third-order polynomial fits and all are trap-free. The reported maximum yield for the palmitic acid product was 16.1% and for the oleic acid product was 33.1%.

The lipase-catalyzed synthesis of wax esters from palm oil and oleyl alcohol was optimized using time, temperature, substrate molar ratio, and enzyme amount as variables [24]. The molar yield of wax esters as a function of pairs of the variables is shown in Figures 42 through 47. The maximal yield was 84.6%.

1.4 Optimization of Biologically Produced Compounds

The optimization of reaction conditions for the synthesis of compounds produced by biological organisms (e.g., yeast, bacteria) is also common in the food and energy industries.

The production of acetic acid from CO using fermentation by *Clostridium aceticum* bacteria was optimized using the fermentation time and concentrations of the nutrients NH_4Cl and yeast extract as variables [25]. The goal consisted of maximizing acetic acid yield while minimizing CO concentration and having the bacterial cell concentration within a desired range. The fitness landscapes for this multiobjective goal versus fermentation time and NH_4Cl and yeast extract concentration are shown in Figures 48 and 49. Even for these multiobjective cases, the fitness landscapes are trap-free. 100% CO conversion was obtained.

The production of the herbicide azadirachtin from the bacterium *Azadirachta indica* was optimized using concentrations of the elicitors jasmonic acid, chitosan, and salicylic acid as variables [26]. The fitness landscapes for yield of azadirachtin versus pairs of the variables are shown in Figure 50. No percent yield data was given.

The synthesis of acetic acid from carbon monoxide with *Clostridium aceticum* was optimized using partial pressure of CO and reaction time as variables [27]. The fitness landscapes were constructed using third-order polynomial fitting. Figure 51 shows the effect of CO partial pressure and reaction time on (a) cell density of *Clostridium aceticum*, (b) acetic acid yield, and (c) residual CO. All these fitness landscapes are trap-free.

The synthesis of toxin proteins Cry4Ba and Cry11Aa from *Bacillus thuringiensis* was optimized using temperature, C:N ratio (ratio of organic carbon to organic nitrogen as food sources), K_2HPO_4 concentration and Mn concentration as variables [28]. Fitness landscapes for production of Cry4Ba as functions of pairs of variables are shown in Figure 52 and those for production of Cry11Aa are shown in Figure 53. These surfaces were constructed using third-order polynomial fitting and are all trap-free. Some of the fitness landscapes show the presence of saddle points.

The production of lovastatin from *Aspergillus flavipes* was reported using water content and particle size of wheat bran food source as variables [29]. The reported trap-free fitness landscape is shown in Figure 54.

The production of thermally stable lipase enzyme from *Geobacillus* species was optimized using temperature, inocolum size, agitation rate, medium volume, initial pH, and incubation time as variables [30]. The resulting lipase activity is plotted versus pairs of variables in Figure 55. All of the fitness landscapes are trap-free.

2 Optimization of Catalyst Compositions

A common synthetic target is optimization of the composition of solid-state catalysts for chemical reactions, with the variables $\mathbf{p}=[p_1,\ p_2 \dots p_i]$, satisfying $\sum_i p_i = 1$, as well as possibly including additional processing conditions. These studies predominantly produced trap-free fitness landscapes, although there are a few examples with traps. The results are summarized by target objective.

2.1 Selective oxidation of isobutane

Two sets of fitness landscapes from [31] were presented in the main work, where the Mo-V-Bi landscape appeared to contain traps when formation of isobutene was selected as the target objective. The remaining two sets of landscapes, from a Mo-V-Fe library (Figure 56) and a V-Bi-Sb library (Figure 57) may contain traps for the isobutene fitness landscape as well. It is conjectured that the sets of variables Mo-V-Bi, Mo-V-Fe, and V-Bi-Sb constitute constrained variable choices compared to Mo-V-Sb, as the overall relative conversions (compared to a referance literature catalyst) were inferior to Mo-V-Sb.

2.2 Oxidation of CO

An examination of the fitness landscape for catalytic oxidation CO $\rightarrow$ CO_2 was performed [32], where libraries of ternary metal alloys Rh-Pd-Pt and Rh-Pd-Cu were examined. Although the fitness landscapes are generally monotonic, with highest catalytic activity in the Rh-rich region, there appear to be some discontinuities in the middle region of the Rh-Pd-Pt library at reaction temperature of 673K, as shown in Figure 58. The reaction rate for the Rh-Pd-Pt system is affected by a kinetic phase transition of the surface at the "ignition temperature" of the reaction, and the authors suggest that "the discontinuities in catalyst activity seen... (namely, low activity elements surrounded by much more active elements) may be caused by these kinetic instabilities" [32]. These results suggest that fitness measurement may be unstable at temperatures near the kinetic phase transition, as the reaction temperature (here, fixed at 673K) may make the materials kinetically unstable, thus drastically increasing or decreasing their catalytic ability if they undergo a phase transition. This case illustrates how process variables (here, temperature) must be taken into account when evaluating and utilizing OptiChem theory. The oxidation of CO to CO_2 was also studied for a Rh-Pd-Cu system at 673K, producing the fitness landscape shown in Figure 59A, which appears to contain two isolated optimal regions and no traps. The projection on the Rh-Cu axis in Figure 59B shows that the height of the two maxima (at Cu/Rh=0 and Cu/Rh-0.57) is the same, indicating a level set of two isolated points. In the same study, the oxidation of CO by NO to produce CO_2, N_2 and N_2O was examined for the Rh-Pd-Pt library. The catalytic production of N_2 is shown in Figure 60A, and the production of N_2O is shown in Figure 60B at 673K (top), 773K (middle), and 873K (bottom). The fitness landscapes appear trap-free, with some discontinuities that are probably caused by the same kinetic phase instability as for the $CO+O_2 \rightarrow CO_2$ reaction discussed above.

Catalysis of the reaction $CO+O_2 \rightarrow CO_2$ was studied for Mn-Co-Al and Mn-Co-Ni libraries [33], and the resulting fitness landscapes shown in Figure 61 are both trap-free.

2.3 Reduction of NO_x

The catalytic reduction of $NO_x \rightarrow N_2$, an important process in reducing auto emissions, has been studied using an In-Ag-Co-Cu library [34]. The resulting fitness landscapes at reaction temperatures ranging from 400°C to 475°C produce trap-free landscapes (Figure 62). The same reaction was also studied using a Pt-Fe-Co-Cu library [35], which also produced trap-free fitness landscapes at temperatures ranging from 250°C to 400°C (Figure 5 of [35]).

2.4 Oxidation of ethane to ethylene

Several studies have examined the reaction $C_2H_6 \rightarrow C_2H_4$ with different solid-state catalyst libraries. The production of ethylene and $CO_2$was studied for Ni-Co-Nb and Ni-Ta-Nb libraries [36]. The fitness

landscapes for formation of both products by the Ni-Co-Nb library are trap-free (Figure 63), but the Ni-Ta-Nb landscape for ethylene production may contain traps (Figure 64). The maximal yield of ethylene for this library, however, was much lower than for the Ni-Co-Nb library. The authors claim that the best Ni-Ta-Nb catalyst, although producing less ethylene, was more selective than the best Ni-Co-Nb catalyst [36]. The same reaction with an Mo-V-Nb library was also studied [37]. The resulting fitness landscape for ethylene concentration (Figure 2 in [37]) is trap-free.

The production of ethylene by V-Mo-Li and V-Mo-Rb libraries was performed [38]. For the V-Mo-Li library, the yield of the products ethylene (Figure 65a), CO_2 (Figure 65b), and the consumption of O_2 (Figure 65c) are shown. The fitness landscape for ethylene production appears nearly trap-free for the reported 5% error in the observable measurement [38]. The fitness landscapes for formation of CO_2 and consumption of O_2 have spikes in the observable value for pure vanadiaum catalysts and an otherwise nearly trap-free landscape. These spikes are not addressed in the original work. Figure 66 shows that replacement of Li with Rb in the library decreases ethylene production, but the general shape of the fitness landscapes for each observable is the same. The oxidation of propane to propylene was also optimized with the V-Mo-Li library, and the landscapes for the formation of propylene and consumption of O_2 were trap free for ratios of propane:O_2 of 2:1 (Figure 67a,c) and 1:1 (Figure 67b,d).

2.5 Oxidation of C_3 hydrocarbons

Several oxidation reactions of propane have also been studied with solid-state catalyst libraries. The yield of propene from a V-Mg-Ga library was examined [39], resulting in the fitness landscape in Figure 68, which appears trap-free to within a small degree of noise. Oxidation of propene to CO_2 ($C_3H_6 \rightarrow CO_2$) by reduction of NO ($NO \rightarrow N_2$) was studied for a Na-Pt-Pd-In library at temperatures ranging from 200°C to 550°C in [40]. The consumption of NO (Figure 69) produces clearly monotonic fitness landscapes in the temperature range 300-350°C. The consumption of C_3H_6 produces monotonic fitness landscapes at temperatures at 350°C and above (Figure 70). The CO_2 production fitness landscapes are monotonic at high temperatures (Figure 71).

2.6 Other reactions of small molecules

Other reactions using solid-state metal catalysts have produced trap-free fitness landscapes. The reduction of methanol to H_2 was explored using Al-Pb-Bi mixed metal oxide catalysts under photoexcitation [41]. The screening was repeated twice, with the material compositions at different positions under the light source. Essentially the same trap-free fitness landscape was obtained in both experiments (Figure 72). The oxidation of cyclohexane to benzene by a Pt-Pd-In library was studied in [42], where the resulting fitness landscape was also trap-free (Figure 73).

The photocatalytic degradation of 1,6-hexamethylenediamine over W-Ti-Zr, W-Ti-V, V-Ti-Mo, and W-Zr-Nb libraries was studied [43]. The fitness landscapes of catalytic activity for the W-Ti-Zr library are shown in Figure 74 (a) (no additive) and (b) (block copolymer P123 template added). The fitness landscape in (a) appears to contain traps, but the addition of P123 makes the landscape trap-free. The authors comment that a broader range of catalysts have high activity when P123 is added, although the maximal activity didn't increase [43]. This result suggests that addition of P123 lifted a constraint, resulting in the disappearance of a trap and possible generation of an optimal level set. The fitness landscapes for the W-Ti-V and V-Ti-Mo libraries are shown in Figure 75 (a) and (b) respectively. The W-Ti-V fitness landscape appears trap-free, but the V-Ti-Mo fitness landscape may contain traps. The W-Zr-Nb library was prepared using three different processing conditions; catalytic fitness landscapes are shown in Figure 76 (a) (tungsten precursor=$(NH_4)_5H_5[H_2(WO_4)_6]\cdot H_2O$ in ethanol), (b) (tungsten precursor=WCl_6 in ethanol, no P123), and (c) (tungsten precursor=WCl_6 in ethanol, with P123). The catalytic activity is generally highest in the library with P123 (Figure 76(c)), which also produces the fitness landscape that most closely appears to be trap-free. This is another instance where adding P123 constitutes lifting a constraint on the variables.

The catalytic decomposition of $NaBH_4$ to release H_2 using Ru-Co-Ni and Ru-Co-Fe libraries produced trap-free landscapes of H_2 production rate versus catalyst composition (Figure 77) [44].

2.7 Catalysis by electrochemistry

The ability of materials to catalyze reactions in electrochemical cells has also been investigated [45, 46]. The variables are mole fractions of each component, but instead of directly measuring catalytic activity, the onset potential for activation of the desired reaction is measured. Some physical properties are measured as well. The catalytic reduction of O_2 to H_2O by electrochemical cells consisting of Pt-Co-Ti, Pt-Co-Cu, and Pt-Co-Cr cathode catalyst compositions was examined [45]. The onset electrochemical potential for the oxidation reaction for the Pt-Co-Ti system and the system stability are shown in Figure 78, with both fitness landscapes being trap-free. The onset potential for the Pt-Co-Cu system is shown in Figure 79, and the stability of this system is shown in Figure 80(c) also producing trap-free fitness landscapes. The onset potential and stability for the Pt-Co-Cr system produce the trap-free fitness landscapes in Figure 80(a) and (b). The compositions Pt-Ru-W and Pt-Ru-Co were studied as anode catalysts for methanol oxidation fuel cells [46]. The X-ray diffraction pattern 2θ shift of the main spectral peak was shown to vary monotonically with Pt-Ru-Co composition (Figure 81). The peak current through the Pt-Ru-W cell (a) and the onset potential for oxidation (b) are shown in Figure 82. There may be traps in the current fitness landscape, but the authors note that "to cover the ternary field a library with reasonably wide steps was required" [46], so the apparent discontinuities may be due to insufficient sampling. Figure 83 shows the peak current (a) and onset potential (b) for the Pt-Ru-Co system; here, both fitness landscapes are trap-free.

3 Physical Properties of Materials

3.1 Luminescent Materials

Many studies of luminescent materials result in trap-free fitness landscapes [47, 48, 49, 50, 51, 52, 53, 54, 55, 56, 57, 58, 59]. In all of these studies, combinations of metal oxides were used to optimize luminescence from the materials upon excitation with UV light. The variables are the mole fractions of the various metal (or metal oxide) components, i.e. $\mathbf{p}=[p_1 p_2 \dots p_i]$ with the restriction $\sum_i p_i = 1$, as was the case with the catalytic activity fitness landscapes reported in Section 2. Each study is discussed briefly below.

A ternary library of M_2CeO_4 was constructed with the varied metal M=Ca, Sr, and Ba (i.e. the variables $\mathbf{p} = [p_{Ca}\, p_{Sr}\, p_{Ba}]$, $p_{Ca}+p_{Sr}+p_{Ba} = 1$) [47]. The fitness landscape is trap-free, with monotonic increase in intensity as Sr (top corner) content increases (see Figure 3 in [47]). The optimal region extends down the Sr-Ba line (left side of the triangle), showing the presence of a level set of homologous optimal luminescent materials.

Optimization of red luminescence from excitation with 254nm and 147nm radiation was performed for an As-Nb-P-V library, resulting in quaternary fitness landscapes [48]. The fitness landscapes for luminescence at both exciation wavelengths were shown in the main work; the landscapes for the x and y coordinates of CIE (Commission Internationale de l'Eclairage) color chromaticity for the emission radiation are shown in Figure 84, where both of the fitness landscapes are trap-free.

The optimization of 147nm blue luminescence and color chromaticity was performed on a ternary Sr-B-P oxide [49]. The fitness landscape for luminescent intensity shows the full search space and subsequent fine-tuning landscapes around the optimum, all of which are trap-free. The CIE color chromaticity in the y coordinate also produces a trap-free landscape. The landscapes are shown in Figures 85 and 86, respectively.

The red luminescence of a Al-Mg-Ca phosphor library under 246nm excitation radiation was optimized [50]. The fitness landscape for luminescence shown in Figure 87 is trap-free.

The red luminescence of Ti-Y-Gd oxide phosphors was optimized under excitation by 254nm and 400nm radiation [51]. The fitness landscapes are shown in Figure 88(a) for 254nm and Figure 88(b) for 400nm under four different firing temperatures. The fitness landscapes are clearly trap free for at least one firing temperature (700°C) for both excitation wavelengths. The use of different firing temperatures constitutes a fourth variable; the reported fitness landscapes are three-dimensional slices of this four-dimensional landscape.

Blue luminescence from a quaternary Sr-Ba-Mg-Ca library under 400nm excitation radiation produced a trap-free four-dimensional fitness landscape [52] in Figure 89, where the full landscape is labeled [A_1 B_1 C_1 D_1], and the remaining landscapes are subsets of the full landscape.

The red luminescence from an Al-Gd-Mg library [53] produced fitness landscapes for the firing temperatures 1000°C (a), 1100°C (b), 1200°C (c), and 1300°C (d) in Figure 90. All of the fitness landscapes are trap-free, as are three-dimensional slices of a four-dimensional landscape with the fourth variable being firing temperature. In the same work, an Al-Gd-Li library was studied as well, producing fitness landscapes for firing temperatures 900°C (a), 1000°C (b), and 1100°C (c) in Figure 91. The fitness landscapes at 900°C and 1000°C are trap-free; stacking the landscapes with firing temperature as the fourth variable may produce a trap-free four-dimensional landscape, but it is difficult to see this by eye.

Red luminescence from quaternary libraries of Gd-Sc-Y-Lu and Y-Gd-P-B under 146nm excitation radiation [54] produced the quaternary fitness landscapes in Figure 92 for the Gd-Sc-Y-Lu library (a) and the Y-Gd-P-B library (b); both landscapes appear trap-free.

Green luminescence from a Gd-Ca-Al library under 147nm excitation radiation [55] resulted in the fitness landscapes shown in Figure 93 for libraries fired at 1100°C (1), 1200°C (2), 1300°C (3), and 1400°C (4). All of the landscapes are trap-free, and could be stacked to produce a four-dimensional trap-free fitness landscape with the fourth variable being firing temperature.

White luminescence under 405nm excitation radiation from a Ba-Sr-Mg-Ca library [56] resulted in the quaternary fitness landscape shown in Figure 94. The full landscape is labeled [A_1 B_1 C_1 D_1], and the remaining landscapes are subsets of the full landscape which show that the full landscape is trap-free. In the same work, the color of the luminescense for a Sr-Si-Eu library was examined under 405nm and 465nm excitation radiation, resulting in the fitness landscapes shown in Figure 95, which are also monotonic with respect to color.

Luminescence from a quarternary Dy-Pr-Nd-Ce system was examined [57], where the excitation wavelength was 365nm. The quarternary fitness landscape in Figure 1 of [57] is labeled [A_1 B_1 C_1 D_1] and the remaining landscapes are subsets of the full landscape. The full landscape appears trap free; this conclusion is supported by looking at the subset landscapes, none of which contain obvious traps.

White luminescence under 254nm excitation radiation was studied in a Tb-Sc-Pr library [58]. A photograph of the library is shown in Figure 96(a), and the intensity fitness landscape is shown in Figure 96(b); both landscapes are trap-free.

3.2 Spectral Properties of Materials

A related goal to optimizing luminescence of materials is to identify materials with some specific spectral property (e.g., color or location of spectral peaks). Different spectral properties of a variety of materials were identified as having trap-free fitness landscapes, where the variables are the mole fractions of the various metal components, i.e. $\mathbf{p}=[p_1 p_2 \dots p_i]$, $\sum_i p_i = 1$. The color of fluorescence from a Y-Eu-Bi library [59] resulted in the fitness landscape shown in Figure 97, where the color varies monotonically from red through pink and violet to blue across the composition space. The color fitness landscape for glass materials containing P, Te, and Zn [60] varies monotonically with composition for libraries produced at batch-melting temperatures of 900°C (a), 1000°C (b), and 1100°C (c), as shown in Figure 98. The melting temperature constitutes a fourth variable, as in cases described above. X-ray diffraction spectral properties also produced trap-free fitness landscapes. X-ray diffraction (XRD) spectra were obtained for a Ti-Ni-Pd thin film library [61]. The spectral intensity of four different peaks in the XRD spectrum was plotted versus composition, yielding trap-free fitness landscapes in all cases (Figure 99 (b)-(d)). The XRD spectral intensity of a peak characteristic of $Bi_4Ti_3O_{12}$ crystal structure was studied for six different ternary libraries of M-Bi-Ti, where M=V, W, Cu, Mo, P, and Ba [62]. The resulting six ternary fitness landscapes for spectral intensity are shown in Figure 100, and the fitness landscapes for M=V, W, and Cu appear to be trap-free.

3.3 Mechanical Properties of Materials

Mechanical properties such as hardness and elastic modulus also produce trap-free fitness landscapes. The Charpy impact parameter and Vickers hardness parameter were examined for a Zr-Cu-Al library [63], producing the trap-free fitness landscapes in Figure 101. Lattice constants and the Vickers hardness parameter were examined in an Al-Ti-Zr library [64]. Although only a small region of the available ternary search space produced materials in the desired γ-phase, the resulting fitness landscapes in Figures 102 and 103 are trap-free. The hardness and elastic modulus were measured for a Pd-Rh-Pt ternary system [65]. Both resulting fitness landscapes are trap-free, as shown in Figures 6 and 7 in [65].

3.4 Electronic Properties of Materials

Many different electronic properties of materials also yielded trap-free fitness landscapes, when mole fractions of the component metals were used as variables, unless otherwise indicated. Optimization of the dielectric constant of mixed metal oxides with the variables Zr, Hf, and Sn was conducted [66], where deposition of the oxide samples was carried out at 400°C and 500°C. The resulting fitness landscapes are shown in Figure 104. Both appear to be trap free; furthermore the fitness landscape at 400°C appears to have a level set in the optimal region, as the authors comment that the maximal value of the dielectric constant κ "was obtained at $Zr_{0.81}Hf_{0.12}Sn_{0.07}O_2$, although multiple compositions (all in the ZrO_2-rich area) yielded values of κ very close to this" [66]. Another study of the dielectric constant as a function of material composition was conducted on a Hf-Y-Al oxide system [67]. This fitness landscape is shown in Figure 105, and also contains a level set, where the authors comment that "it is remarkable that wide regions of the HfO_2-Y_2O_3-Al_2O_3 ternary allow maintain high dielectric constants" [67]. The dielectric constant of a Zr-Sn-Ti thin-film library was measured as a function of material composition [68], where the resulting fitness landscape (Figure 106) shows that "the dielectric constant increases monotonically as the Ti content of the film is increased" [68], indicating a trap-free fitness landscape. This work also measured the maximum stored charge density of the same library operating as capacitor materials, producing the fitness landscape in Figure 107, which is also trap-free. The maximal stored charge density was also measured for a Hf-Sn-Ti film [69], resulting in a fitness landscape that was also trap-free (Figure 108).

The resistivity to electrical current flow was studied in a Si-Cu-Pd thin-film metallic glass system [70]. The resulting fitness landscape (see Figure 9 in [70]) was trap-free, with resistivity decreasing as Pd content increased. The thermal hysteresis (i.e., difference at a given temperature between when the material is heated and when it is cooled) of resistivity was studied in a Ti-Ni-Cu thin-film system [71]. The resulting fitness landscape for the region of composition space that underwent a phase change during the heating/cooling process is trap-free, as shown in Figure 109. Resistivity was measured in a Co-Mn-Ge library, where temperature and total $p_{Co} + p_{Mn} + p_{Ge}$ doping concentration were the variables [72]. The resulting fitness landscape (Figure 110) shows no traps. The resistivity and activation energy for conductivity of a Mn-Ni-Cu library [73] resulted in a resistivity fitness landscape ("conductivity map," shown in Figure 111) that is trap-free, with "two connected conductive areas" [73], which constitute a level set. The fitness landscape for the thermal activation energy of conduction shown in Figure 112 appears to contain two disconnected regions of minimal activation energy, marked by a I and II on the figure, but an apparent trap exists in the lower-right portion of the measured landscape.

The bandgap and out-of-plane lattice constant for a Ti-Zr-Hf library of semiconductors were determined [74]. The lattice constant was measured with a scanning X-ray microdiffractometer, producing a fitness landscape in which the "lattice constant gradually increases with increasing Zr and Hf content" [74], indicating a trap-free landscape. The bandgap "shifts towards higher energy with increasing Zr and Hf content" [74], also producing a trap-free landscape. These landscapes are shown in Figures 3 and 4 of [74].

3.5 Binding Properties of Materials

The ability of solid-state and polymer materials to bind other molecules also produces trap-free fitness landscapes for a variety of binding targets. In the solid-state materials, the variables are the mole fractions of each component, and in the polymer cases, the variables are the mole fractions of each monomer.

The reversible storage capacity of H_2 by a $LiNH_2$-MgH_2-$LiBH_4$ materials was studied [75]. The strength of the H_2 binding was recorded by the amount of H_2 desorbed from the material. The resulting fitness landscape is shown in Figure 113, where the first desorption was carried out at 220°C (Figure 113(a)), the second desorption was carried out at 285°C (Figure 113(b)), and the third desorption was carried out at 350°C (Figure 113(c)), where the blue-violet regions denote high binding capacity and red regions low binding capacity. The fitness landscape for the first desorption is clearly trap-free, with the maximum marked by X, while the second desorption has two disconnected maxima marked with X and Y-Z. The fitness landscape for the third desoprtion shows a different maximum marked by U, which the authors attribute to the previously optimal materials being degraded by repeated measurements. The binding capacity of H_2 by a Mg-Ti thin film was studied as a function of the ambient pressure of H_2 and mole fraction of Mg in the film [76]. The optical transmission of the film was measured as a function of composition and pressure, where by Beer-Lambert's law, the logarithm of the transmission measures the hydrogen concentration in the material. The resulting fitness landscape, in Figure 114, is trap-free, where high concentration of H_2 is denoted by the red regions. The optimal region corresponds to higher pressures, where "a plateau develops, which widens with increasing Mg content" [76], suggesting the presence of a level set. In the same work, the capacity for binding H_2 in a Mg-Ti-Ni ternary library was studied as well. Figure 115 (b) shows that amount of hydrogen bound at constant pressure versus composition, where light regions indicate high binding capacity, forming a trap-free fitness landscape. The enthalpy of binding of H_2 to the material compositions studied is plotted in Figure 115 (d), also producing a trap-free fitness landscape.

Hydrogen bonding properties in a segmented poly-(urethane-urea) library was studied as a function of curing temperature and composition of the chain-extender component [77]. The resulting two-dimensional fitness landscapes for urea-urea hydrogen bonding (Figure 116(a)) and total hydrogen bonding (Figure 116(b)) both show clear monotonic trends, although there is some noise in the data that could be interpreted as traps.

The binding selectivity of molecularly imprinted polymers was studied [78, 79]. The polymers were created using continuously varying mole fractions of two monomer units x and y, where compositions satisfy the constraint ($p_x + p_y = 1$). In one case [78], the monomer components were methacrylic acid (MAA) and 2-(trifluoromethyl)acrylic acid (TFMAA). The polymers were imprinted against ametryn (Figure 117) and azatrine (Figure 118), resulting in the fitness landscapes for binding to ametryn (a), azatrine (b), and selectivity of ametryn versus azatrine bound (Figure 117(c)) and selectivity of azatrine versus ametryn bound (Figure 118(c)). All of these fitness landscapes are trap-free to within some degree of experimental noise. In the other case [79], the monomer units were MAA and trimethylolpropane trimethacrylate (TRIM), and the polymers were imprinted with propranolol and Boc-L-Phe-OH. The resulting fitness landscapes were measured at acetonitrile amounts of 3mL (Figure 119(a)), 5.5mL (Figure 119(b)), and 8mL (Figure 119(c)). The landscapes in the figure are interpolated from the experimental data, and all are trap-free.

4 Molecular Properties

In one example, the glass transition temperature T_g and air-water contact angle of polymers were found to correlate with the length of the polymer backbone and pendant chain [80, 81]. A library of 112 polymers (14 pendent chain diphenols and 8 backbone diacids) was synthesized and the T_g and air-water contact angles measured, resulting in trap-free fitness landscapes for both properties when plotted versus the size of the component diphenols/diacids, as shown in Figure 120 for the T_g property. The authors comment that the plot "intuitively illustrate[s] that there may be a correlation between chemical structure and

the glass transition temperature" [81]. In this case, the simple chemometric of molecular size determines the objective value and results in a trap-free fitness landscape.

In all other cases of molecular property objecties, reordering was used to identify the appropriate fitness landscape, as explained in the main text. In the diagram used to illustrate the reordering concept (Figure 9 in the main text), the chemical moieties used at the sites X_1 and X_2 are given in Table 1. Other examples of reordering from data in the literature are presented below.

The yield of glycidil ether synthesis catalyzed by a library of hydroxylase mutants with two mutated amino acid sites was measured [82]. The fitness landscape for percentage conversion to glycidil ether appears rugged before reordering (Figure 121a); after reordering, it becomes smooth (Figure 121b). With knowledge of this reordering data, 45 additional mutants were generated, mostly with mutations selected from the optimal area of the reordered landscape, as well as some random mutations. Placing the resulting conversion values on the reordered fitness landscape shows that most of the mutants from the optimal landscape region produced high yield (Figure 121c). A library of disubstituted palladium bidentate catalysts was synthesized [83] and tested for the ability to kinetically resolve racemic cyclohexenyl acetate. The resulting reordered fitness landscape is trap-free (Figure 122). A di-substituted triazine library was tested for the ability to inhibit aggregation of Aβ2, a peptide involved in the progression of Alzheimer's disease [84]. The inhibitory activity was determined by measuring the fluorescence of attached GFP (green fluorescent protein) to the triazines. The resulting reordered fitness landscape is trap-free (Figure 123). Finally, a hexapeptide library with the first two amino acids fully sampled (400 library members) was tested for inhibition of the binding of a rat brain protein to its natural receptor [85]. Even though the remaining four amino acids on the peptide varied for each set of two determined amino acids, the reordered fitness landscape is still trap-free (Figure 124).

References

[1] Pescarmona, P. P., Janssen, K. P. F., and Jacobs, P. A. *Chem. Eur. J.* **13**, 6562 (2007).

[2] Hanrahan, G. and Lu, K. *Current Reviews in Analytical Chemistry* **36**, 151 (2006).

[3] Gooding, O. W. *Current Opinion in Chemical Biology* **8**, 297 (2004).

[4] Ilzarbe, L., Alvarez, M. J., Viles, E., and Tanco, M. *Quality and Reliability Engineering International* **24**, 417 (2008).

[5] Myers, R. H., Montgomery, D. C., Vining, G. G., Borror, C. M., and Kowalski, S. M. *Journal of Quality Technology* **36**, 53 (2004).

[6] Prvan, T. and Street, D. J. *Journal of Statistical Planning and Inference* **106**, 245 (2002).

[7] Kirsch, J. F., Clewell, W., and Simon, A. *J. Org. Chem.* **33**, 127 (1968).

[8] Scott, J. M. W. *Canadian Journal of Chemistry* **48**, 3808 (1970).

[9] Hogan, P. J., Hopes, P. A., Moss, W. O., Robinson, G. E., and Patel, I. *Org. Proc. Res. Dev.* .

[10] Aggarwal, V. K., Staubitz, A. C., and Owen, M. *Org. Proc. Res. Dev.* **10**, 64 (2006).

[11] Glasnov, T. N., Tye, H., and Kappe, C. O. *Tetrahedron* **64**, 2035 (2008).

[12] Thien, C. Y., Mohamed, A. R., and Bhatia, S. *Journal of Chemical Technology and Biotechnology* **82**, 81 (2007).

[13] Stazi, F., Palmisano, G., Turconi, M., and Santagostino, M. *J. Org. Chem.* **69**, 1097 (2004).

[14] Shieh, C.-J. and Lai, Y.-F. *J. Agric. Food Chem.* **48**, 1124 (2000).

[15] Bautista, L. F., Martinez, M., and Aracil, J. *Chem. Eng. Technol.* **20**, 287 (1997).

[16] McKie, D. B. and Lepeniotis, S. *Chemometrics and Intelligent Laboratory Systems* **41**, 105 (1998).

[17] Hwang, K. T., Jung, S. T., Lee, G. D., Chinnan, M. S., Park, Y. S., and Park, H. J. *J. Agric. Food Chem* **50**, 1876 (2002).

[18] Kukovecz, A., Mehn, D., Nemes-Nagy, E., Szabo, R., and Kiricsi, I. *Carbon* **43**(14), 2842 – 2849 (2005).

[19] Zhang, D.-H., Bai, S., Dong, X.-Y., and Sun, Y. *J. Agric. Food Chem.* **55**, 4526 (2007).

[20] Yasin, Y., Basri, M., Ahmad, F., and Salleh, A. B. *Journal of Chemical Technology and Biotechnology* **83**, 694 (2008).

[21] Lv, L.-X. and Chen, S.-Y. Li, Y.-Q. *Journal of the Science of Food and Agriculture* **88**, 659 (2007).

[22] Bouaid, A., Aparicio, J., Martinez, M., and Aracil, J. *Enzyme and Microbial Technology* **41**, 533 (2007).

[23] Soo, E., Salleh, A., Basri, M., Rahman, R., and Kamaruddin, K. *Process Biochemistry* **39**(11), 1511 – 1518 (2004).

[24] Basri, M., Rahman, R., Ebrahimpour, A., Salleh, A., Gunawan, E., and Rahman, M. *BMC Biotechnology* **7**(1), 53 (2007).

[25] Sim, J. H., Kamaruddin, A. H., and Long, W. S. *Biochemical Engineering Journal* **40**, 337 (2008).

[26] Prakash, G. and Siristava, A. K. *Biochemical Engineering Journal* **40**, 218 (2008).

[27] Sim, J. H., Kamaruddin, A. H., Long, W. S., and Najafpour, G. *Enzyme and Microbial Technology* **40**(5), 1234 – 1243 (2007).

[28] Tokcaer, Z., Bayraktar, E., Mehmetoglu, U., Ozcengiz, G., and Alaeddinoglu, N. G. *Process Biochemistry* **41**(2), 350 – 355 (2006).

[29] Valera, H., Gomes, J., Lakshmi, S., Gururaja, R., Suryanarayan, S., and Kumar, D. *Enzyme and Microbial Technology* **37**(5), 521 – 526 (2005).

[30] Ebrahimpour, A., Rahman, R., Ean Ch'ng, D., Basri, M., and Salleh, A. *BMC Biotechnology* **8**(1), 96 (2008).

[31] Paul, J. S., Jacobs, P. A., Weiss, P. W., and Maier, W. F. *Appl. Catal. A: Gen.* **265**, 185 (2004).

[32] Cong, P. J., Doolen, R. D., Fan, Q., Giaquinta, D. M., Guan, S. H., McFarland, E. W., Poojary, D. M., Self, K., Turner, H. W., and Weinberg, W. H. *Angew. Chem. Int. Ed.* **38**, 483 (1999).

[33] Saalfrank, J. W. and Maier, W. F. *C.R. Chemie* **7**, 483 (2004).

[34] Richter, A., Langpape, M., Kolf, S., Grubert, G., Eckelt, R., Radnik, J., Schneider, A., Pohl, M. M., and Fricke, R. *Applied Catalysis B: Environmental* **36**, 261 (2002).

[35] Liu, Z. M., Oh, K. S., and Woo, S. I. *Catalysis Surveys from Asia* **10**, 8 (2006).

[36] Liu, Y., Cong, P., Doolen, R. D., Guan, S., Markov, V., Woo, L., Zeyss, S., and Dingerdissen, U. *Appl. Catal. A: Gen.* **254**, 59 (2003).

[37] Cong, P. J., Dehestani, A., Doolen, R., Giaquinta, D. M., Guan, S. H., Markov, V., Poojary, D., Self, K., Turner, H., and Weinberg, W. H. *Proc. Natl. Acad. Sci. USA* **96**, 11077 (1999).

[38] Senkan, S., Ozturk, S., Krantz, K., and Onal, I. *Appl. Catal. A: Gen.* **254**, 97 (2003).

[39] Buyevskaya, O. V., Brueckner, A., Kondratenko, E. V., Wolf, D., and Baerns, M. *Catalysis Today* **67**, 369 (2001).

[40] Krantz, K., Ozturk, S., and Senkan, S. *Catalysis Today* **62**, 281 (2000).

[41] Seyler, M., Stoewe, K., and Maier, W. F. *Appl. Catal. B: Env.* **76**, 146 (2007).

[42] Senkan, S., Krantz, K., Ozturk, S., Zengin, V., and Onal, I. *Angew. Chem. Intl. Ed.* **38**, 2794 (1999).

[43] Dai, Q. X., Xiao, H. Y., Li, W. S., Na, Y. Q., and Zhou, X. P. *Appl. Catal. A: Gen.* **290**, 25 (2005).

[44] Park, J. H., Shakkthivel, P., Kim, H. J., Han, M. K., Jang, J. H., Kim, Y. R., Kim, H. S., and Shul, Y. G. *International Journal of Hydrogen Energy* **33**, 1845 (2008).

[45] Cooper, J. S. and McGinn, P. J. *App. Surf. Sci.* **254**, 662 (2007).

[46] Cooper, J. S. and McGinn, P. J. *Journal of Power Sources* **163**, 330 (2006).

[47] Danielson, E., Devenney, M., Giaquinta, D. M., Golden, J. H., Haushalter, R. C., McFarland, E. W., Poojary, D. M., Reaves, C. M., Weinberg, W. H., and Wu, X. D. *Science* **279**, 837 (1998).

[48] Sohn, K. S., Zeon, I. W., Chang, H., Seung, K. L., and Park, H. D. *Chem. Mater.* **14**, 2140 (2002).

[49] Sohn, K. S., Yoo, J. G., Shin, N., Toda, K., and Zang, D. S. *J. Electrochem. Soc.* **152**, H213 (2005).

[50] Seo, S. Y., Sohn, K. S., Park, H. D., and Lee, S. *J. Electrochem. Soc.* **149**, H12 (2002).

[51] Park, D. H., Cho, S. H., Kim, J. S., and Sohn, K. S. *Journal of Alloys and Compounds* **449**, 196 (2008).

[52] Park, J. K., Choi, K. J., Kang, H. G., Kim, J. M., and Kim, C. H. *Electrochemical and Solid State Letters* **10**, J15 (2007).

[53] Park, J. K., Kim, J. M., Kim, K. N., Kim, C. H., and Park, H. D. *Electrochemical and Solid State Letters* **7**, H39 (2004).

[54] Sohn, K. S., Kim, C. H., Park, J. T., and Park, H. D. *Journal of Materials Research* **17**, 3201 (2002).

[55] Kim, C. H., Park, S. M., Park, J. K., Park, H. D., Sohn, K. S., and Park, J. T. *J. Electrochem. Soc.* **149**, H183 (2002).

[56] Park, J. K., Choi, K. J., Kim, K. N., and Kim, C. H. *App. Phys. Lett.* **87**, 031108 (2005).

[57] Sohn, K. S., Seo, S. Y., and Park, H. D. *Electrochemical and Solid State Letters* **4**, H26 (2001).

[58] Takahashi, R., Kubota, H., Murakami, M., Yamamoto, Y., Matsumoto, Y., and Koinuma, H. *J. Comb. Chem.* **6**, 50 (2004).

[59] Chan, T. S., Kang, C. C., Liu, R. S., Chen, L., Liu, X.-N., Ding, J.-J., Bao, J., and Gao, C. *J. Comb. Chem.* **9**, 343 (2007).

[60] Konishi, T., Hondo, T., Araki, T., Keishi, N., Tsuchiya, T., Matsumoto, T., Suehara, S., Todoroki, S., and Inoue, S. *Journal of Non-Crystalline Solids* **324**, 58 (2003).

[61] Zarnetta, R., Savan, A., Thienhaus, S., and Ludwig, A. *App. Surf. Sci.* **254**, 743 (2007).

[62] Takahashi, R., Yonezawa, Y., Ohtani, M., Kawasaki, M., Matsumoto, Y., and Koinuma, H. *App. Surf. Sci.* **252**, 2477 (2006).

[63] Yokoyama, Y. *J. Noncryst. Sol.* **316**, 104 (2003).

[64] Tanda, D., Tanabe, T., Tamura, R., and Takeuchi, S. *Materials Science and Engineering A* **387-389**, 991 (2004).

[65] Zhao, J.-C., Jackson, M. R., Peluso, L. A., and Brewer, L. N. *JOM* **54**, 42 (2002).

[66] Xia, B., Chen, F., Campbell, S. A., Roberts, J. T., and Gladfelter, W. L. *Chemical Vapour Deposition* **10**, 195 (2004).

[67] Hasegawa, K., Ahmet, P., Okazaki, N., Hasegawa, T., Fujimoto, K., Watanabe, M., T., C., and Koinuma, H. *App. Surf. Sci.* **223**, 229 (2004).

[68] van Dover, R. B. and Schneemeyer, L. F. *Macromolecular Rapid Communications* **25**, 150 (2004).

[69] Schneemeyer, L. F., van Dover, R. B., and Fleming, R. M. *Appl. Phys. Lett.* **75**, 1967 (1999).

[70] Yamauchi, R., Hata, S., Sakurai, J., and Shimokohbe, A. *Japanese Journal of Applied Physics* **45**, 5911 (2006).

[71] Loebel, R., Thienhaus, S., Savan, A., and Ludwig, A. *Materials Science and Engineering A* **481-482**, 151 (2008).

[72] Tsui, F. and Chu, Y. S. *Macromolecular Rapid Communications* **25**, 189 (2004).

[73] Kukuruznyak, D. A., Ahmet, P., Chikyow, T., Yamamoto, A., and Ohuchi, F. S. *J. Appl. Phys.* **98**, 043710 (2005).

[74] Yamada, Y., Fukumura, T., Ikeda, M., Ohtani, M., Toyosaki, H., Ohtomo, A., Matsukura, F., Ohno, H., and Kawasaki, M. *Journal of Superconductivity* **18**, 109 (2005).

[75] Lewis, G. J., Sachtler, J. W. A., Low, J. J., Lesch, D. A., Faheem, S. A., Dosek, P. M., Knight, L. M., Halloran, L., Jensen, C. M., Yang, J., Sudik, A., Siegel, D. J., Wolverton, C., Ozolins, V., and Zhang, S. *Journal of Alloys and Compounds* **446-447**, 355 (2007).

[76] Gremaud, R., Broedersz, C. P., Borsa, D. M., Borgschulte, A., Mauron, P., Schreuders, H., Rector, J. H., Dam, B., and Griessen, R. *Advanced Materials* **19**, 2813 (2007).

[77] Sormana, J.-L. and Meredith, J. C. *Macromolecules* **37**, 2186 (2004).

[78] Takeuchi, T., Fukuma, D., and Matsui, J. *Analytical Chemistry* **71**, 285 (1999).

[79] Kempe, H. and Kempe, M. *Macromolecular Rapid Communications* **25**, 315 (2004).

[80] Brocchini, S., James, K., Tangpasuthadol, V., and Kohn, J. *J. Biomed. Mater. Res.* **42**, 66 (1998).

[81] Smith, J. R., Seyda, A., Weber, N., Knight, D., Abramson, S., and Kohn, J. *Macromolecular Rapid Communications* **25**, 127 (2004).

[82] Reetz, M., Wang, L. W., and Bocola, M. *Angew. Chem. Int. Ed.* **45**, 1236 (2006).

[83] Jiang, X.-B., van Leeuwen, P., and Reek, J. *Chem. Commun.* **22**, 2287 (2007).

[84] Kim, W., Kim, Y., Min, J., Chang, Y. T., and Hecht, M. H. *ACS Chemical Biology* **1**, 461 (2006).

[85] Dooley, C. T., Chung, N. N., Wilkes, B. C., Schiller, P. W., Bidlack, J. M., Pasternak, G. W., and Houghten, R. A. *Science* **266**, 2019 (1994).

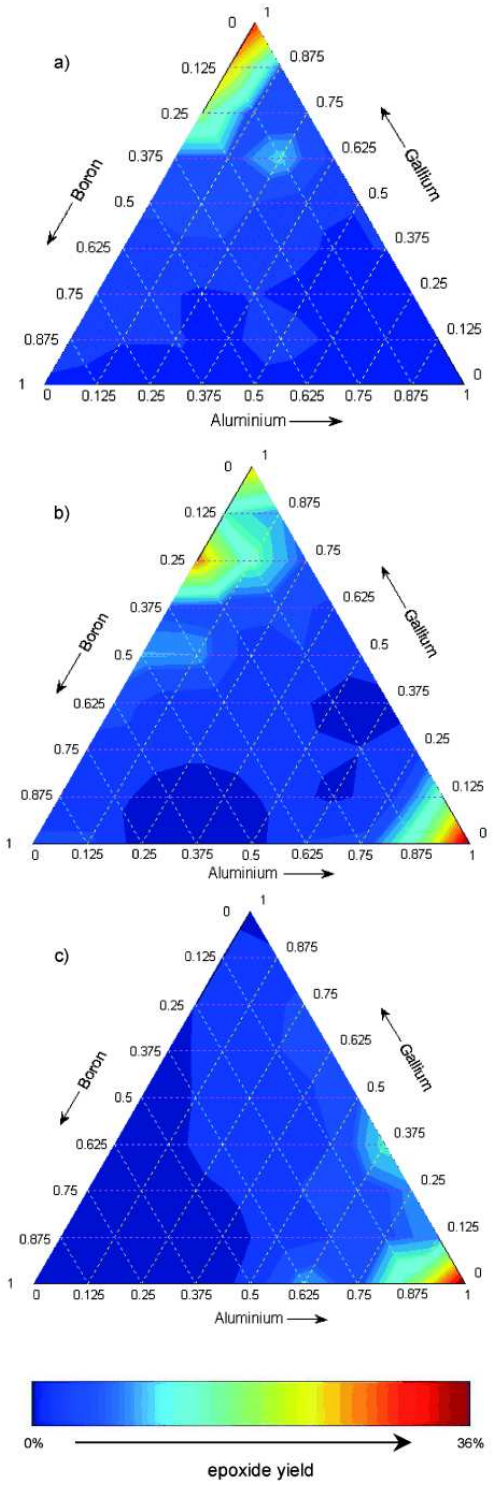

Figure 1: Fitness landscapes for catalytic behavior of a single B-Al-Ga alloy library. Variation of processing produces three different landscapes for the same objective. The optimal regions of the landscapes vary, depending on the processing. Such cases show that processing variables need to be taken into account when evaluating OptiChem theory. Copyright Wiley-VCH Verlag GmbH & Co. KGaA. Reproduced with permission.

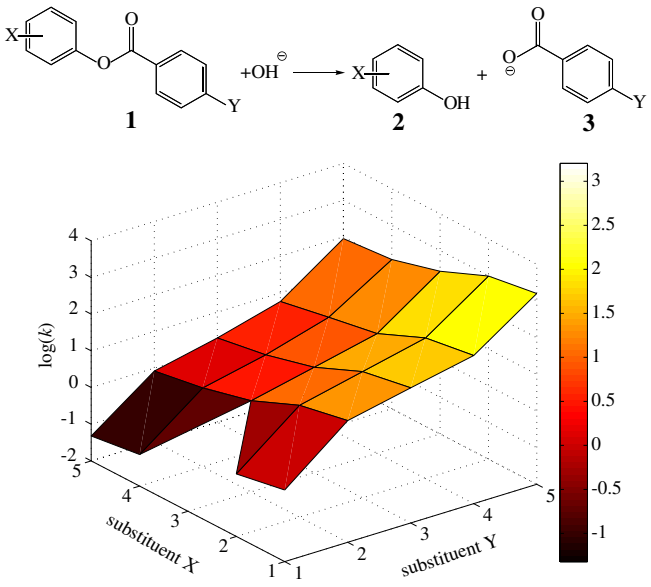

Figure 2: Reaction rate, $\log(k)$, of the hydrolysis of phenyl benzoate **1** by OH^- ion to produce alcohol **2** and benzoate **3**. The variables are the substituents X and Y, with 1=*p*-NO_2, 2=*m*-NO_2, 3=*p*-Cl, 4=*p*-H, 5=*p*-CH_3 for substituent X and 1=*p*-$N(CH_3)_2$, 2=*p*-CH_3, 3=*p*-H, 4=*p*-Cl, 5=*p*-NO_2 for substituent Y. For this landscape, the substituents are arranged in order of electron donor character (i.e., their Hammett constants), indicating that the Hammett constant is a good chemometric to describe the reactivity of the substrate **1**. The missing point in the landscape occurs because the combination X=*p*-Cl, Y=*p*$N(CH_3)_2$ was not tested.

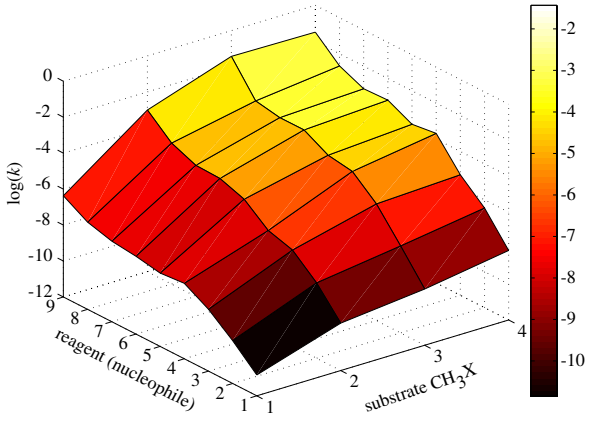

Figure 3: Rate, $\log(k)$, of the nucleophilic displacement reaction on the substrate CH_3X (for substituent X, 1=F, 2=Cl, 3=I, 4=Br) by nucleophiles (1=H_2O, 2=F^-, 3=Cl^-, 4=Br^-, 5=OH^-, 6=I^-, 7=SCN^-, 8=CN^-, 9=$S_2O_3{}^{2-}$). The ordering in terms of nucleophiles generally agrees with the accepted nucleophilicity rule, but the substrate ordering is not intuitive (i.e., Br^- reacts faster than I^-).

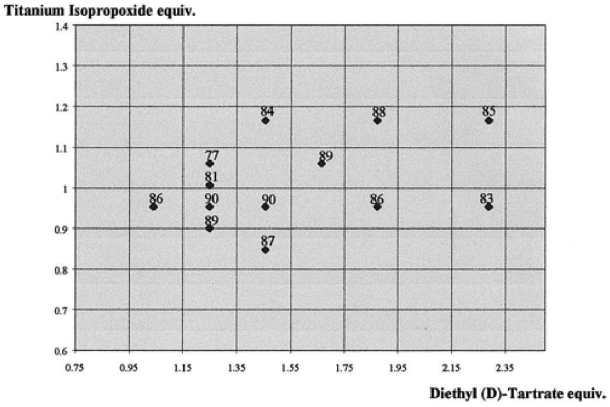

Figure 4: Enantiomeric excess of product sulfoxide with concentrations of Titanium isopropoxide and diethyl-*D*-tartrate as variables [9]. Even with the limited number of data points, the landscape appears trap-free. Reprinted with permission. Copyright 2002 American Chemical Society.

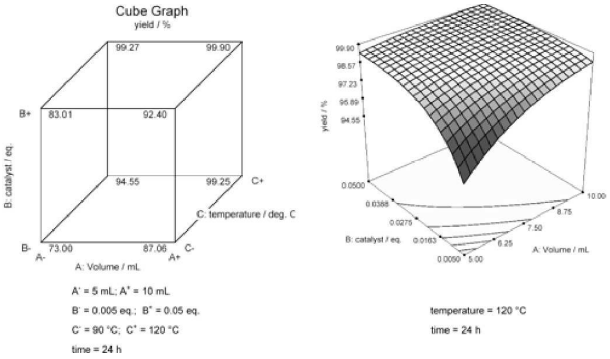

Figure 5: Yield of 3-phenyl cinnemaldehyde as a function of catalyst $Pd(OAc)_2$ concentration and total solvent volume [10]. The actual yields at the measured variables are shown on the left, and the interpolated surface is shown on the right. This surface has a large global maximum region, indicating an optimal level set. Reprinted with permission. Copyright 2006 American Chemical Society.

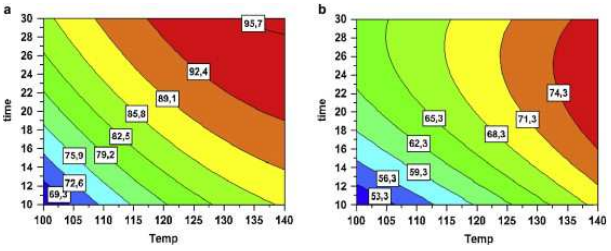

Figure 6: Yield of monasterol (a) and product purity (b) as a function of reaction time and temperature [11]. Reprinted with permission from Elsevier. Copyright 2008.

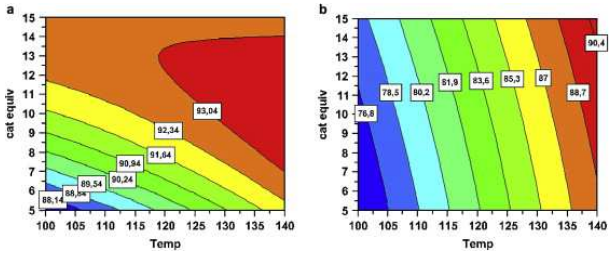

Figure 7: Yield of monasterol (a) and product purity (b) as a function of catalyst $LaCl_3$ concentration and temperature [11]. Reprinted with permission from Elsevier. Copyright 2008.

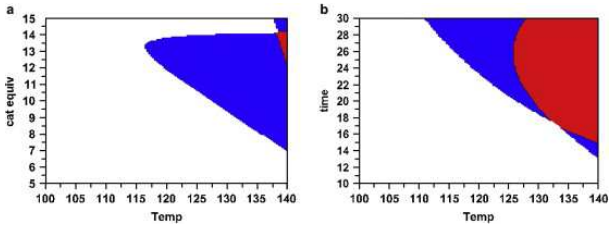

Figure 8: Optimal regions for monasterol yield and purity as a function of temperature and catalyst concentration (a) and temperature and reaction time (b). The red areas indicate optimal level sets. Reprinted with permission from Elsevier. Copyright 2008.

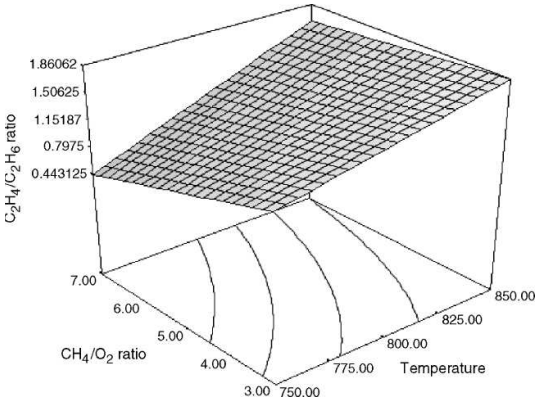

Figure 9: Ratio of ethylene:ethane as a function of temperature and CH_4/O_2 ratio [12]. The optimal region is on the edge of the measured domain. Copyright Wiley-VCH Verlag GmbH & Co. KGaA. Reproduced with permission.

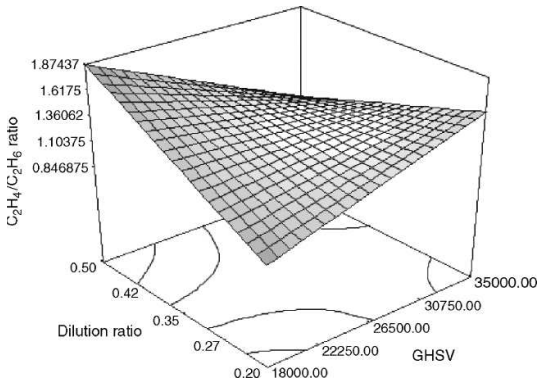

Figure 10: Ratio of ethylene:ethane as a function of GHSV of methane and the dilution ratio [12]. The optimal region is again on the edge of the measured region. Copyright Wiley-VCH Verlag GmbH & Co. KGaA. Reproduced with permission.

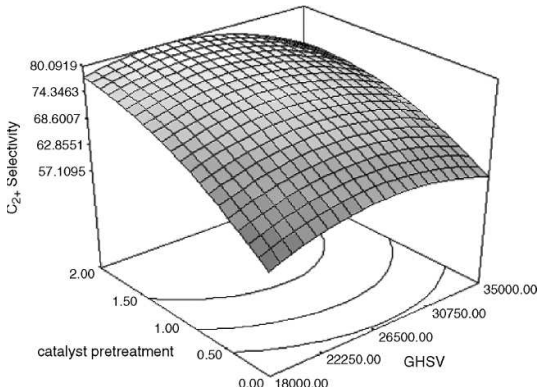

Figure 11: C_2+ selectivity as a function of GHSV and catalyst pretreatment time [12]. Copyright Wiley-VCH Verlag GmbH & Co. KGaA. Reproduced with permission.

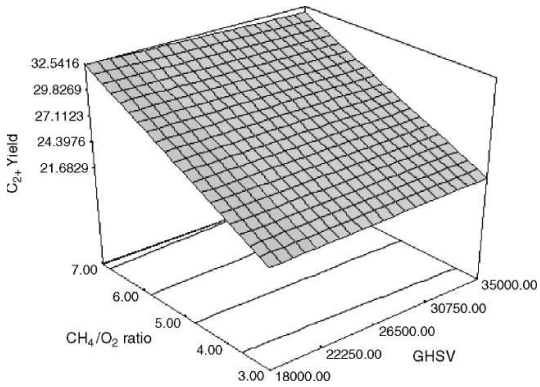

Figure 12: Yield of C_2+ as a function of GHSV and the CH_4/O_2 ratio [12]. The optimal region is on the edge of the measured region. Copyright Wiley-VCH Verlag GmbH & Co. KGaA. Reproduced with permission.

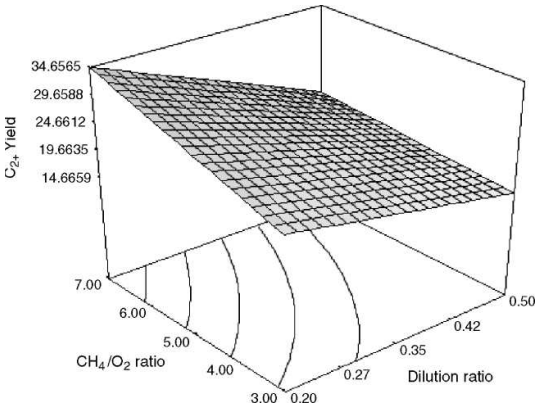

Figure 13: Ratio of ethylene:ethane as a function of the dilution ratio and CH_4/O_2 ratio [12]. The optimal region is on the edge of the measured region. Copyright Wiley-VCH Verlag GmbH & Co. KGaA. Reproduced with permission.

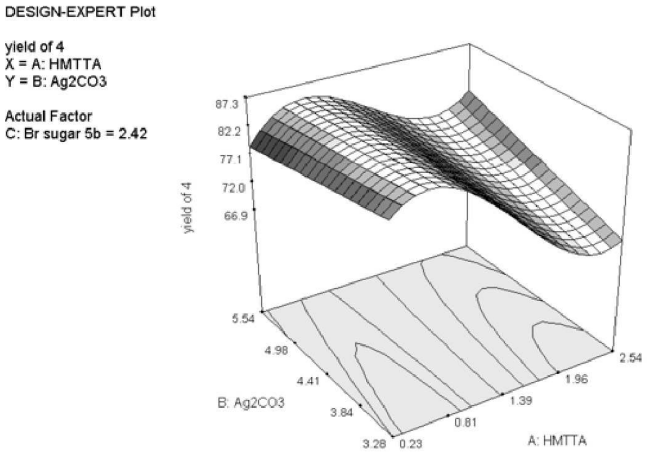

Figure 14: Yield of gluconoride product as a function of mole fractions of Ag_2CO_3 and HMTTA [13]. The optimal region may lie on the edge of the measured domain. Reprinted with permission. Copyright 2004 American Chemical Society.

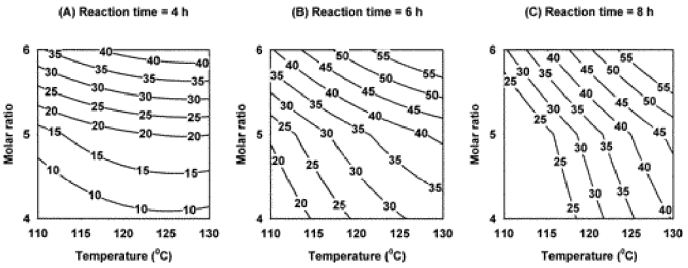

Figure 15: Yield of MGPE as a function of temperature and substrate ratio at three fixed reaction times [14]. All landscapes are trap-free, showing maximum yield at the upper limits of both variables. Reprinted with permission. Copyright 2000 American Chemical Society.

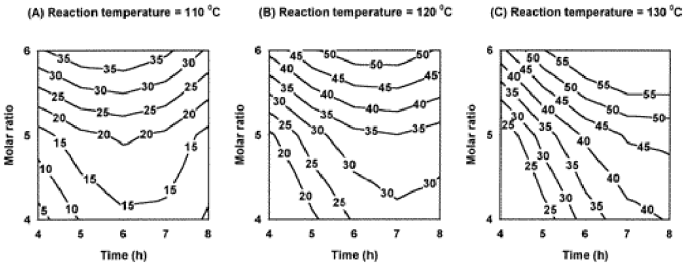

Figure 16: Yield of MGPE as a function of time and substrate ratio at three fixed temperatures [14]. All landscapes show maximum yield at the upper limits of the molar ratio. Reprinted with permission. Copyright 2000 American Chemical Society.

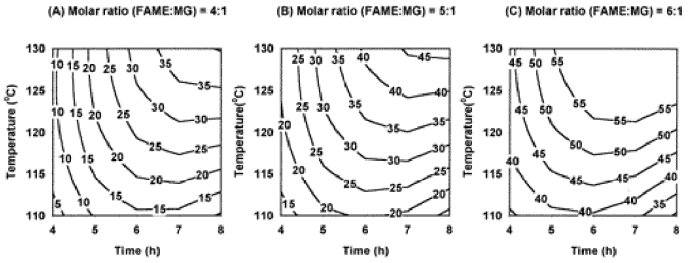

Figure 17: Yield of MGPE as a function of temperature and reaction time at three fixed substrate ratios [14]. All landscapes show maximum yield at the upper limits of both variables. Reprinted with permission. Copyright 2000 American Chemical Society.

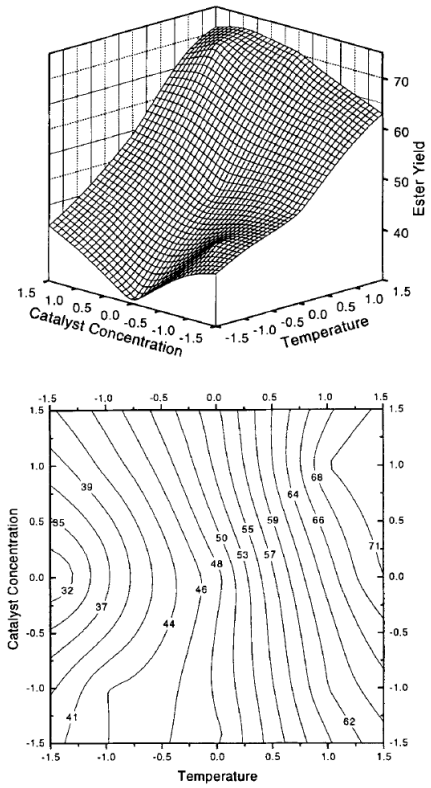

Figure 18: Interpolated surface of the experimental data points for yield of cetyl oleate ester with catalyst concentration and temperature as the variables. Three-dimensional surface (top) and contour plot (bottom). The maximum appears to lie at the temperature boundary. Copyright Wiley-VCH Verlag GmbH & Co. KGaA. Reproduced with permission.

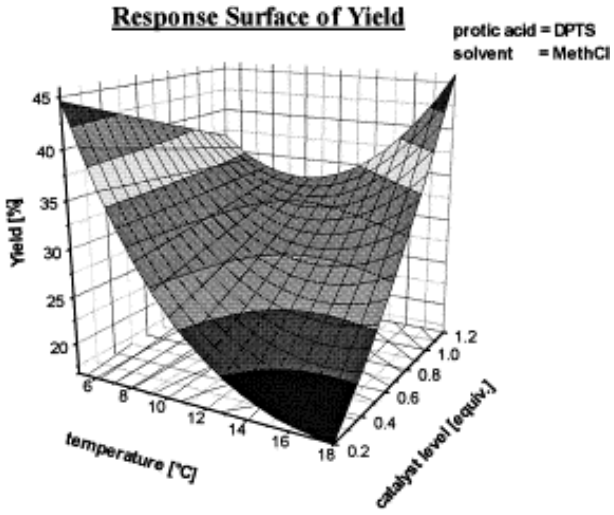

Figure 19: Yield of poly((*RS*)-TFL) as a function of temperature and mole fraction of carbodiimide reagent with DPTS catalyst [16]. There are two optimal regions at the opposite limits of the measured domain. Reprinted with permission from Elsevier. Copyright 1998.

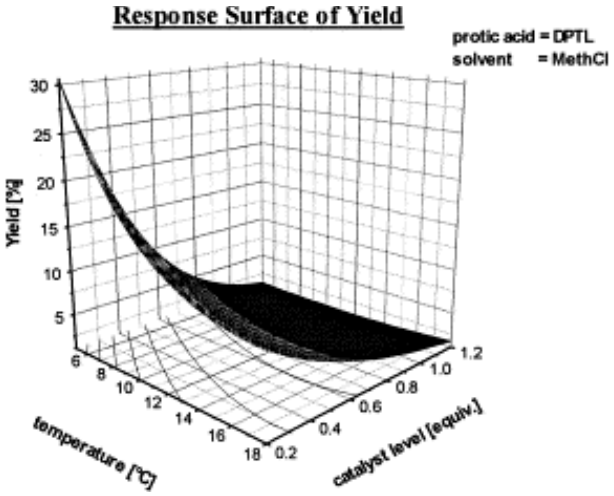

Figure 20: Yield of poly((*RS*)-TFL) as a function of temperature and mole fraction of carbodiimide reagent with DPTL catalyst [16]. The optimum exists at the minimum measured value of both variables. Reprinted with permission from Elsevier. Copyright 1998.

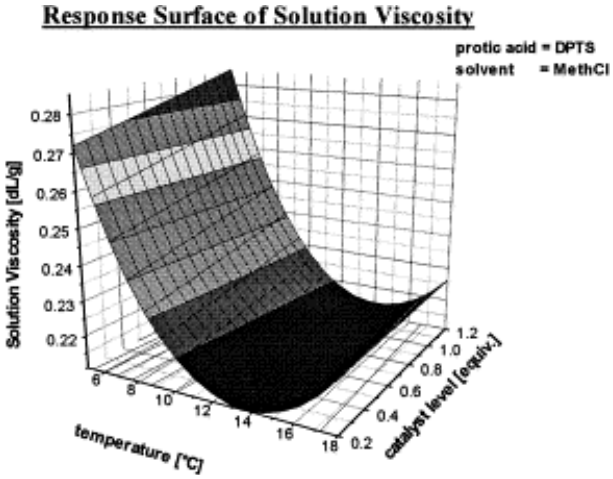

Figure 21: Solution viscosity (molecular weight) of poly((*RS*)-TFL) as a function of temperature and mole fraction of carbodiimide reagent with DPTS catalyst [16]. The optimum exists at the maximum measured catalyst level and minimum temperature. Reprinted with permission from Elsevier. Copyright 1998.

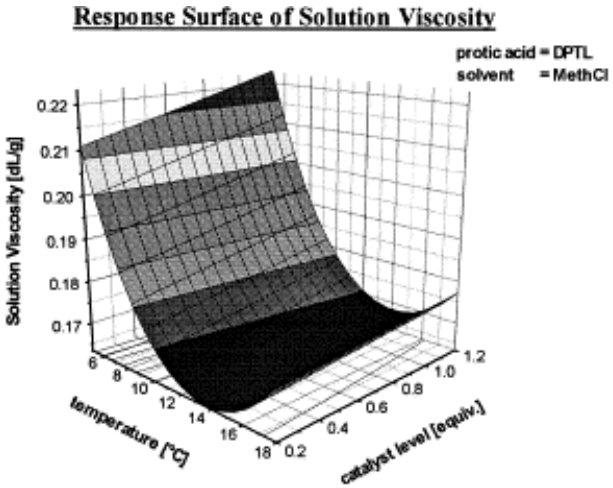

Figure 22: Solution viscosity (molecular weight) of poly((*RS*)-TFL) as a function of temperature and mole fraction of carbodiimide reagent with DPTL catalyst [16].The optimum exists at the maximum measured catalyst level and minimum temperature, as with the catalyst from Figure 21. Reprinted with permission from Elsevier. Copyright 1998.

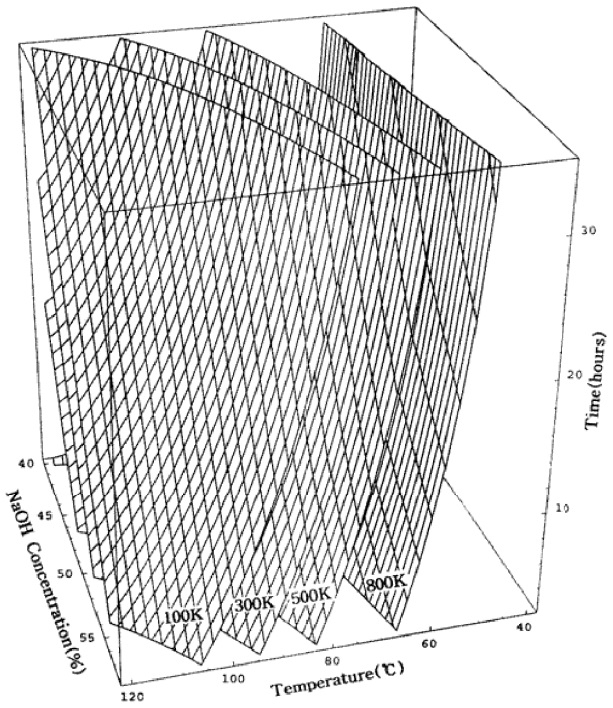

Figure 23: Molecular weight of chitosan polymer as a function of temperature, reaction time, and mole fraction of NaOH added [17]. This three-dimensional landscape shows level sets at different weights (in kilodaltons, K). Reprinted with permission. Copyright 2002 American Chemical Society.

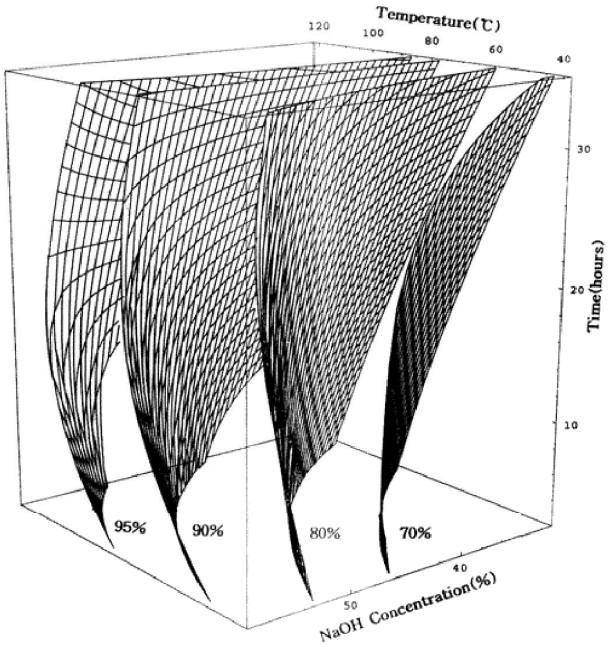

Figure 24: Degree of deacetylation of chitosan polymer as a function of temperature, reaction time, and mole fraction of NaOH added [17]. This three-dimensional landscape shows level sets at different deacetylation percentages. Reprinted with permission. Copyright 2002 American Chemical Society.

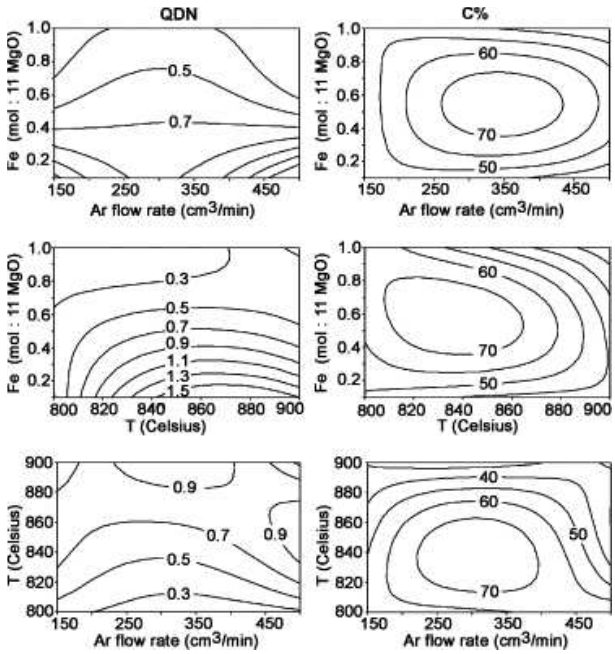

Figure 25: Yield of single-walled carbon nanotubes [18] as measured by QDN (quality descriptor number, a measure of the fraction of sample that is single-walled nanotubes) and C% (carbon deposition percentage) as a function of pairs of the variables drawn from temperature, Ar gas flow rate, and mole fraction of Fe in the catalyst. All of the landscapes are trap-free. Reprinted with permission from Elsevier. Copyright 2005.

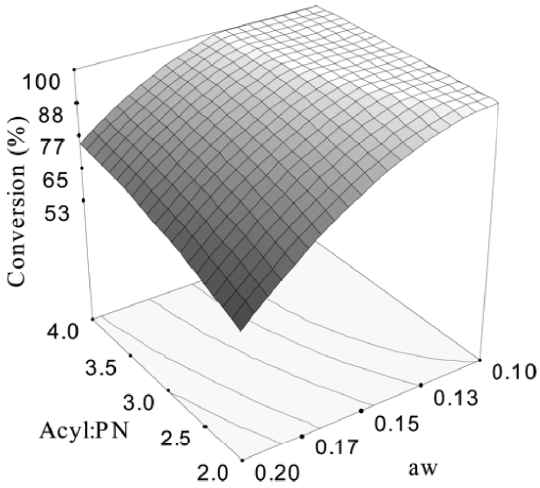

Figure 26: Yield of pyridoxine ester from lipase catalyzed reaction as a function of substrate molar ratio and mole fraction of water added [19]. There is a large optimal level set region. Reprinted with permission. Copyright 2007 American Chemical Society.

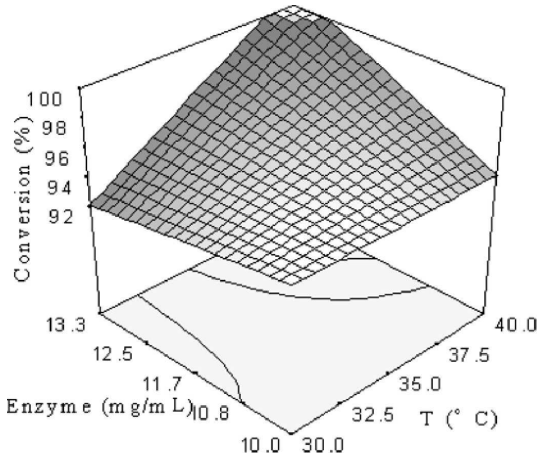

Figure 27: Yield of pyridoxine ester from lipase catalyzed reaction as a function of temperature and mole fraction of enzyme [19]. The small level set at the maximum value of both variables could be larger if the mesured domain were increased. Reprinted with permission. Copyright 2007 American Chemical Society.

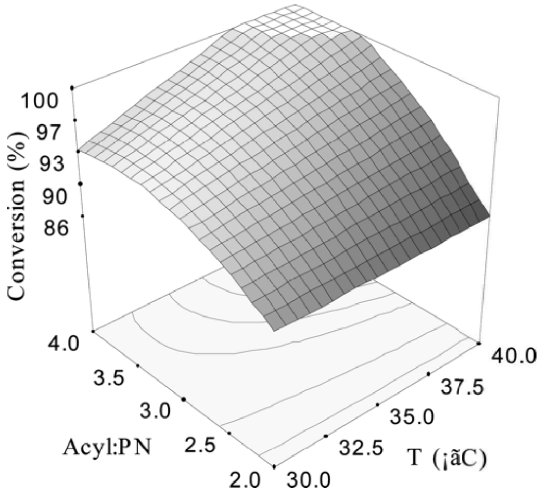

Figure 28: Yield of pyridoxine ester from lipase catalyzed reaction as a function of substrate molar ratio and temperature [19]. There is an optimal level set region. Reprinted with permission. Copyright 2007 American Chemical Society.

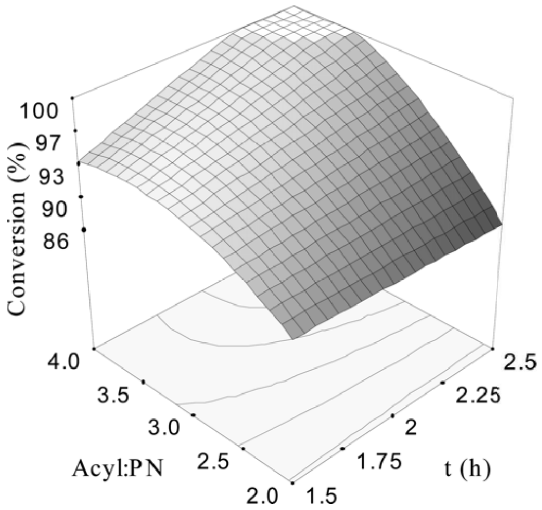

Figure 29: Yield of pyridoxine ester from lipase catalyzed reaction as a function of substrate molar ratio and reaction time [19]. There is an optimal level set region. Reprinted with permission. Copyright 2007 American Chemical Society.

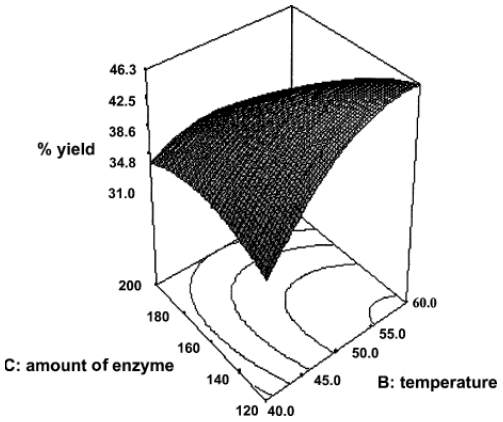

Figure 30: Yield of betulinic acid ester from lipase catalyzed acylation as a function of enzyme mole fraction and temperature [20]. The landscape is trap-free with the maximum at the upper limit of temperature and lower limit of enzyme amount. This is a projection of a three-dimensional landscape. Copyright Wiley-VCH Verlag GmbH & Co. KGaA. Reproduced with permission.

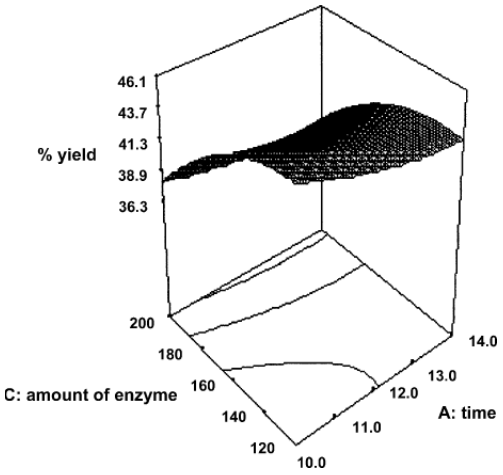

Figure 31: Yield of betulinic acid ester from lipase catalyzed acylation as a function of enzyme mole fraction and reaction time [20]. This is a projection of a three-dimensional landscape. Copyright Wiley-VCH Verlag GmbH & Co. KGaA. Reproduced with permission.

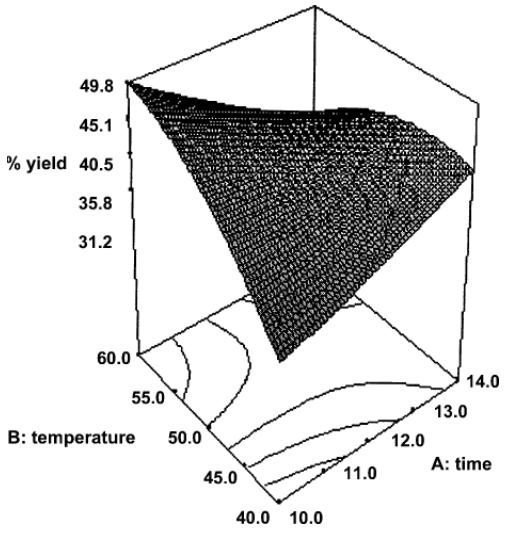

Figure 32: Yield of betulinic acid ester from lipase catalyzed acylation as a function of reaction time and temperature [20]. This is a projection of a three-dimensional landscape. Copyright Wiley-VCH Verlag GmbH & Co. KGaA. Reproduced with permission.

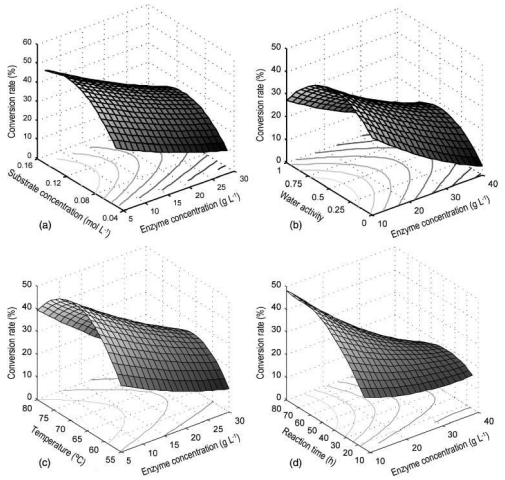

Figure 33: Yield of ascorbic acid ester versus enzyme concentration and substrate concentration (a), water content (b), temperature (c), and reaction time (d) [21]. These are projections from a five-dimensional landscape. Copyright Wiley-VCH Verlag GmbH & Co. KGaA. Reproduced with permission.

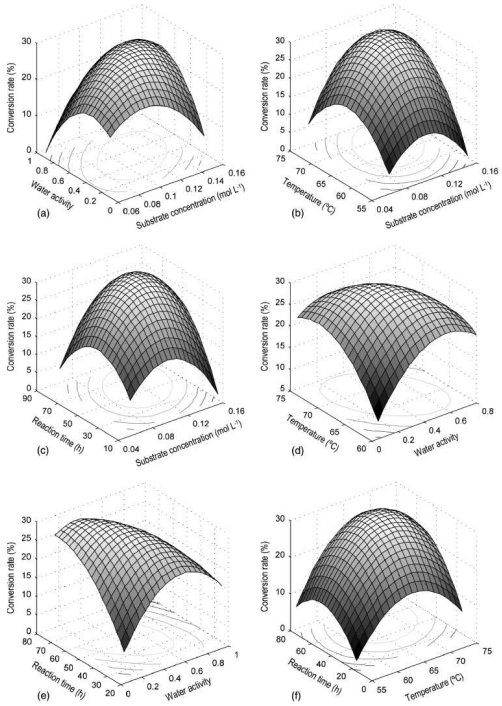

Figure 34: Yield of ascorbic acid ester versus water content and substrate concentration (a), temperature and substrate concentration (b), reaction time and substrate concentration (c), temperature and water content (d), reaction time and water content (e), and reaction time and temperature (f) [21]. These are the remaining projections on the five-dimensional landscape also in Figure 33. Copyright Wiley-VCH Verlag GmbH & Co. KGaA. Reproduced with permission.

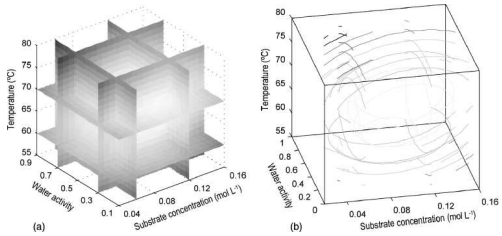

Figure 35: Yield of ascorbic acid ester versus the three variables water content, substrate concentration, and temperature [21]. The three-dimensional plot shows one global maximum in the center of the space, and is still a projection from the full five-dimensional landscape. Copyright Wiley-VCH Verlag GmbH & Co. KGaA. Reproduced with permission.

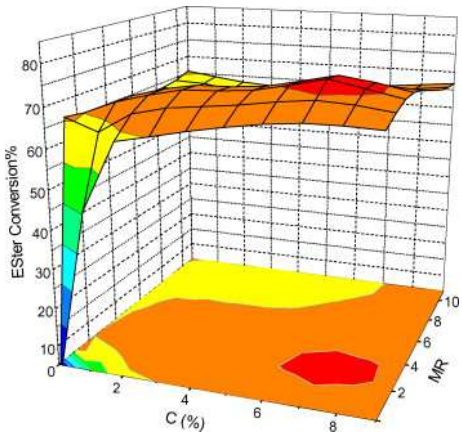

Figure 36: Yield of isopropyl esters versus enzyme concentration and substrate molar ratio. This plot is taken from experimental data [22]. Reprinted with permission from Elsevier. Copyright 2007.

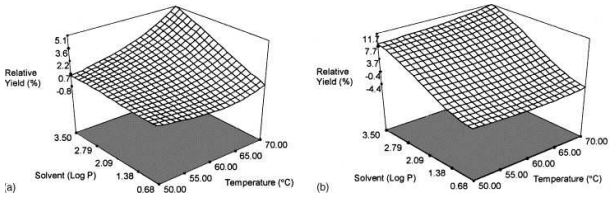

Figure 37: Yield of acylated lysine with palmitic acid (left) and oleic acid (right) as a function of temperature and solvent hydrophobicity [23]. Both landscapes are projections from full five-dimensional landscapes. Reprinted with permission from Elsevier. Copyright 2004.

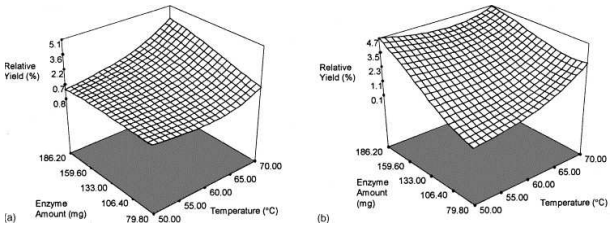

Figure 38: Yield of acylated lysine with palmitic acid (left) and oleic acid (right) as a function of temperature and lipase enzyme amount [23]. Both landscapes are projections from the same full five-dimensional landscapes in Figure 37. Reprinted with permission from Elsevier. Copyright 2004.

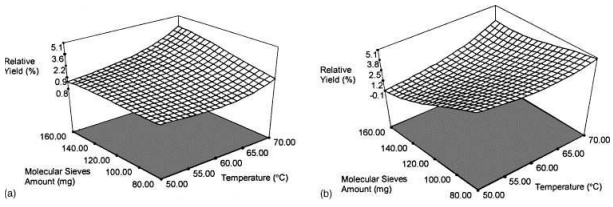

Figure 39: Yield of acylated lysine with palmitic acid (left) and oleic acid (right) as a function of temperature and molecular sieve amount [23]. Both landscapes are projections from the same full five-dimensional landscapes in Figure 37. Reprinted with permission from Elsevier. Copyright 2004.

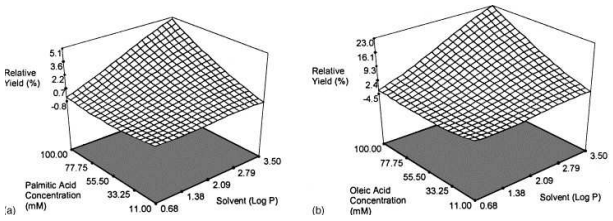

Figure 40: Yield of acylated lysine with palmitic acid (left) and oleic acid (right) as a function of solvent hydrophobicity and fatty acid concentration [23]. Both landscapes are projections from the same full five-dimensional landscapes in Figure 37. Reprinted with permission from Elsevier. Copyright 2004.

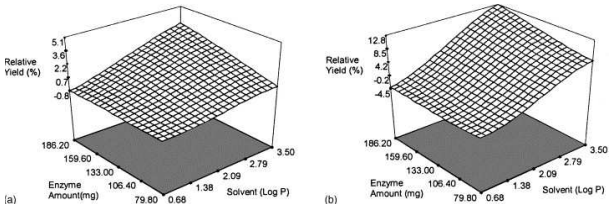

Figure 41: Yield of acylated lysine with palmitic acid (left) and oleic acid (right) as a function of solvent hydrophobicity and enzyme amount [23]. Both landscapes are projections from the same full five-dimensional landscapes in Figure 37. Reprinted with permission from Elsevier. Copyright 2004.

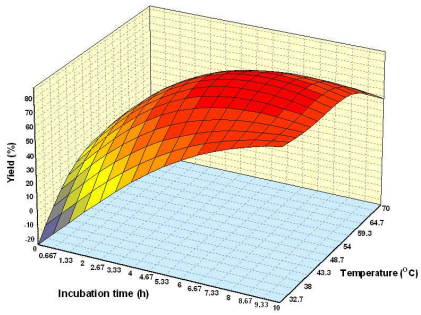

Figure 42: Yield of wax esters as a function of time and temperature [24]. This is a projection of a four-dimensional landscape.

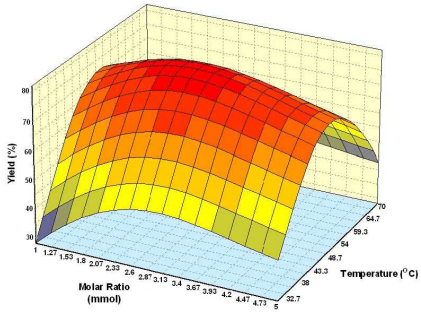

Figure 43: Yield of wax esters as a function of substrate molar ratio and temperature [24]. This is a projection of the four-dimensional landscape.

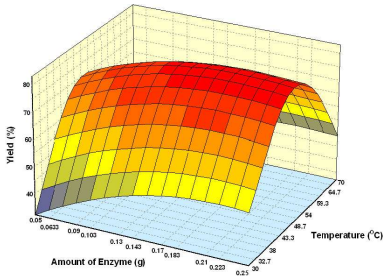

Figure 44: Yield of wax esters as a function of enzyme amount and temperature [24]. This is a projection of the four-dimensional landscape.

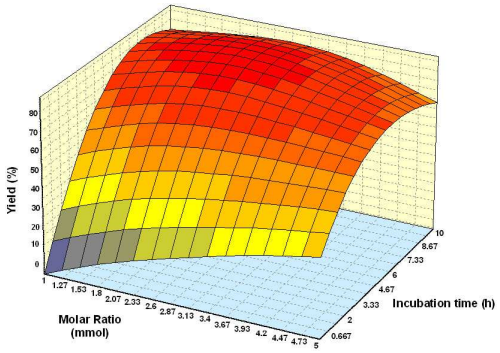

Figure 45: Yield of wax esters as a function of substrate molar ratio and time [24]. This is a projection of the four-dimensional landscape.

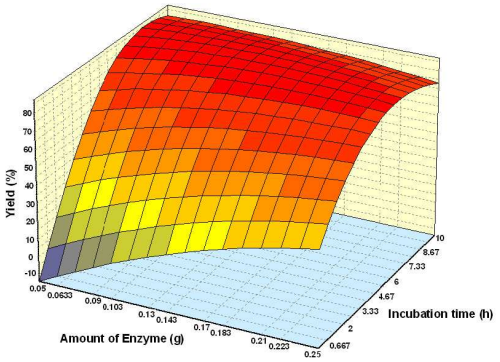

Figure 46: Yield of wax esters as a function of enzyme amount and time [24]. This is a projection of the four-dimensional landscape.

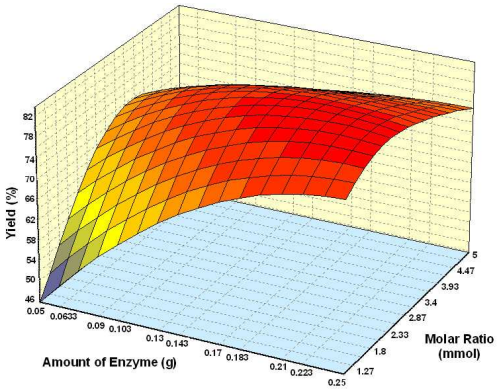

Figure 47: Yield of wax esters as a function of enzyme amount and substrate molar ratio [24]. This is a projection of the four-dimensional landscape.

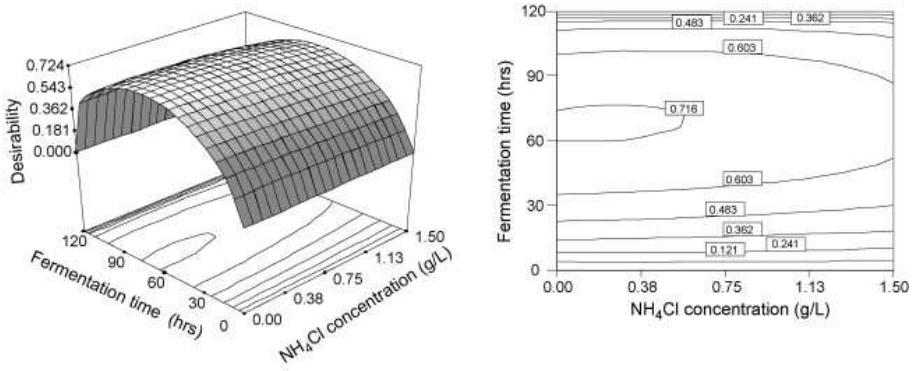

Figure 48: Cost function of acetic acid yield from bacteria versus fermentation time and NH_4Cl concentration [25]. The landscape for this multiobjective cost function is trap-free. Reprinted with permission from Elsevier. Copyright 2008.

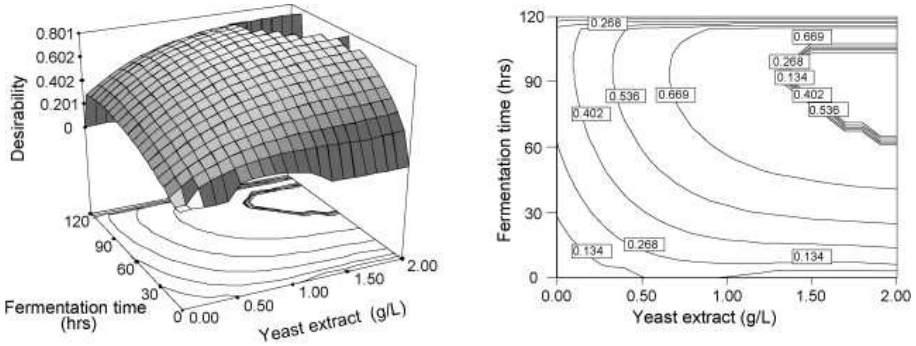

Figure 49: Cost function of acetic acid yield from bacteria versus fermentation time and yeast extract concentration [25]. The landscape for this multiobjective cost function is trap-free. Reprinted with permission from Elsevier. Copyright 2008.

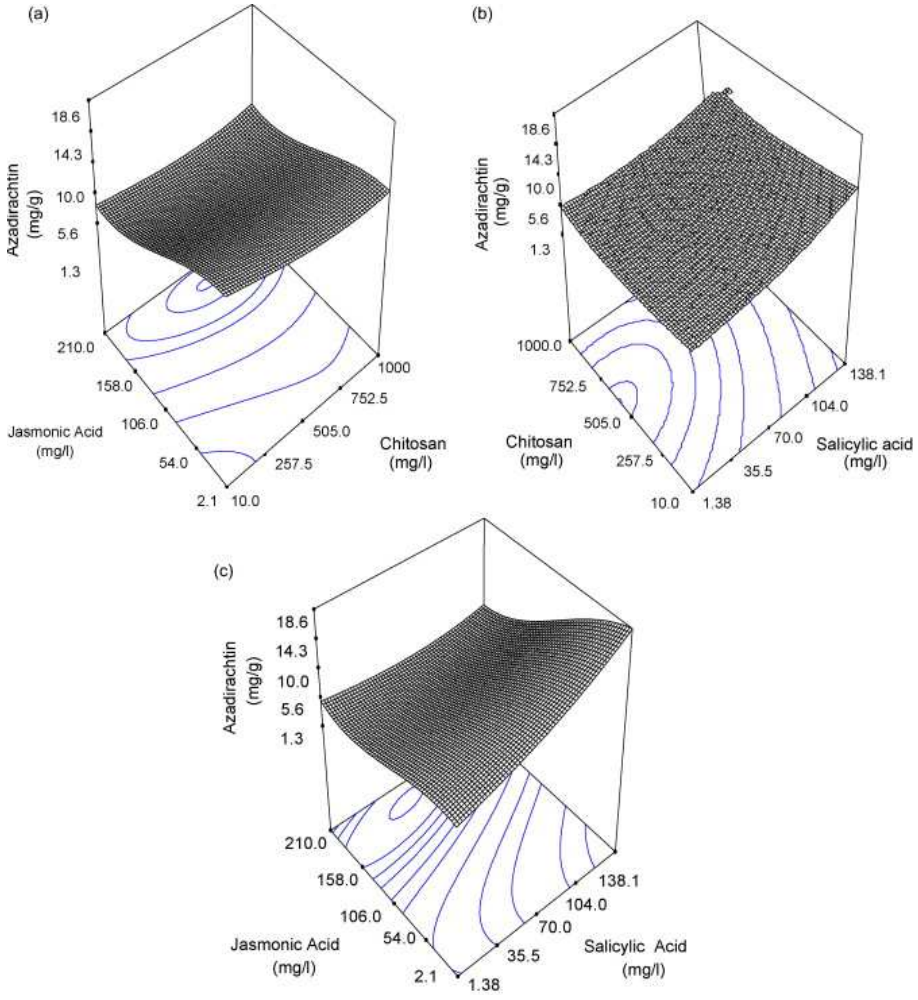

Figure 50: Yield of azadirachtin as a function of the concentrations of jasmonic acid and chitosan (a), chitosan and salicylic acid (b), and jasmonic acid and salicylic acid (c) [26]. These are projections of a three-dimensional landscape. Reprinted with permission from Elsevier. Copyright 2008.

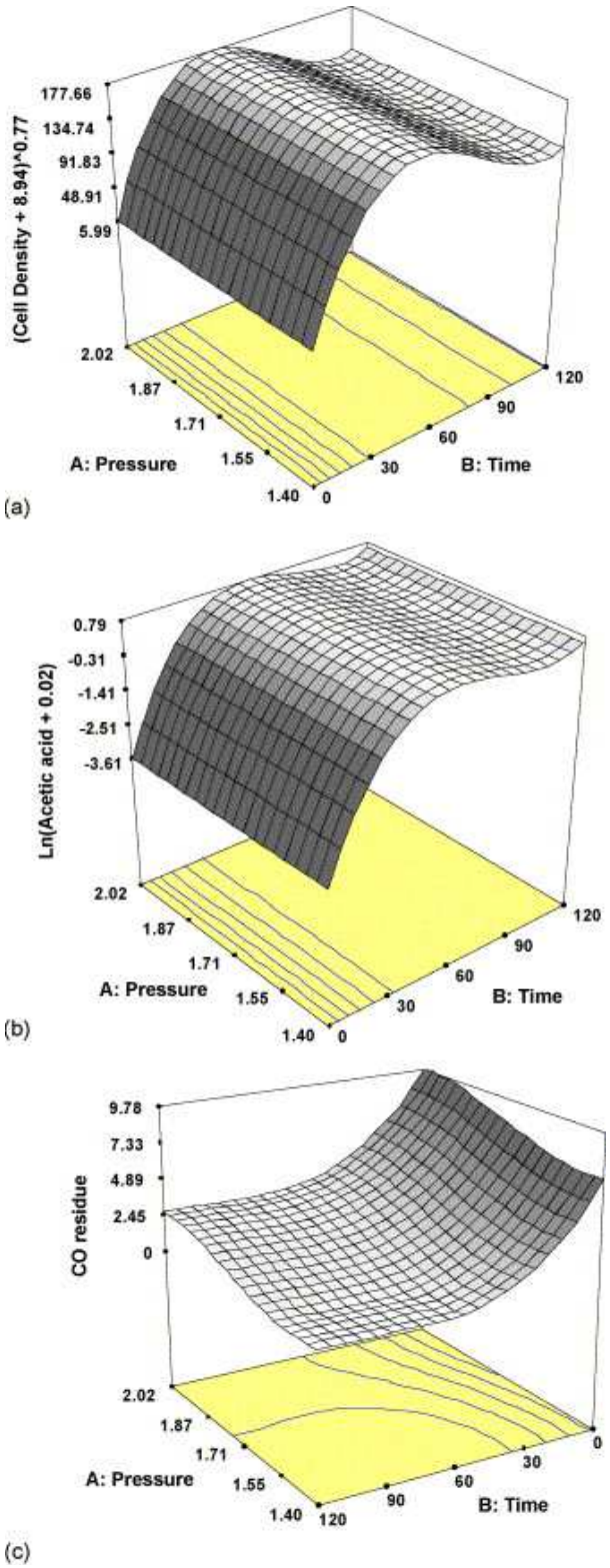

Figure 51: Synthesis of acetic acid as measured by (a) cell density of *Clostridium aceticum*, (b) acetic acid yield, and (c) residual CO [27]. CO partial pressure and reaction time are variables. Reprinted with permission from Elsevier. Copyright 2007.

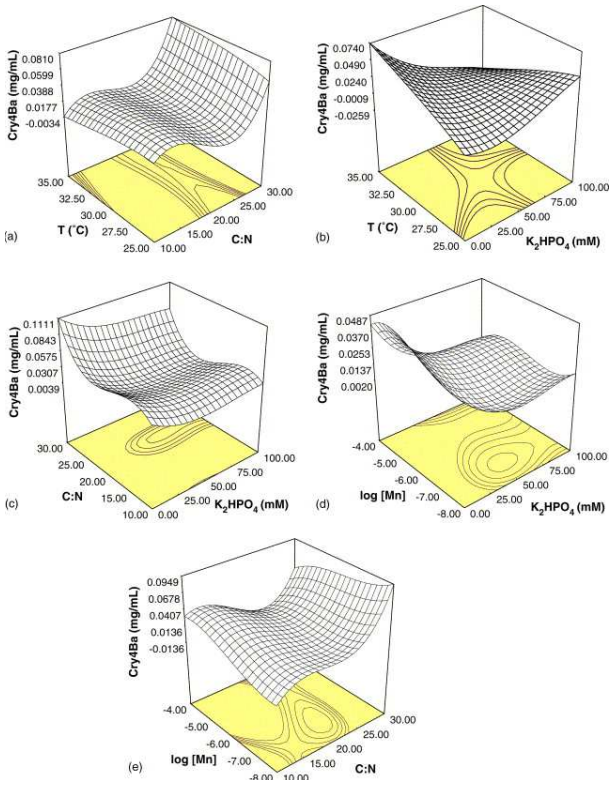

Figure 52: Yield of Cry4Ba as a function of (a) temperature and C:N ratio, (b) temperature and K_2HPO_4 concentration, (c) C:N ratio and K_2HPO_4 concentration, (d) Mn and K_2HPO_4 concentration, and (e) C:N ratio and Mn concentration [28]. These are projections on a four-dimensional landscape. Reprinted with permission from Elsevier. Copyright 2006.

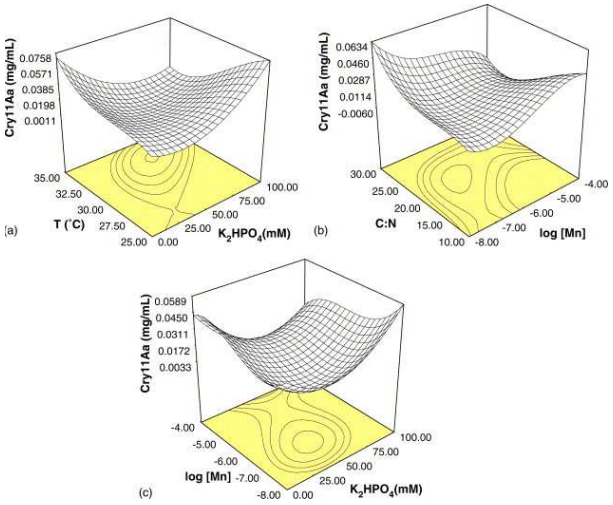

Figure 53: Yield of Cry11Aa as a function of (a) temperature and K_2HPO_4 concentration, (b) C:N ratio and Mn concentration, and (c) Mn and K_2HPO_4 concentration [28]. These are projections on a four-dimensional landscape. Reprinted with permission from Elsevier. Copyright 2006.

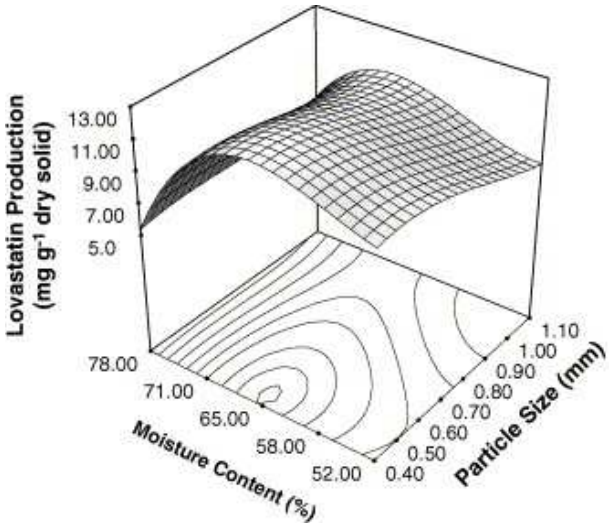

Figure 54: Yield of lovastatin from *Aspergillus flavipes* as a function of water content and particle size of wheat bran food substrate [29]. Reprinted with permission from Elsevier. Copyright 2005.

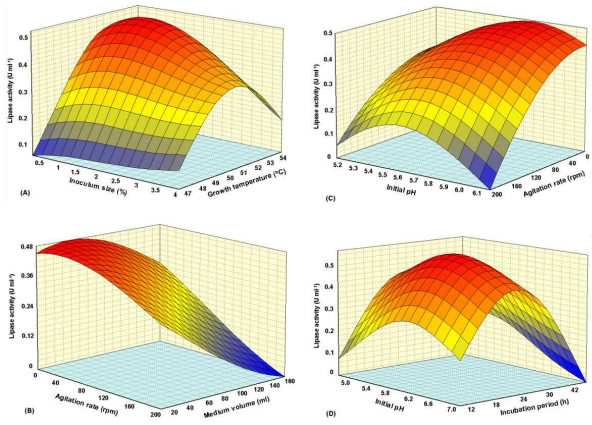

Figure 55: Recorded lipase activity (proportional to lipase yield) as a function of (a) temperature and inocolum size, (b) agitation rate and medium volume, (c) initial pH and agitation rate, and (d) initial pH and incubation time [30]. These are projections on a five-dimensional landscape.

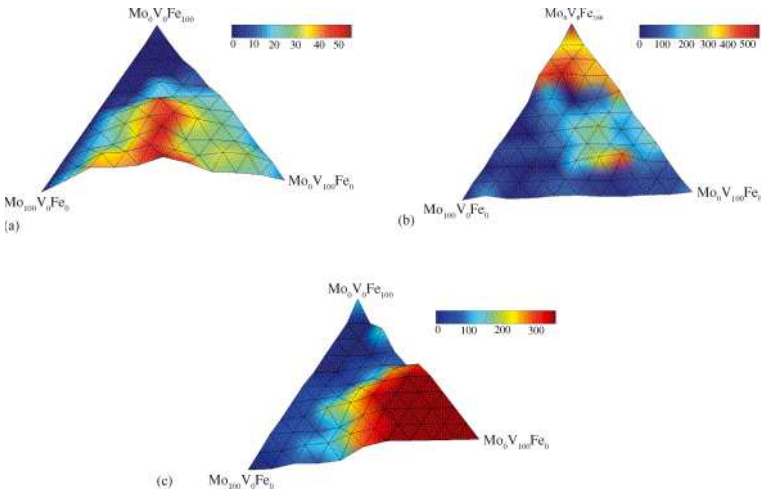

Figure 56: Relative catalytic yield for oxidation of isobutane to methacrolein (a), isobutene (b) and CO_2 (c) by a Mo-V-Fe catalyst system [31]. The isobutene landscape may contain a trap. Reprinted with permission from Elsevier. Copyright 2004.

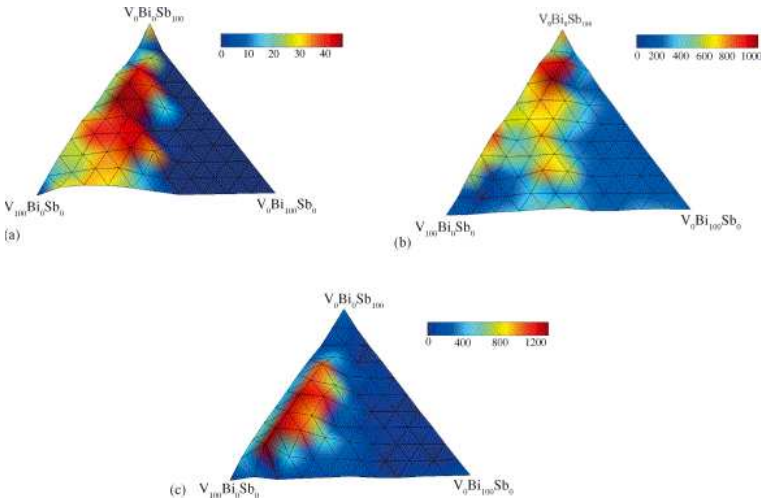

Figure 57: Relative catalytic yield for oxidation of isobutane to methacrolein (a), isobutene (b) and CO_2 (c) by a V-Bi-Sb catalyst system [31]. The isobutene landscape may contain a trap. Reprinted with permission from Elsevier. Copyright 2004.

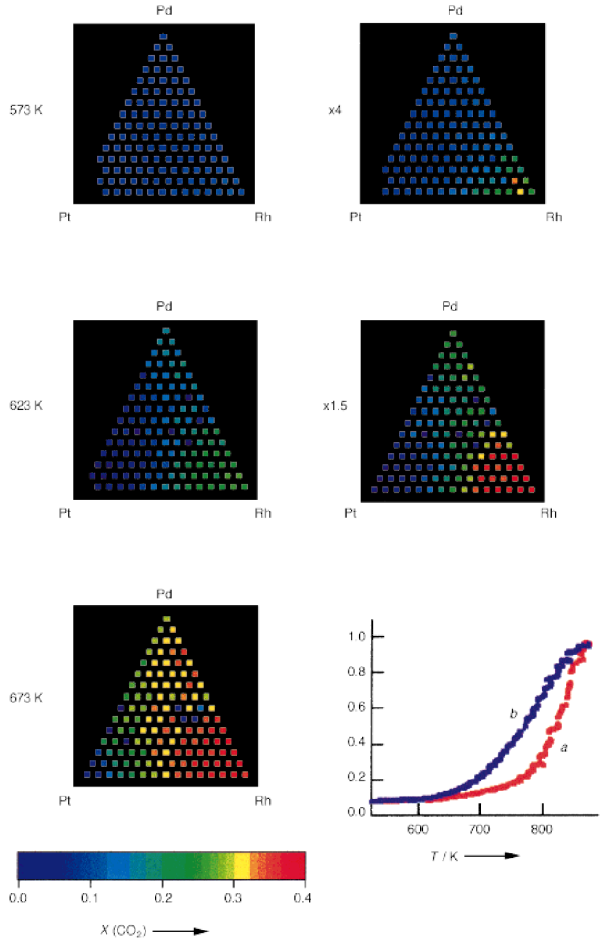

Figure 58: Catalytic activity of the reaction CO→CO_2 for Rh-Pd-Pt catalysts, measured at 573K (top; the landscape on the right is identical to that on the left, but rescaled to clearly show the activity range), 623K (middle; the landscape on the right is identical to that on the left, but rescaled to clearly show the activity range), and 673K (bottom). The figure in the lower right-hand corner plots CO_2 yield as a function of temperature for pure Pt with heating (red) and cooling (blue). (Figure 2 from [32]). Although all landscapes show a clear trend toward increasing ativity with Rh content, the landscape at 673K contains a striking discontinuity near the optimal region. The authors attribute this to the fact that the catalysts undergo a kinetic phase transition around this temperature. Copyright Wiley-VCH Verlag GmbH & Co. KGaA. Reproduced with permission.

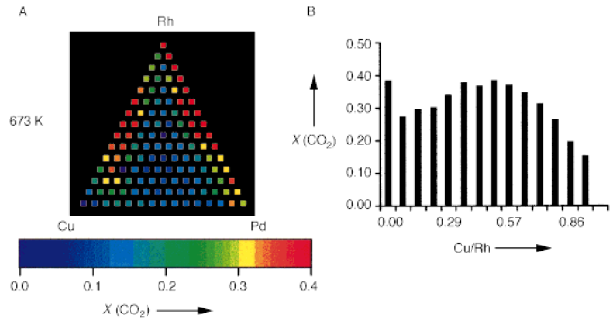

Figure 59: Yield of CO_2 from CO by Cu-Rh-Pd oxidation catalyst library (A) [32]. There are two isolated maxima, which are of equal height, according to the projection on the Rh-Cu axis (B). Copyright Wiley-VCH Verlag GmbH & Co. KGaA. Reproduced with permission.

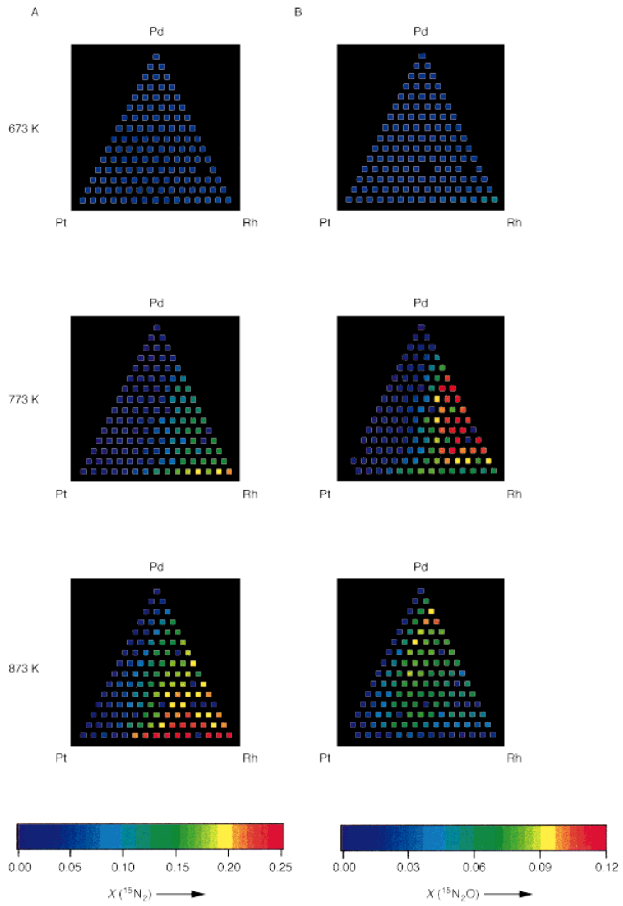

Figure 60: Yield of N_2(A) and N_2O (B) from Rh-Pd-Pt library from oxidation of CO by NO [32], at 673K (top), 773K (middle), and 873K (bottom). The landscapes are trap-free, with some discontinuities, as for the Rh-Pd-Pt library for the oxidation of CO by O_2 in Figure 58. Copyright Wiley-VCH Verlag GmbH & Co. KGaA. Reproduced with permission.

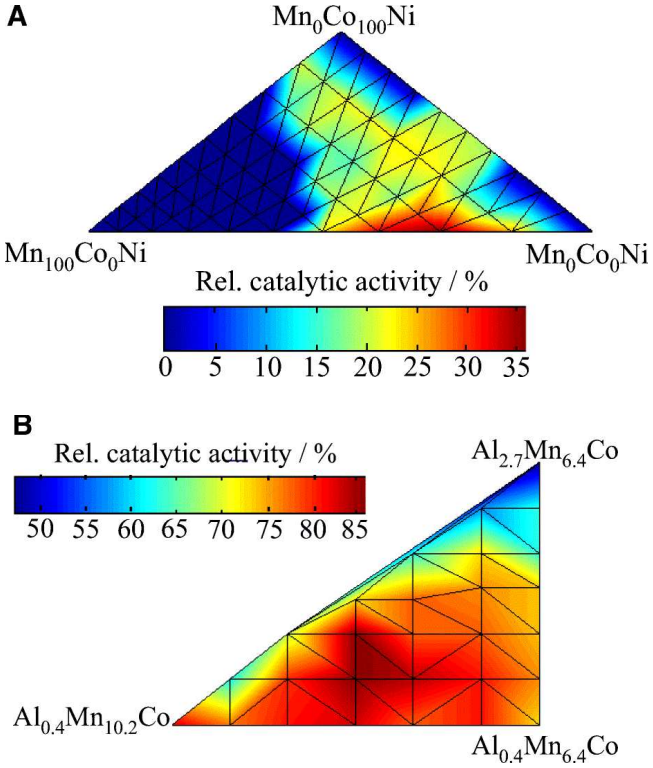

Figure 61: Relative catalytic activity (to a reference literature catalyst) of Mn-Co-Ni library (A) and Mn-Co-Al library (B) for reaction $CO+O_2 \rightarrow CO_2$ [33]. Both landscapes are trap-free. Reprinted with permission from Elsevier. Copyright 2004.

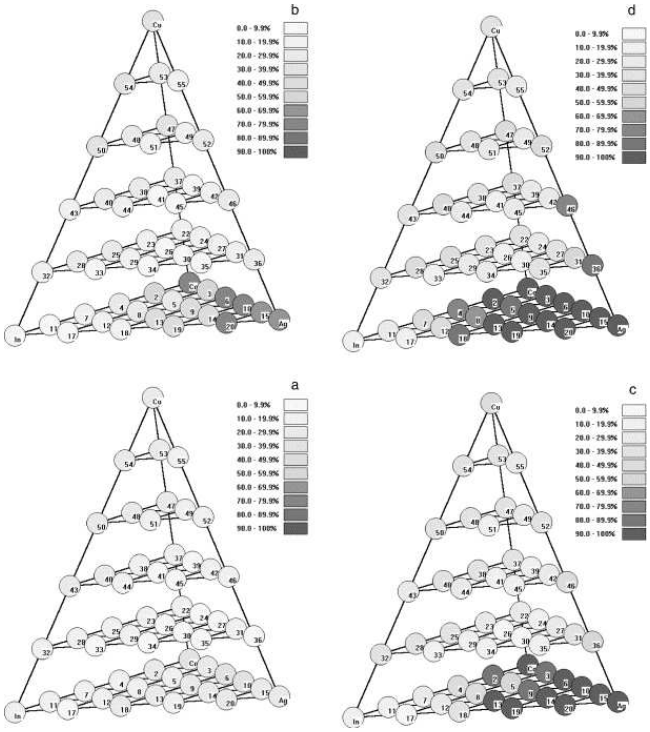

Figure 62: Conversion of NO by In-Ag-Co-Cu catalysts at 400°C (a), 425°C (b), 450°C (c) and 475°C (d) [34]. All landscapes are trap-free. Reprinted with permission from Elsevier. Copyright 2002.

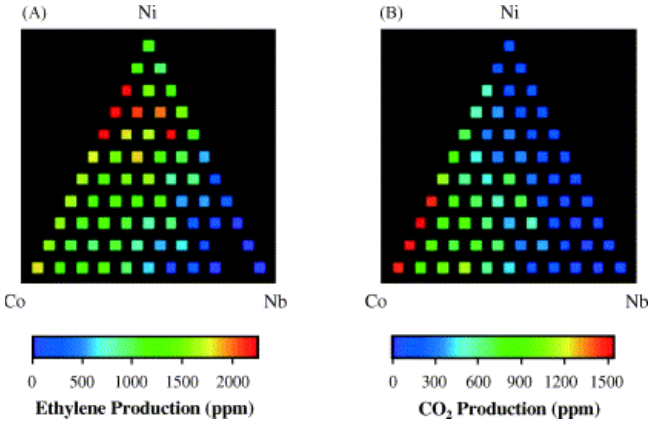

Figure 63: Yield of ethylene (a) and CO_2 (b) for Ni-Co-Nb library [36]. Both landscapes are trap-free. Reprinted with permission from Elsevier. Copyright 2003.

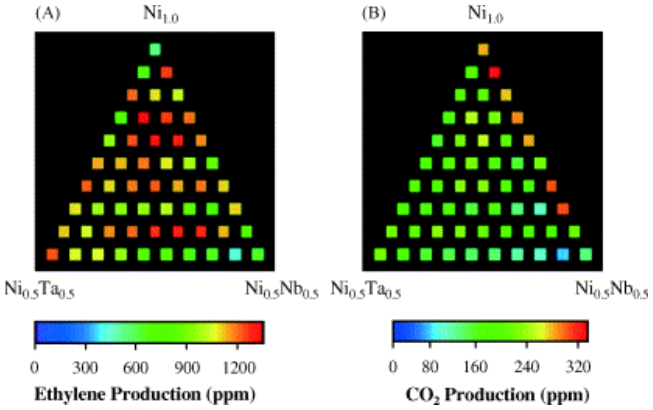

Figure 64: Yield of ethylene (a) and CO_2 (b) for Ni-Ta-Nb library [36]. The landscape for ethylene production may contain traps. Reprinted with permission from Elsevier. Copyright 2003.

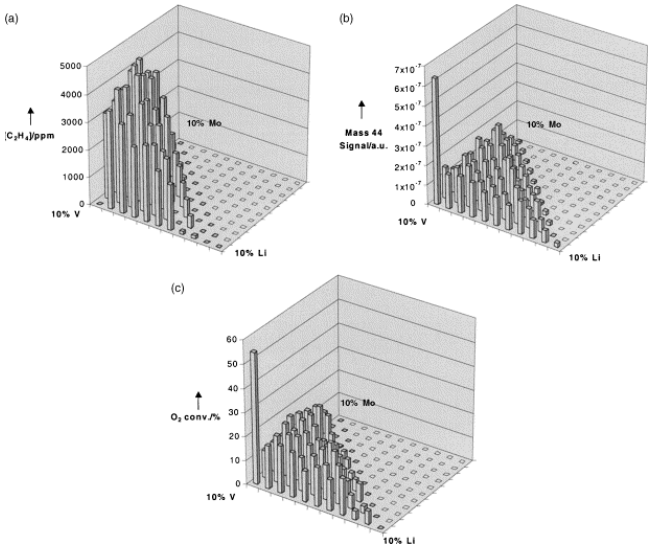

Figure 65: Yield of ethylene (a), CO_2 (b), and O_2 consumption (c) for ethane oxidation by a V-Mo-Li library [38]. All landscapes are trap-free. Reprinted with permission from Elsevier. Copyright 2003.

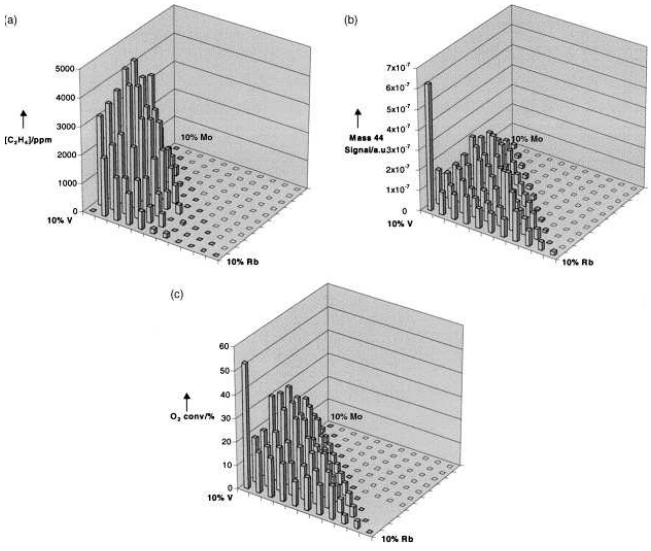

Figure 66: Yield of ethylene (a), CO_2 (b), and O_2 consumption (c) for ethane oxidation by a V-Mo-Rb library [38]. All landscapes are trap-free. Reprinted with permission from Elsevier. Copyright 2003.

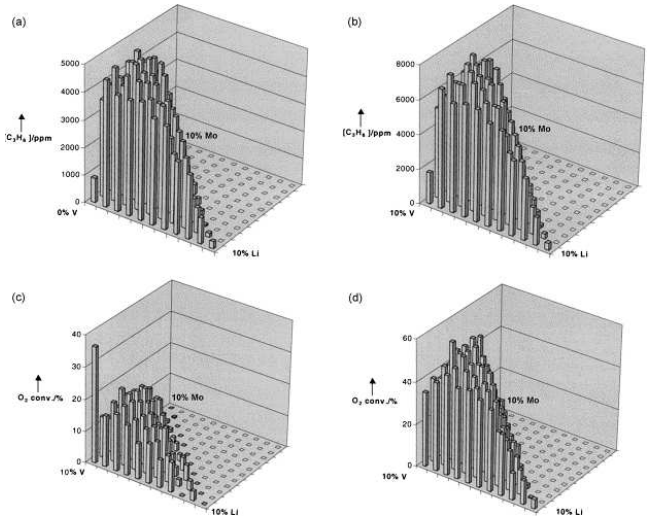

Figure 67: Yield of propylene (a), (b) and O_2 consumption (c), (d) for propane oxidation by a V-Mo-Li library at molar ratios propane:O_2 =2:1 (a,c) and propane:O_2 =1:1 (b,d) [38]. All landscapes are trap-free. Reprinted with permission from Elsevier. Copyright 2003.

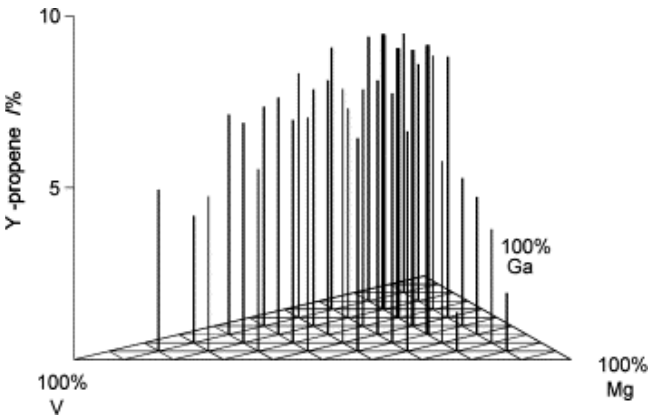

Figure 68: Propene yield from a V-Mg-Ga library [39]. The landscape is trap-free to within a reasonable degree of noise. Reprinted with permission from Elsevier. Copyright 2001.

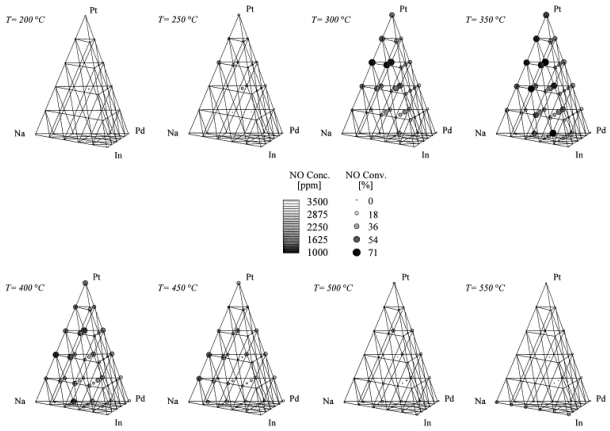

Figure 69: Consumption of NO for Na-Pt-Pd-In library, recorded at eight different temperatures [40]. The landscapes at 250°C and 300°C are trap-free. These are four-dimensional projections of a five-dimensional landscape, with the fifth variable being temperature. Reprinted with permission from Elsevier. Copyright 2000.

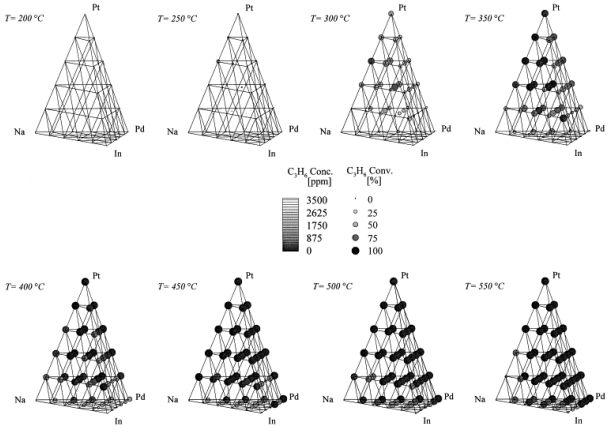

Figure 70: Consumption of propene for Na-Pt-Pd-In library, recorded at eight different temperatures [40]. The landscapes at 350°C and higher temperatures are trap-free. These are four-dimensional projections of a five-dimensional landscape, with the fifth variable being temperature. Reprinted with permission from Elsevier. Copyright 2000.

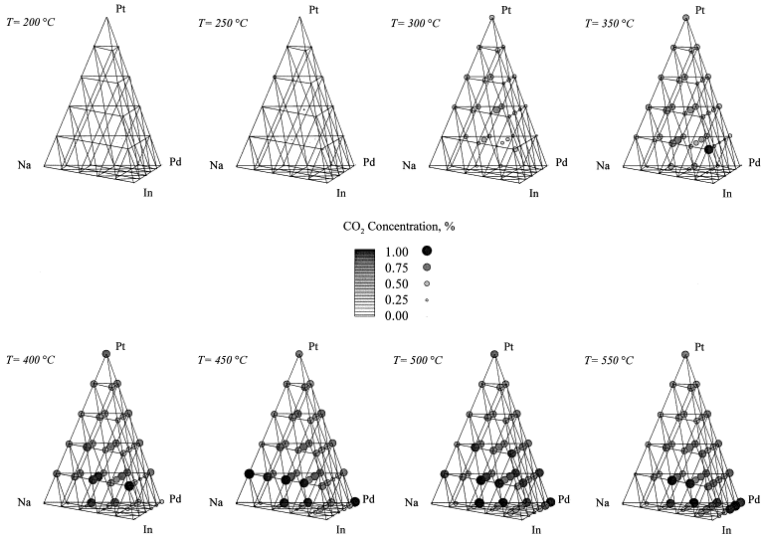

Figure 71: Production of CO_2 for Na-Pt-Pd-In library, recorded at eight different temperatures [40]. The landscapes at 500°C and 550°C are trap-free. These are four-dimensional projections of a five-dimensional landscape, with the fifth variable being temperature. Reprinted with permission from Elsevier. Copyright 2000.

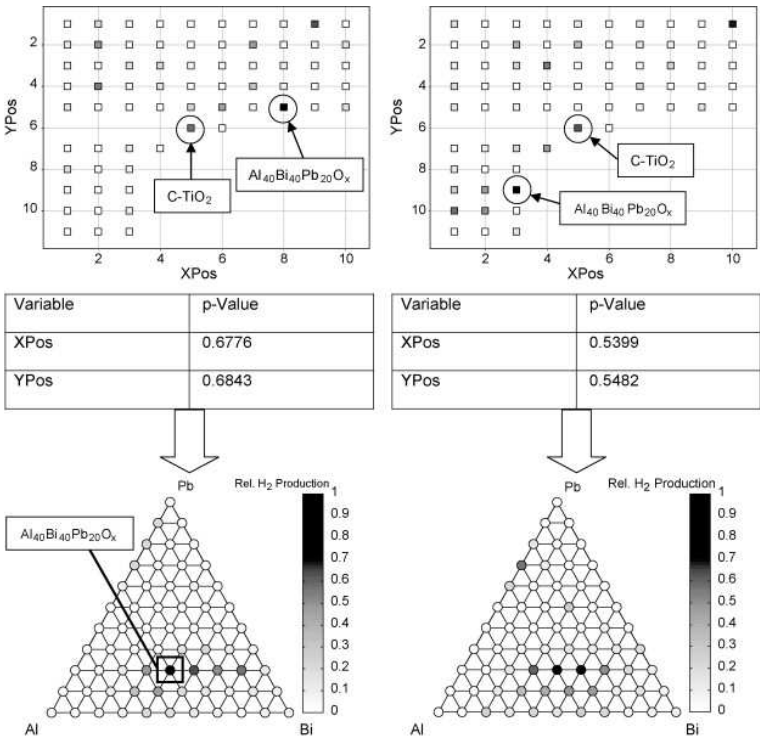

Figure 72: Relative catalytic conversion of methanol to H_2 by Al-Bi-Pb catalysts under photoexcitation [41]. The top of the figure shows the process of positioning the test material compositions under the light source. The positioning of each material composition under the light source was different for the landscapes on the left and right, but the landscapes produced are similar. Reprinted with permission from Elsevier. Copyright 2007.

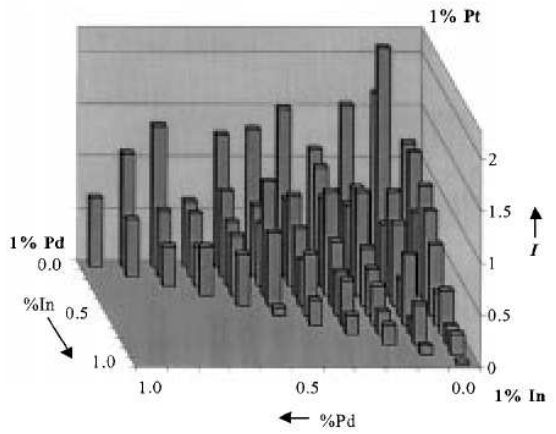

Figure 73: Catalytic activity of cyclohexane to benzene conversion for a Pt-Pd-In library [42]. The landscape is trap-free to within a reasonable level of noise. Copyright Wiley-VCH Verlag GmbH & Co. KGaA. Reproduced with permission.

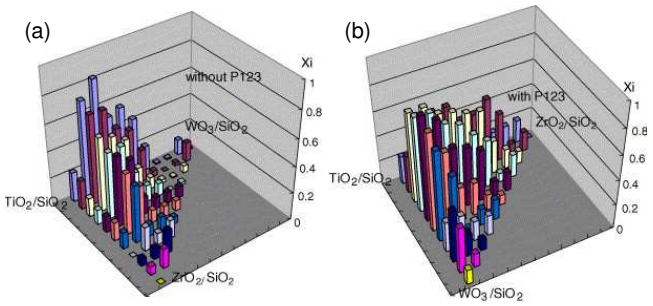

Figure 74: Catalytic activity of 1,6-hexamethylenediamine degradation over W-Ti-Zr libraries (a) without template P123 and (b) with template P123 [43]. The addition of P123 increases catalytic activity and removes the trap at the WO_3 corner of the landscape (a). Reprinted with permission from Elsevier. Copyright 2005.

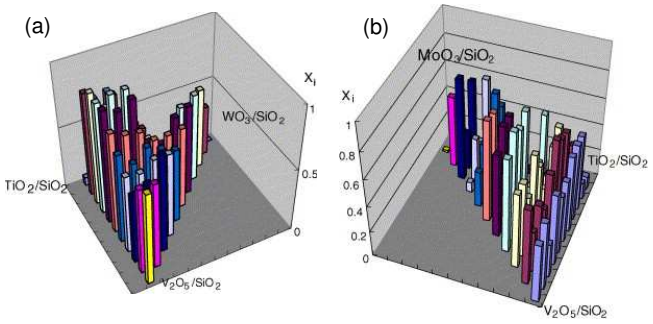

Figure 75: Catalytic activity of 1,6-hexamethylenediamine degradation over W-Ti-V (a) and V-Ti-Mo (b) libraries [43]. The W-Ti-V landscape appears trap-free, but the V-Ti-Mo landscape may contain traps. The error in catalytic measurement was not reported, so it is not possible to discern whether the apparent traps result from uncertainty in the measurements. Reprinted with permission from Elsevier. Copyright 2005.

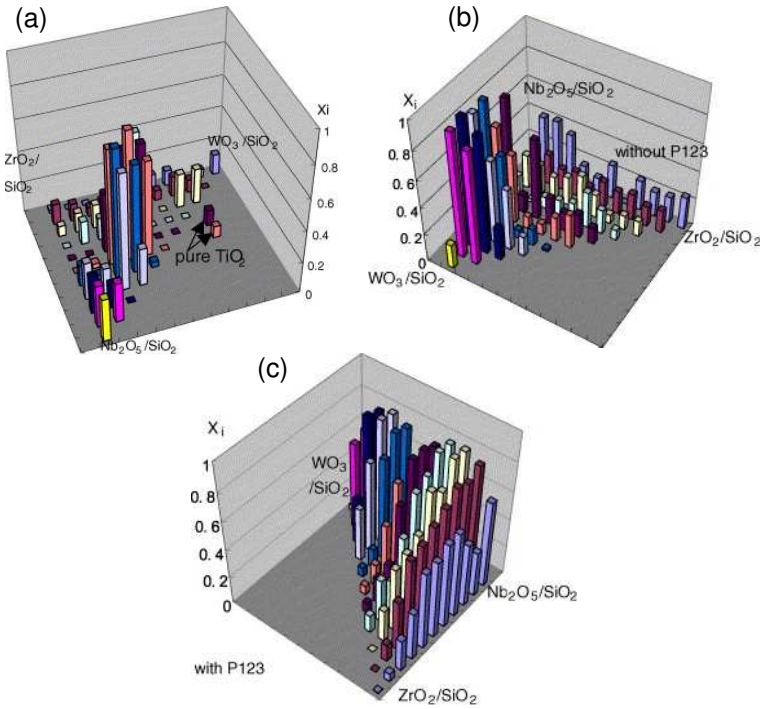

Figure 76: Catalytic activity of 1,6-hexamethylenediamine degradation over W-Ti-Nb libraries prepared by (a) tungsten precursor=$(NH_4)_5H_5[H_2(WO_4)_6]\cdot H_2O$ in ethanol, (b) tungsten precursor=WCl_6 in ethanol, no P123, and (c) tungsten precursor=WCl_6 in ethanol, with P123 [43]. The use of WCl_6 and P123 generates the most overall catalytic activity and the most evident trap-free landscape. Reprinted with permission from Elsevier. Copyright 2005.

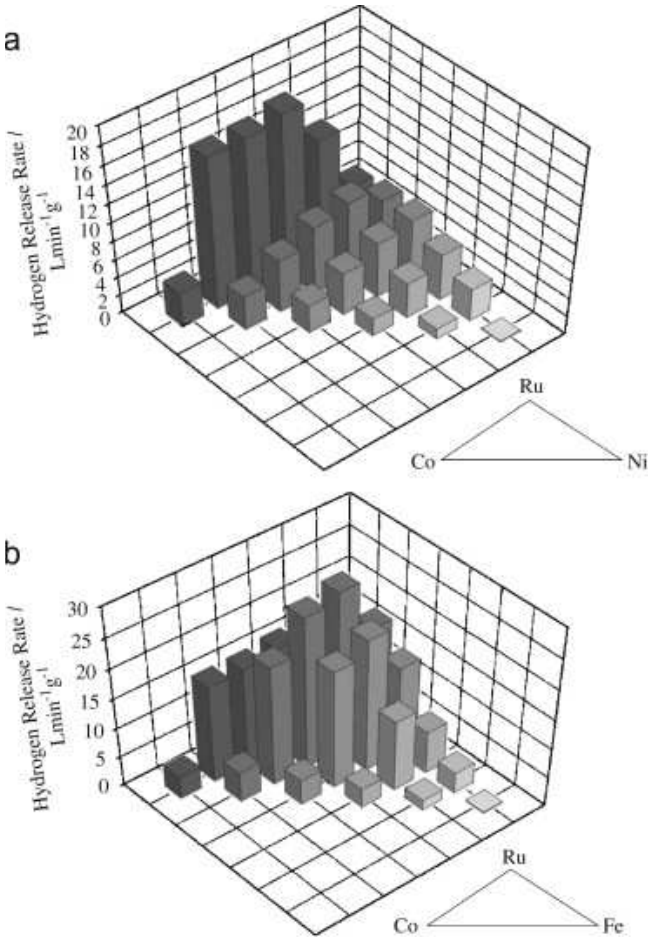

Figure 77: Rate of H_2 formation from $NaBH_4$ by libraries of Ru-Co-Ni (a) and Ru-Co-Fe (b) catalysts [44]. Both landscapes are trap-free. Reprinted with permission from Elsevier. Copyright 2008.

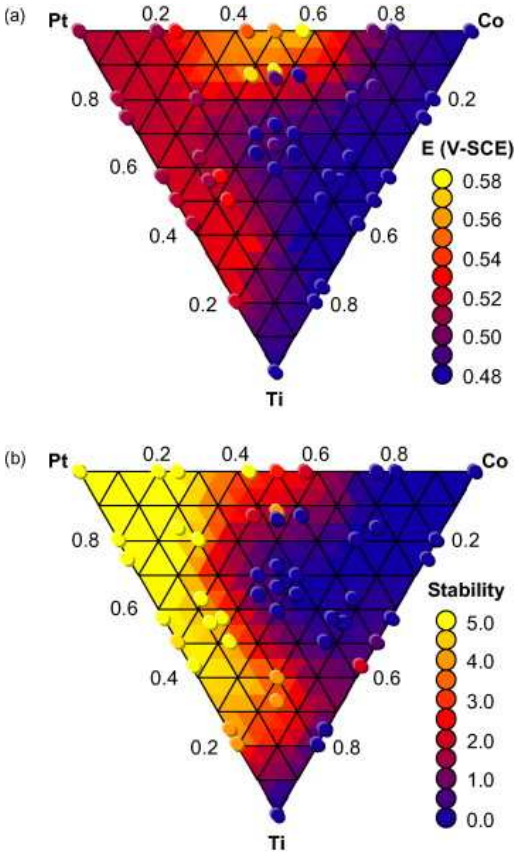

Figure 78: Landscapes for onset potential for O_2 reduction (a) and stability to corrosion (b) of a Pt-Co-Ti library [45]. Both landscapes are trap-free. Reprinted with permission from Elsevier. Copyright 2007.

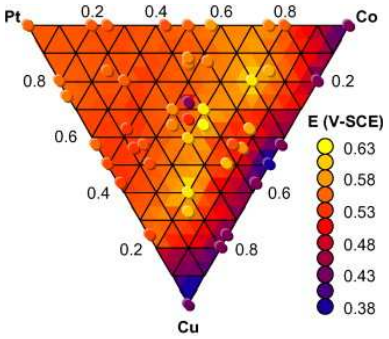

Figure 79: Landscape for onset potential for O_2 reduction of a Pt-Co-Cu library [45]. The landscape is trap-free. Reprinted with permission from Elsevier. Copyright 2007.

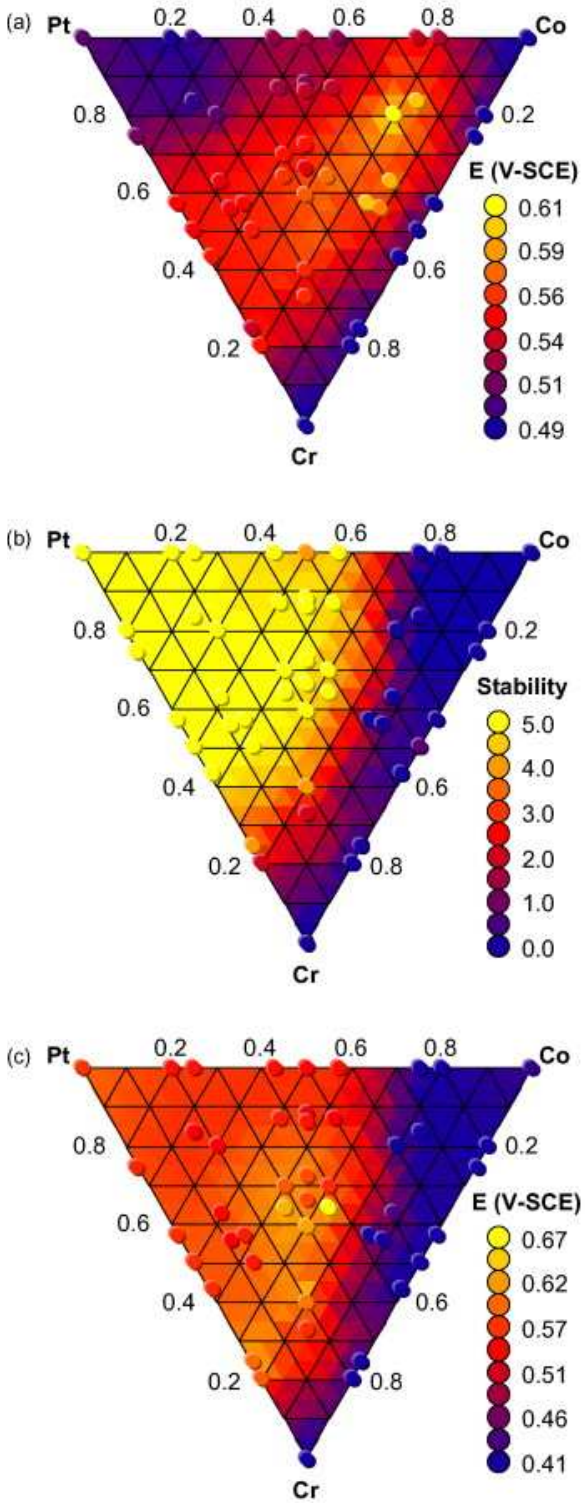

Figure 80: Landscapes for onset potential for O_2 reduction (a), stability to corrosion (b) of a Pt-Co-Cr library; stability to corrosion of a Pt-Co-Cu library (c) [45]. All landscapes are trap-free. The landscape is trap-free. Reprinted with permission from Elsevier. Copyright 2007.

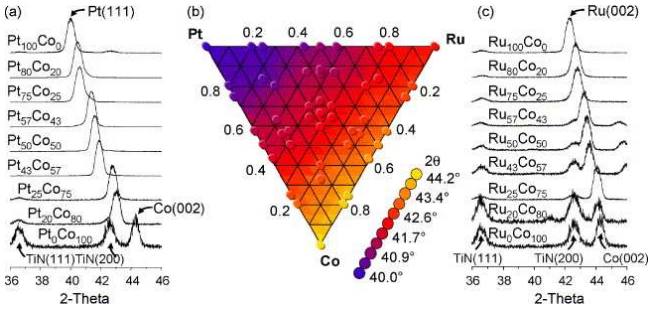

Figure 81: X-ray diffraction scans of Pt-Co compositions (a), landscape of the X-ray diffraction 2θ shift versus composition for a Pt-Ru-Co library (b), and X-ray diffraction scans of Ru-Co compositions (c) [46]. The landscape (b) is trap-free. The landscape is trap-free. Reprinted with permission from Elsevier. Copyright 2006.

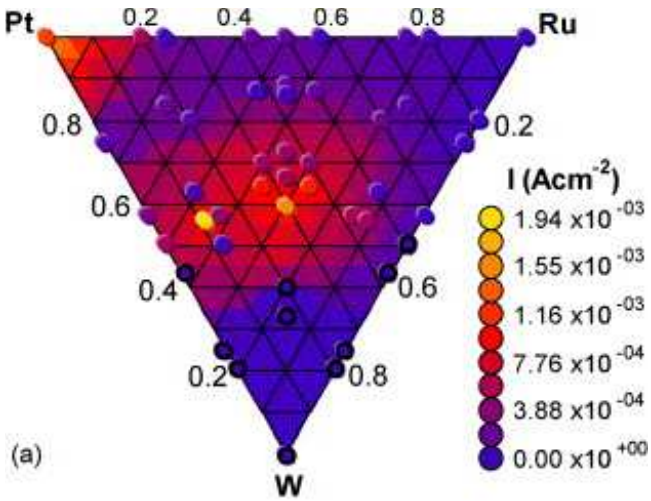

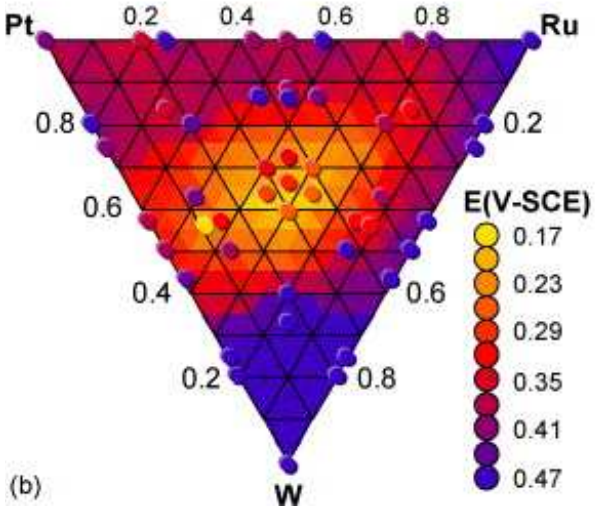

Figure 82: Landscapes for peak current (a) and onset potential for oxidation reaction (b) for a Pt-Ru-W library [46]. There may be traps in the landscape (a), but sparse sampling [46] may cause only apparent traps. The landscape is trap-free. Reprinted with permission from Elsevier. Copyright 2006.

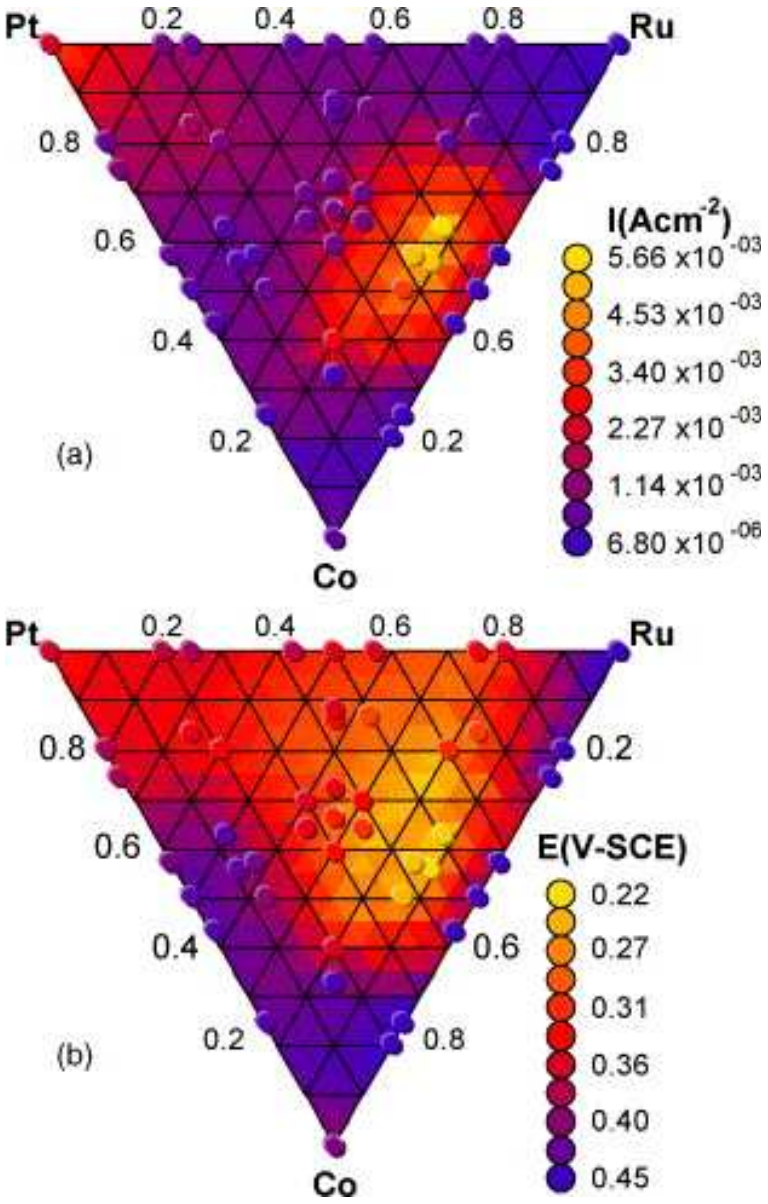

Figure 83: Landscapes for peak current (a) and onset potential for oxidation reaction (b) for a Pt-Ru-Co library [46]. These landscapes are trap-free. The landscape is trap-free. Reprinted with permission from Elsevier. Copyright 2006.

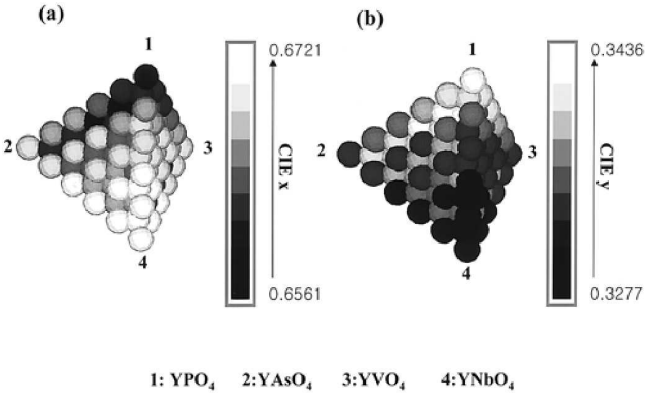

Figure 84: CIE color chromaticity x (a) and y (b) of phosphors versus composition, as labeled on the figure [48]. The landscapes appear to be trap-free. Reprinted with permission. Copyright 2002 American Chemical Society.

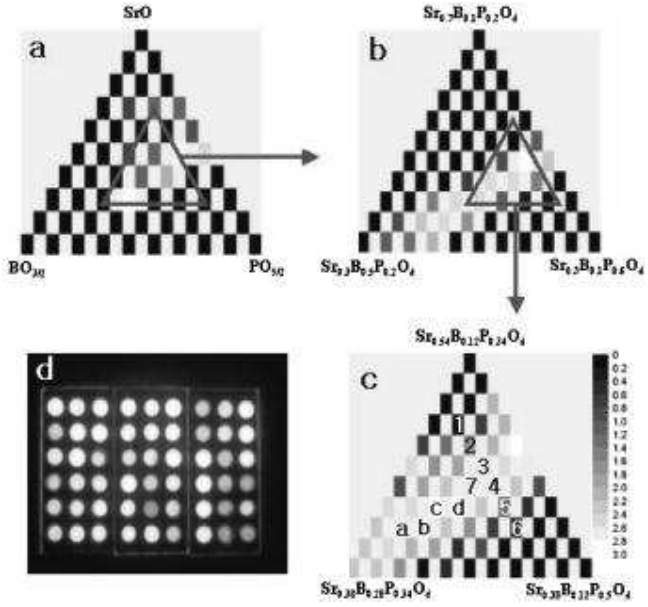

Figure 85: Luminescent intensity for a Sr-B-P library [49]. The full search space is shown in (a), and two subsequent fine-tuning libraries around the optimum are shown in (b) and (c). All of the landscapes appear to be trap-free. Copyright 2005, The Electrochemical Society. Reproduced with permission.

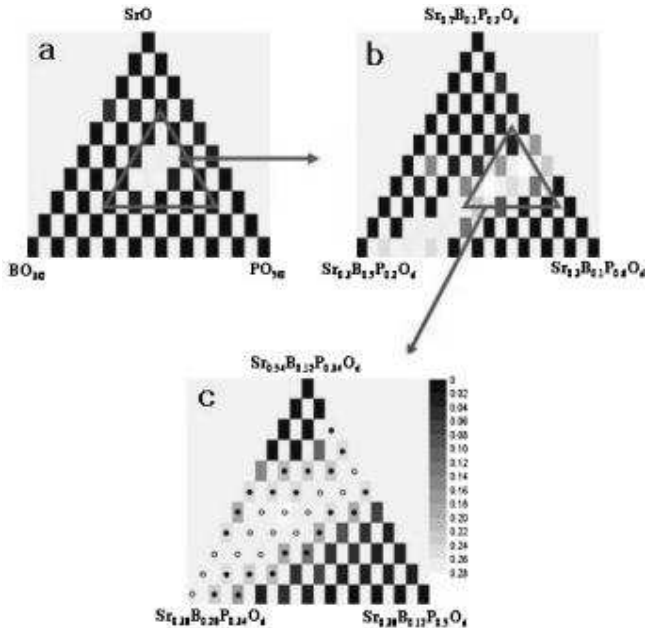

Figure 86: CIE color chromaticity in the y direction for the Sr-B-P library [49]. The full search space is shown in (a), and fine-tuning around the optimum is shown in (b) and (c). The landscape for this property is trap-free. Copyright 2005, The Electrochemical Society. Reproduced with permission.

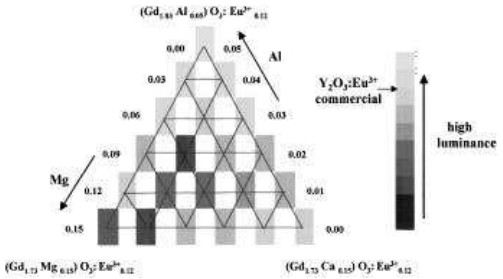

Figure 87: Red luminescence under 246nm excitation radiation for a Al-Mg-Ca phosphor library [50]. Only a small region of search space was measured, producing this trap-free landscape. Copyright 2002, The Electrochemical Society. Reproduced with permission.

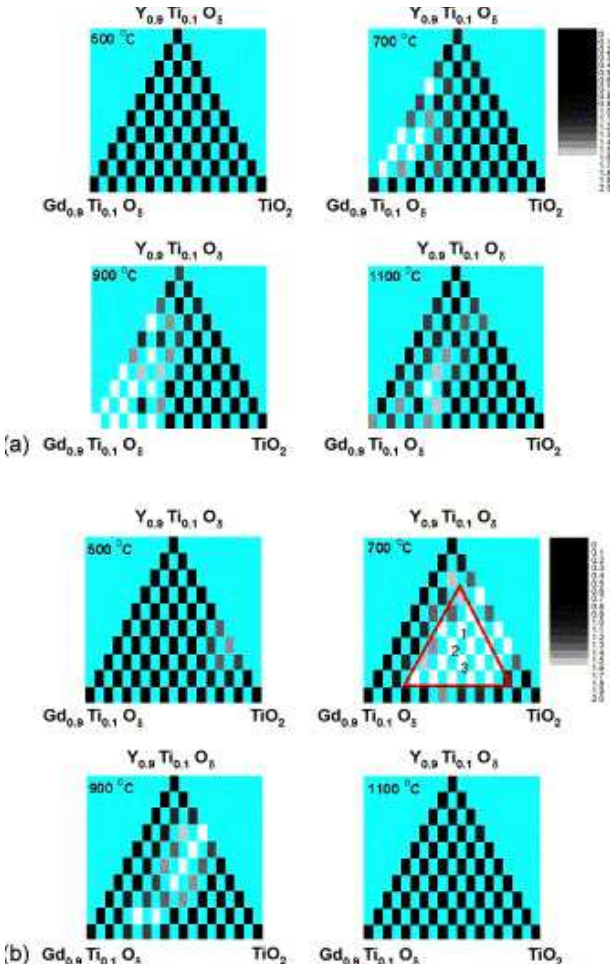

Figure 88: Red luminescent intensity for a Ti-Y-Gd library under excitation at 254nm (a) and 400nm (b) for four different firing temperatures [51]. The landscapes at 700°C firing temperature are trap-free. The landscapes in (a) and (b) are projections on four-dimensional landscapes, with the fourth variable being firing temperature. Reprinted with permission from Elsevier. Copyright 2008.

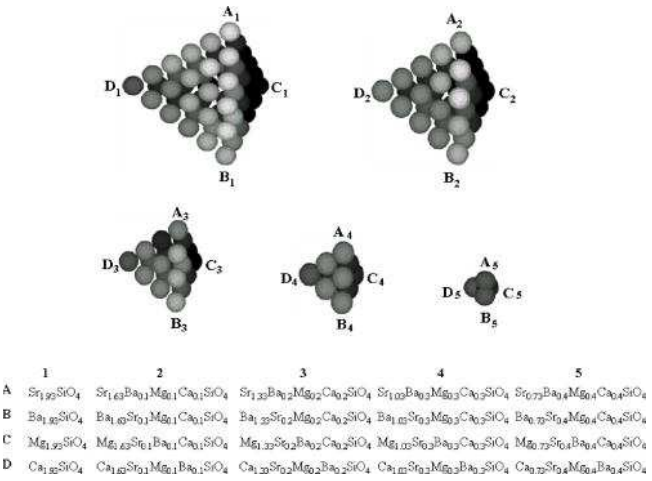

Figure 89: Blue luminescent intensity for a Sr-Ba-Mg-Ca library under 400nm excitation radiation [52]. The full landscape is shown at the left, labelled [A_1 B_1 C_1 D_1], the remaining landscapes are subsets of the full landscape. Since none of the subset landscapes contain obvious traps, the full landscape appears to be trap-free. Copyright 2007, The Electrochemical Society. Reproduced with permission.

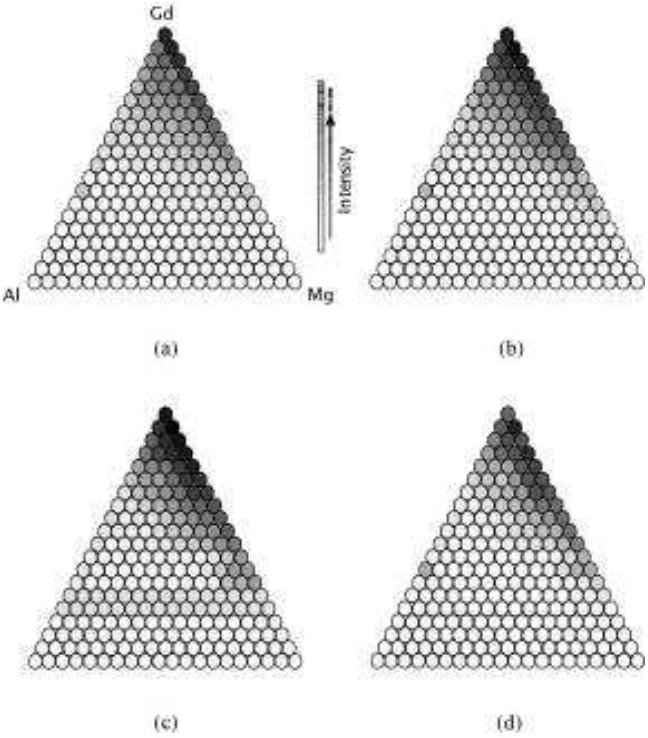

Figure 90: Red luminescent intensity under 246nm excitation radiation for a Al-Gd-Mg library [53]. The landscapes are for libraries fired at 1000°C (a), 1100°C (b), 1200°C (c), and 1300°C (d), which all produce trap-free landscapes. These are projections on a four-dimensional landscape with the fourth variable being firing temperature. Copyright 2004, The Electrochemical Society. Reproduced with permission.

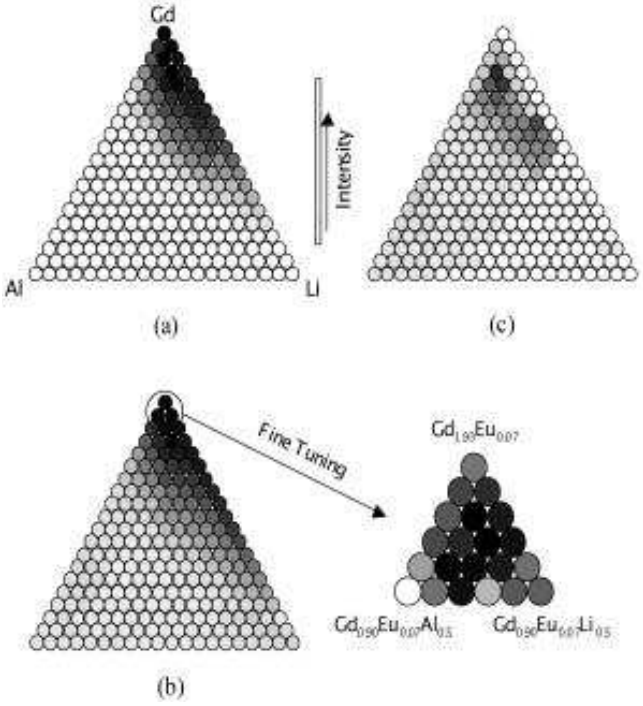

Figure 91: Red luminescent intensity under 246nm excitation radiation for a Al-Gd-Li library [53]. The landscapes are for libraries fired at 900°C (a), 1000°C (b), and 1100°C (c), and the landscapes at 900°C and 1000°C produce trap-free landscapes. These are projections on a four-dimensional landscape with the fourth variable being firing temperature. Copyright 2004, The Electrochemical Society. Reproduced with permission.

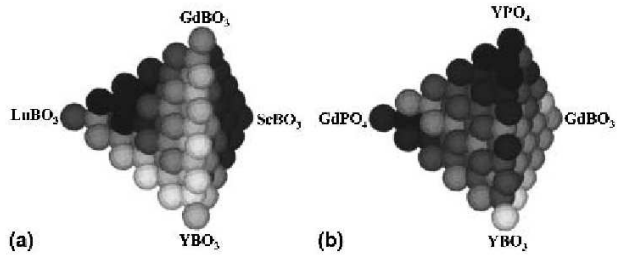

Figure 92: Red luminescent intensity under 146nm excitation radiation for a Gd-Sc-Y-Lu library (a) and a Y-Gd-P-B library (b) [54]. No subsets of the full landscapes are shown, but there are no obvious traps on these full landscapes. Copyright 2001, The Electrochemical Society. Reproduced with permission.

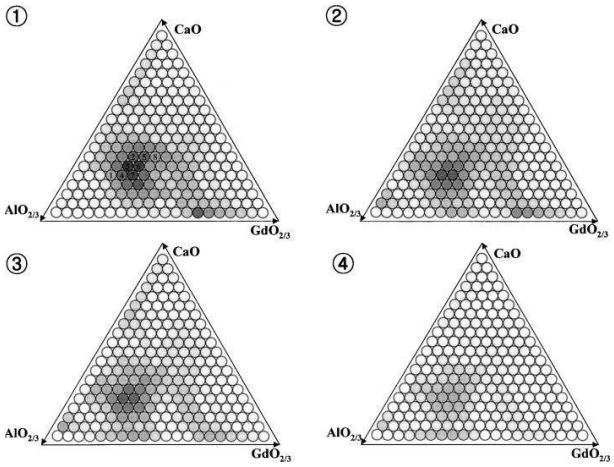

Figure 93: Green luminescent intensity under 147nm excitation radiation for a Gd-Ca-Al library fired at 1100°C (1), 1200°C (2), 1300°C (3), and 1400°C (4) [55]. All of the landscapes are trap-free. These are projections on a four-dimensional landscape with the fourth variable being firing temperature. Copyright 2002, The Electrochemical Society. Reproduced with permission.

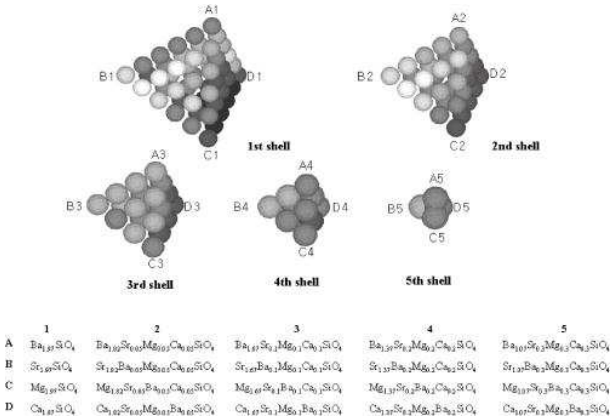

Figure 94: White luminescent intensity under 405nm excitation radiation for a Ba-Sr-Mg-Ca library [56]. The full landscape is labeled [A_1 B_1 C_1 D_1], and the remaining landscapes are subsets of the full landscape. Since the subset landscapes reveal no obvious traps, the full landscape appears to be trap-free. Reprinted with permission. Copyright 2005, American Institute of Physics.

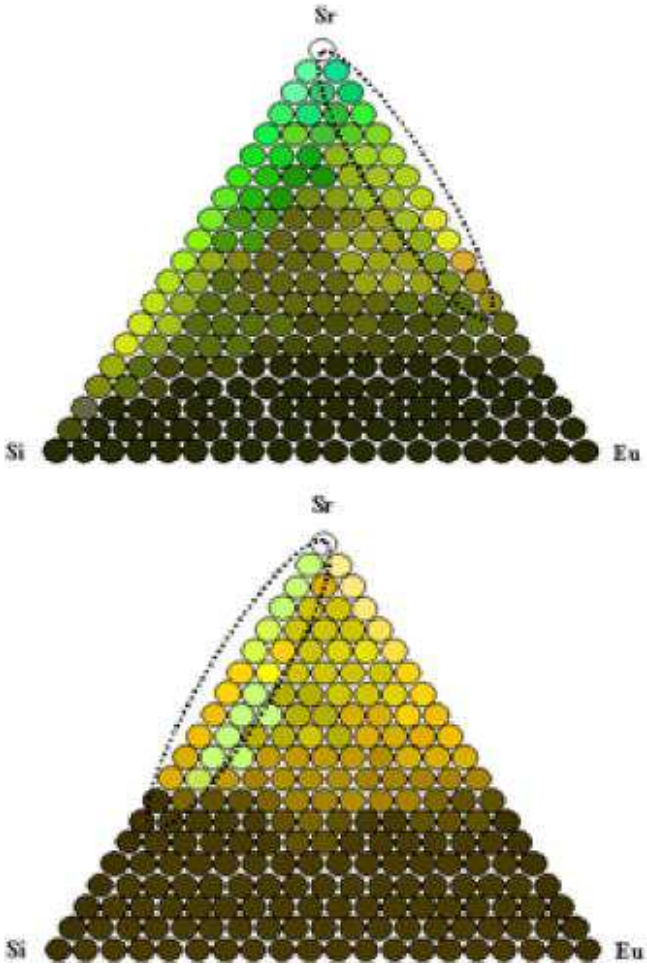

Figure 95: Fluorescence color of an Sr-Si-Eu library under excitation wavelength 405nm (a) and 465nm (b)[56]. The landscape in (a) has one optimal region on the Sr-Eu line; the yellow region on the Sr-Si line is not a trap because it is on the edge of the domain. The landscape in (b) has two disconnected orange regions and no obvious traps. Reprinted with permission. Copyright 2005, American Institute of Physics.

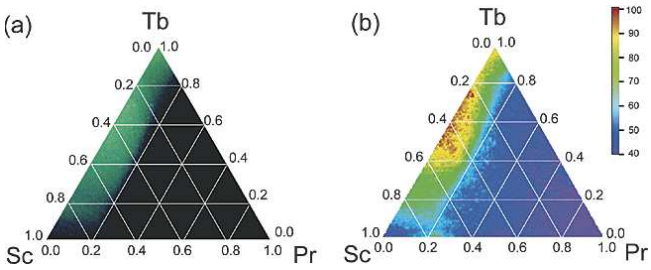

Figure 96: Color photograph of Sc-Tb-Pr library (a) from [58], and the luminescent intensity from the same library (b). Both landscapes are trap-free. Reprinted with permission. Copyright 2004 American Chemical Society.

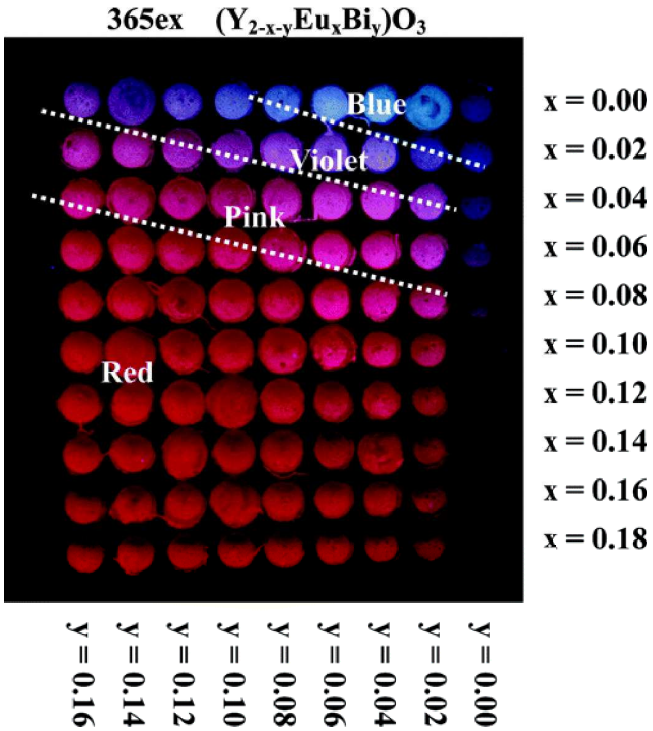

Figure 97: Color photograph of fluorescence from a Y-Eu-Bi library [59]. The color on the landscape varies monotonically from red through pink and violet to blue across the composition space. Reprinted with permission. Copyright 2007 American Chemical Society.

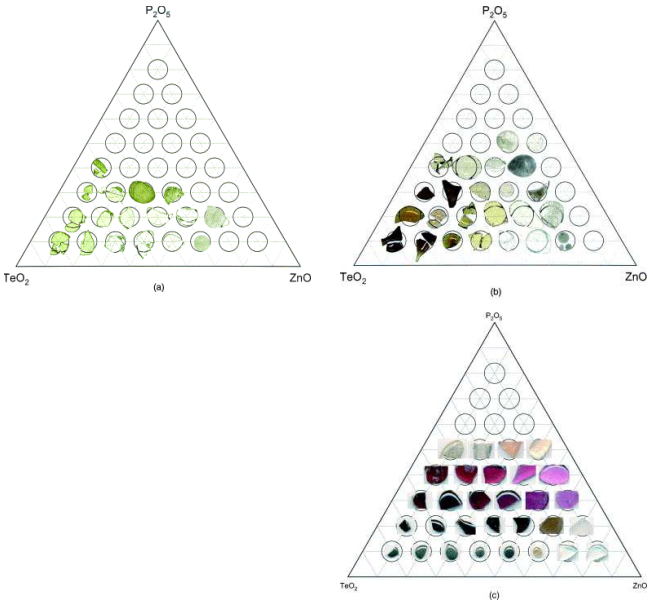

Figure 98: Glass color for P-Te-Zn library batch-melted at 900°C (a), 1000°C (b), and 1100°C (c) [60]. All landscapes show monotonic variation of glass color with composition. Reprinted with permission from Elsevier. Copyright 2003.

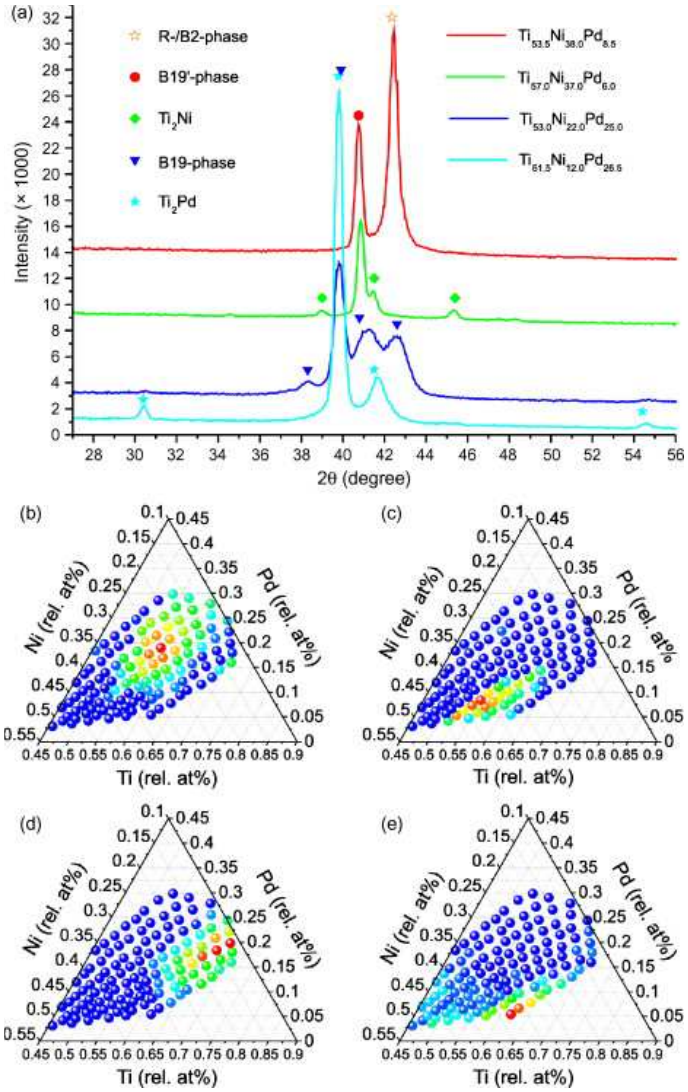

Figure 99: Sample XRD spectra (a) and landscapes of spectral peak intensity versus composition of a Ni-Ti-Pd library for Bragg peaks at $2\theta = 38.35°$ (b), $2\theta = 40.75°$ (c), $2\theta = 30.5°$ (d), and $2\theta = 45.45°$ (e) [61]. Red denotes high intensity and blue denotes low intensity. All landscapes show one maximum (red) region. Reprinted with permission from Elsevier. Copyright 2007.

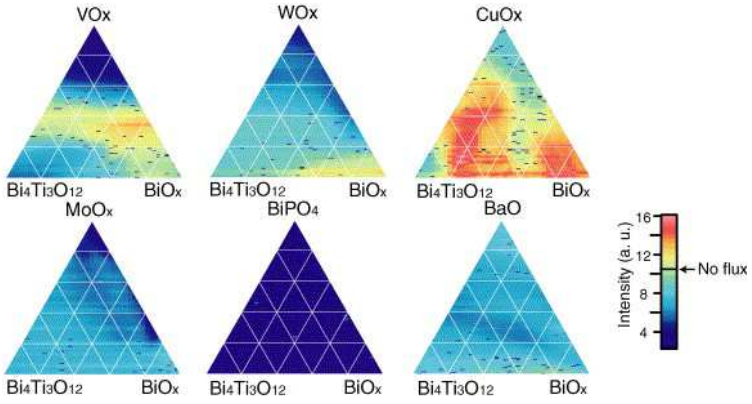

Figure 100: XRD spectral intensity of $Bi_4Ti_3O_{12}$ (0 0 1 4) crystal crystal versus composition of six ternary libraries [62]. The resulting landscapes appear trap-free for the V, W, and Cu libraries; the spectral intensity at all compositions for the remaining libraries is too low to determine if the landscapes are trap-free. Reprinted with permission from Elsevier. Copyright 2006.

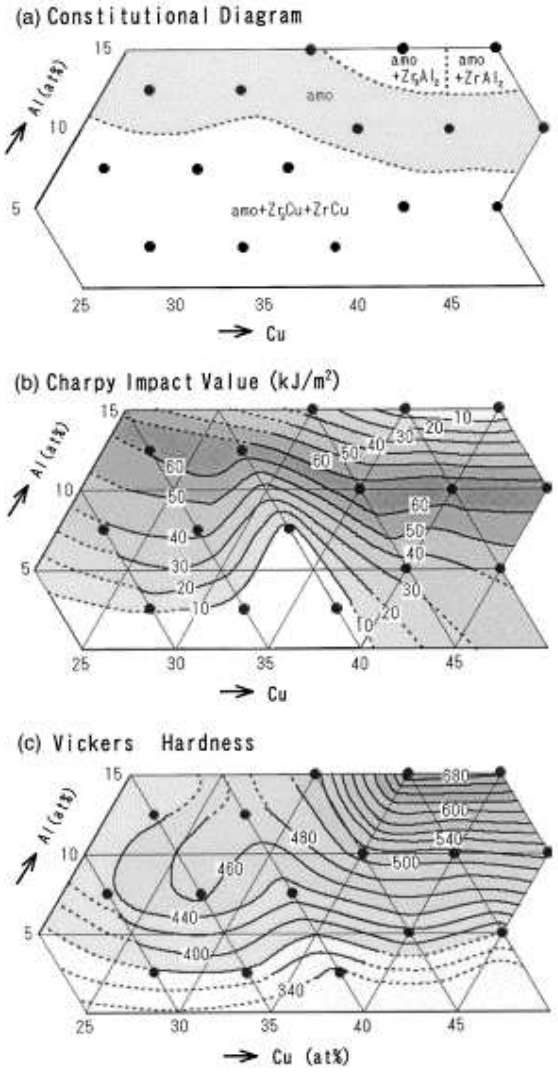

Figure 101: Phase constitutional diagram (a), and landscapes for Charpy impact parameter(b) and Vickers hardness parameter (c) for a Zr-Cu-Al library [63]. The landscapes in (b) and (c) are trap-free, and the landscape (b) contains an optimal level set. Reprinted with permission from Elsevier. Copyright 2003.

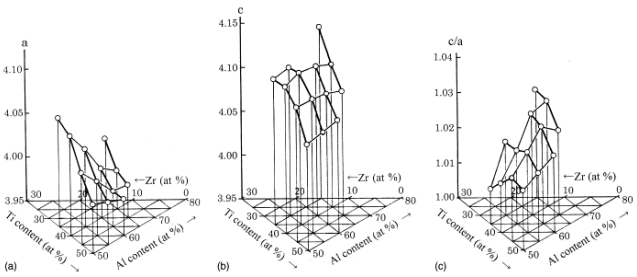

Figure 102: Lattice parameters a (a), c (b) and c/a (c) for an Al-Ti-Zr library [64]. The landscapes are trap-free over the small measured region of composition space. Reprinted with permission from Elsevier. Copyright 2004.

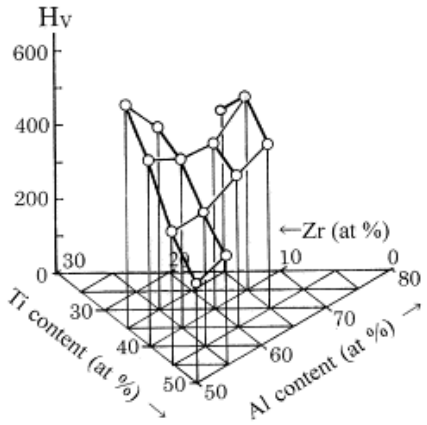

Figure 103: Vickers hardness parameter for Al-Ti-Zr library [64]. The landscapes are trap-free over the small measured region of composition space. Reprinted with permission from Elsevier. Copyright 2004.

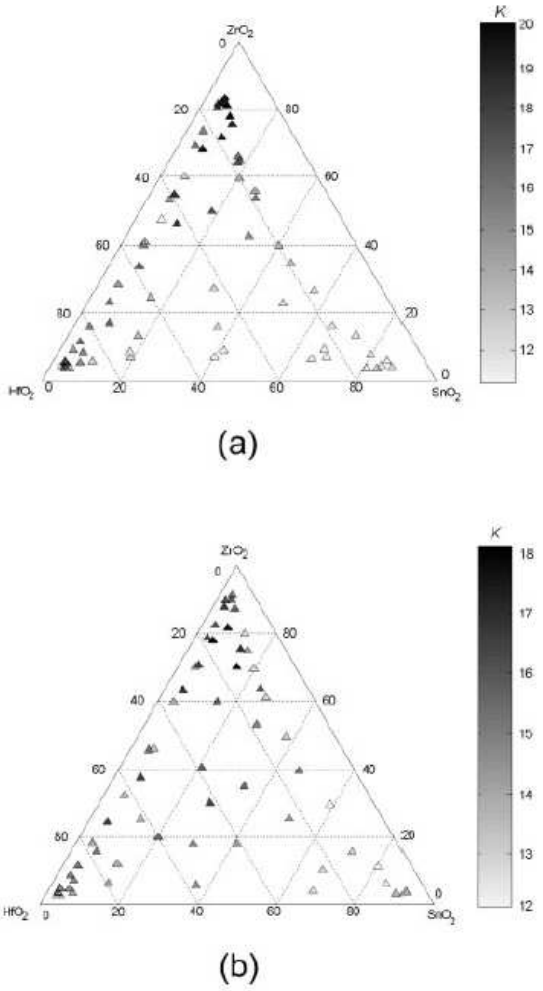

Figure 104: Dielectric constant κ versus material composition of Zr-Hf-Sn oxide library [66] deposited at 400°C (a) and 500°C (b). The landscape is trap-free and the area in the ZnO_2-rich region of both landscapes (a) and (b) constitutes a level set with optimally high values of κ. These landscapes are projections on a four-dimensional landscape, with the fourth variable being deposition temperature.

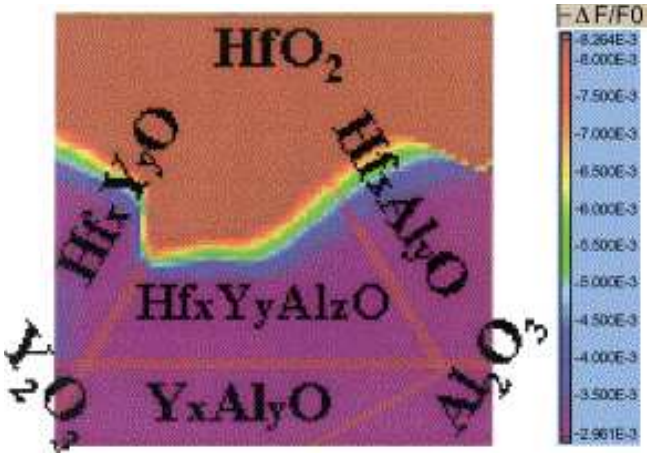

Figure 105: Frequency shift measured by a scanning microwave microscope versus composition in a Hf-Y-Al library [67]. The frequency shift is proportional to the dielectric constant, thus the Hf-rich region has the highest dielectric constant. This region corresponds to an optimal level set on the trap-free landscape. Reprinted with permission from Elsevier. Copyright 2004.

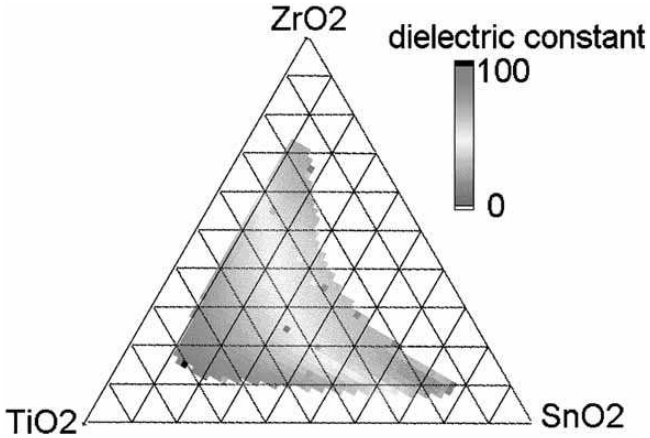

Figure 106: Dielectric constant as a function of composition for a Zr-Sn-Ti thin-film library [68]. The dielectric constant "is seen to monotonically increase as the fraction of TiO_2increases" [68], indicating a trap-free landcape. Copyright Wiley-VCH Verlag GmbH & Co. KGaA. Reproduced with permission.

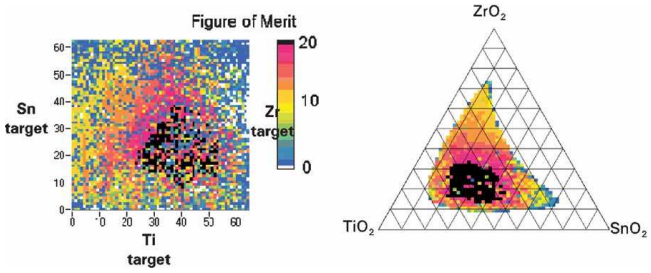

Figure 107: Figure of merit (maximal stored charge density) as a function of composition for the Zr-Sn-Ti library from [68]. This property produced a trap-free landscape. Copyright Wiley-VCH Verlag GmbH & Co. KGaA. Reproduced with permission.

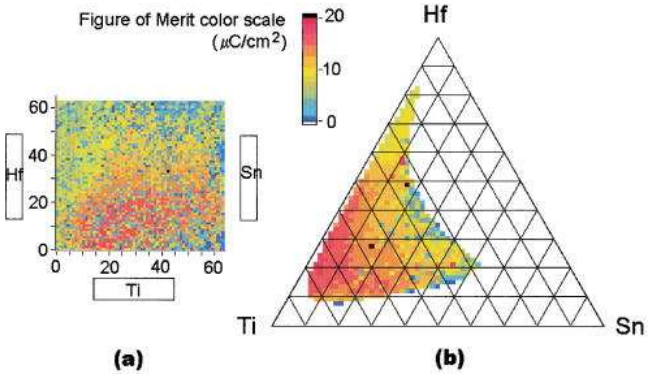

Figure 108: Figure of merit (maximal stored charge density as a function of composition for a Hf-Sn-Ti library [69]. Like the previous library for the same property in Figure 107, this also produces a trap-free landscape. Reprinted with permission. Copyright 1999, American Institute of Physics.

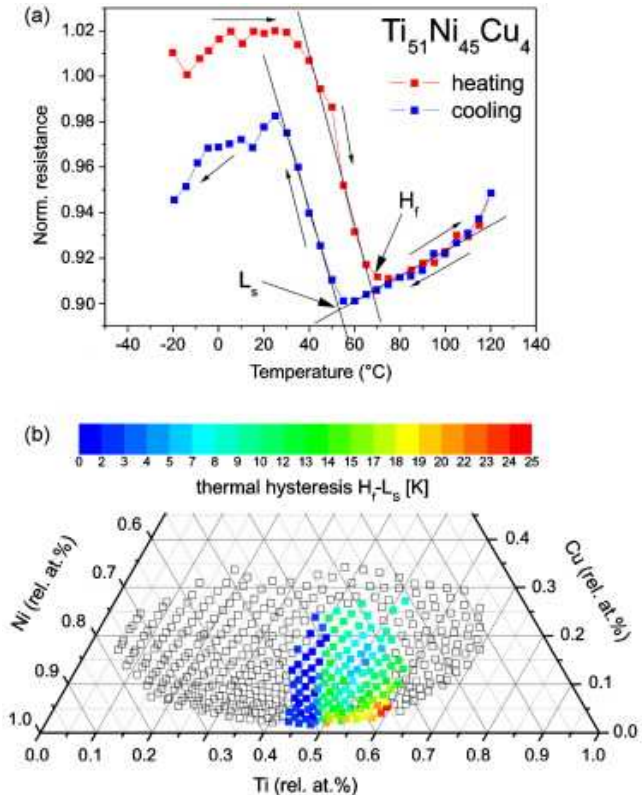

Figure 109: Heating/cooling curves of resistivity (a) and thermal hysteresis of resistivity versus material composition for a thin-film Ti-Ni-Cu library (b) [71]. The hysteresis property is defined as the difference in temperature between the heating and cooling curves in the linear region of Figure (a). The hysteresis landscape is trap-free for the region of composition space that undergoes a phase transition during the heating/cooling process. Reprinted with permission from Elsevier. Copyright 2008.

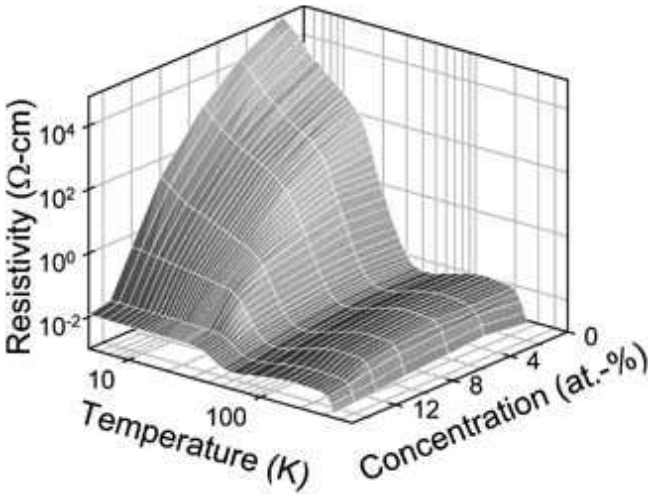

Figure 110: Resistivity versus Temperature and total doping concentration ($p_{Co} + p_{Mn} + p_{Ge}$) [72]. The resulting landscape has no traps. Copyright Wiley-VCH Verlag GmbH & Co. KGaA. Reproduced with permission.

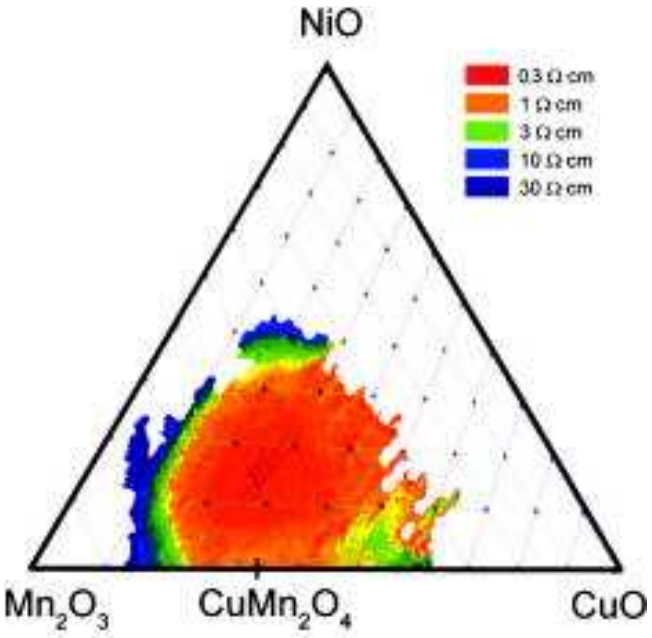

Figure 111: Conductivity map (i.e., measured property is resistivity) versus composition for a Mn-Ni-Cu thin-film library [73]. The landscape contains a large maximal region (in red), which the authors describe as "two connected regions of high conductivity" [73], indicating the presence of an optimal level set. Reprinted with permission. Copyright 2005, American Institute of Physics.

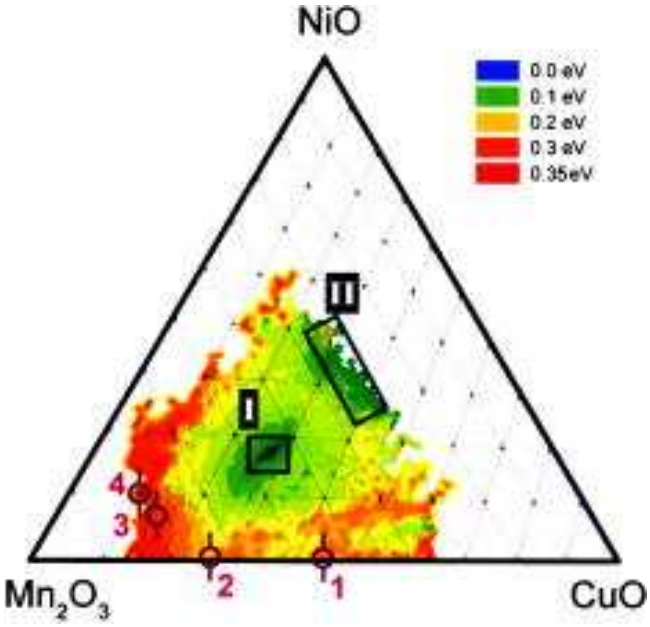

Figure 112: Thermal activation energy of conduction for the Mn-Ni-Cu library [73]. This landscape contains two disconnected maxima marked by I and II and appears to contain a sub-optimal maximal region in the lower right portion of the measured domain. Reprinted with permission. Copyright 2005, American Institute of Physics.

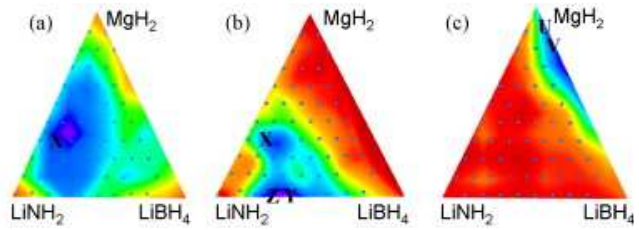

Figure 113: Hydrogen capacity of a $LiNH_2$-MgH_2-$LiBH_4$ material library at the first desorption (220°C, (a)), the second desorption (after rehydriding) (285°C, (b)), and the third desorption w(350°C,(c)) [75]. The landscape for first desorption is clearly trap-free, and the landscape for the second desorption contains two optimal regions marked by X and Y-Z. The landscape for the third desorption is trap free but has a different maximum. The landscape is trap-free. Reprinted with permission from Elsevier. Copyright 2007.

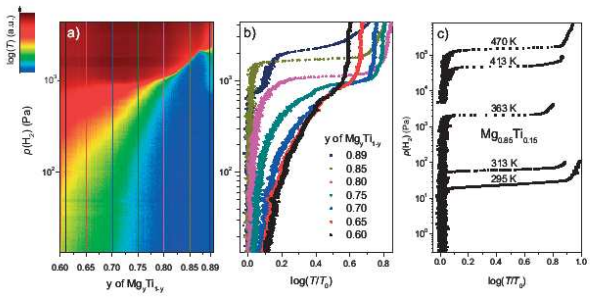

Figure 114: (a) Optical transmission (proportional to H_2 concentration) versus Mg content and pressure of H_2 [76]. (b) and (c) are one-dimensional curves on this landscape. Copyright Wiley-VCH Verlag GmbH & Co. KGaA. Reproduced with permission.

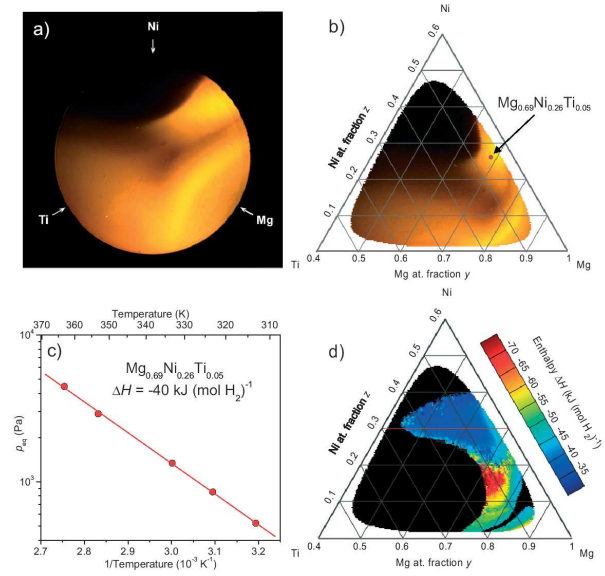

Figure 115: Optical transmission (proportional to amount of H_2 bound) for a Mg-Ti-Ni library from experimental photograph (a), same data mapped onto ternary phase diagram (b), a sample van't Hoff plot used to determine ΔH of binding H_2 (c), and ΔH of binding H_2 versus material composition (d) [76]. The landscape in part (d) is trap-free. The black regions on (d) correspond to compositions for which ΔH could not be calculated, and the remaining regions show a trap-free landscape. Copyright Wiley-VCH Verlag GmbH & Co. KGaA. Reproduced with permission.

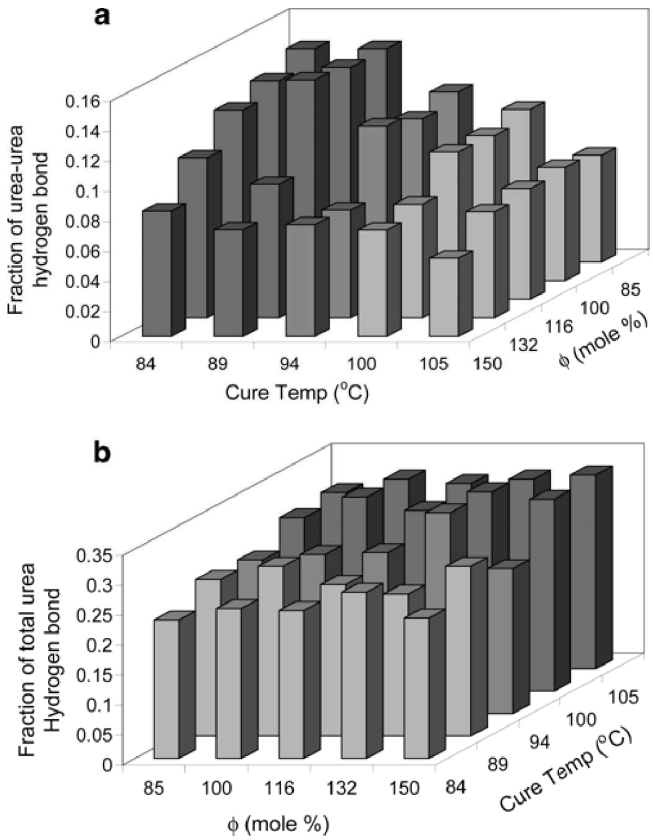

Figure 116: Fraction of urea-urea hydrogen bonding (a) and fraction of total hydrogen bonding (b) versus temperature and chain extender composition (ϕ) for a segmented poly-(urethane-urea) library [77]. The two landscapes show clear monotonic trends, considering a reasonable level of experimental noise. Reprinted with permission. Copyright 2004 American Chemical Society.

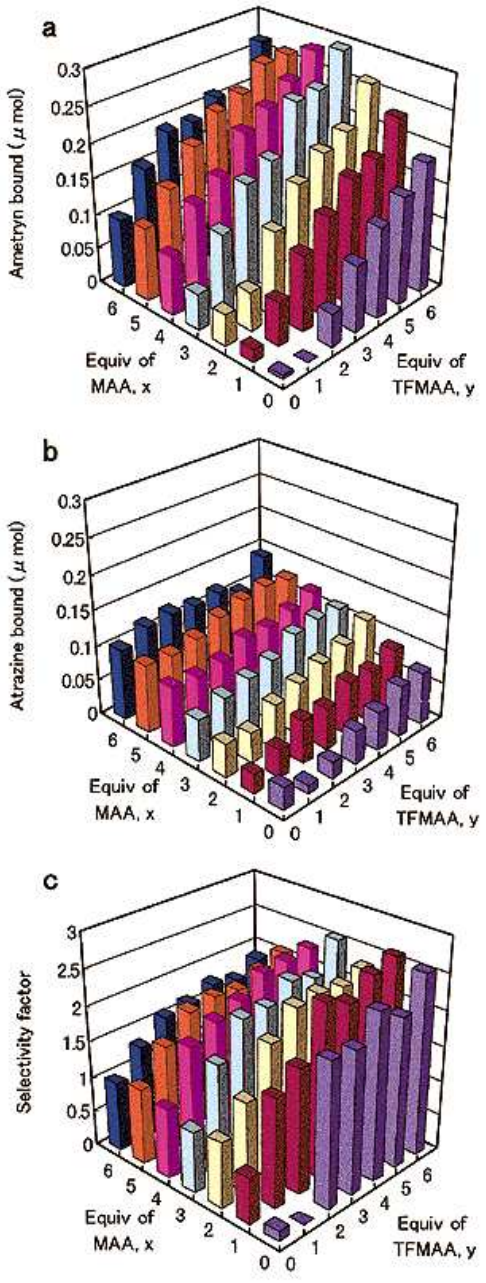

Figure 117: Binding and selectivity landscapes for ametryn-imprinted MAA-TFMAA polymer compositions [78]. Binding to ametryn (a) is stronger than binding to azetrine (b), as expected based on the imprinting; both landscapes are trap-free. The selectivity (relative amount of ametryn versus azetrine bound) (c) landscape is also trap-free. Reprinted with permission. Copyright 1999 American Chemical Society.

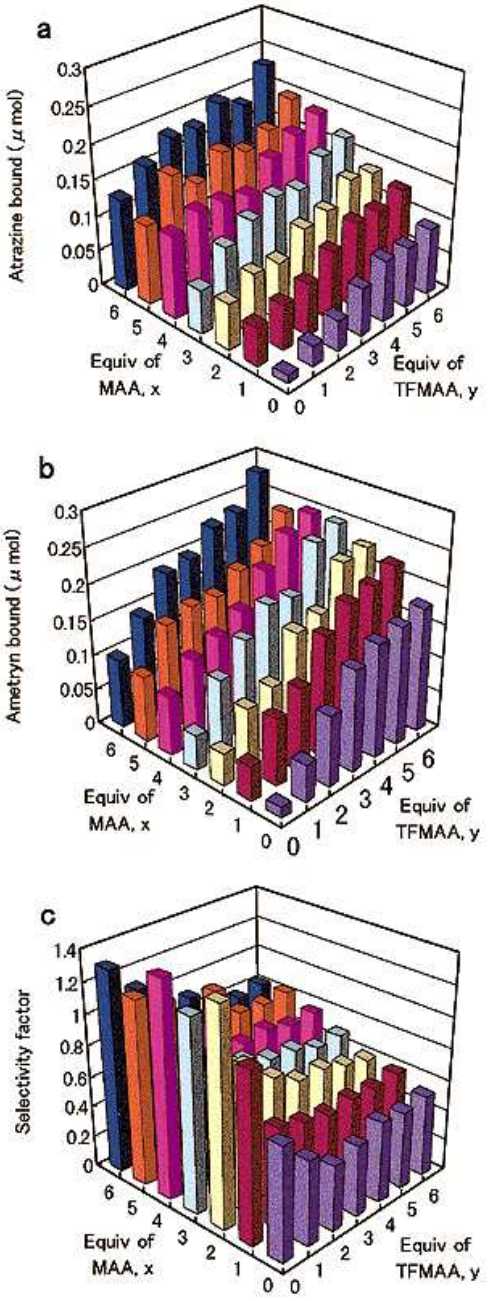

Figure 118: Binding and selectivity landscapes for azetrine-imprinted MAA-TFMAA polymer compositions [78]. Binding to ametryn (a) is weaker than binding to azetrine (b), as expected based on the imprinting; both landscapes are trap-free. The selectivity (relative amount of azetrine versus ametryn bound) (c) landscape is also trap-free. Reprinted with permission. Copyright 1999 American Chemical Society.

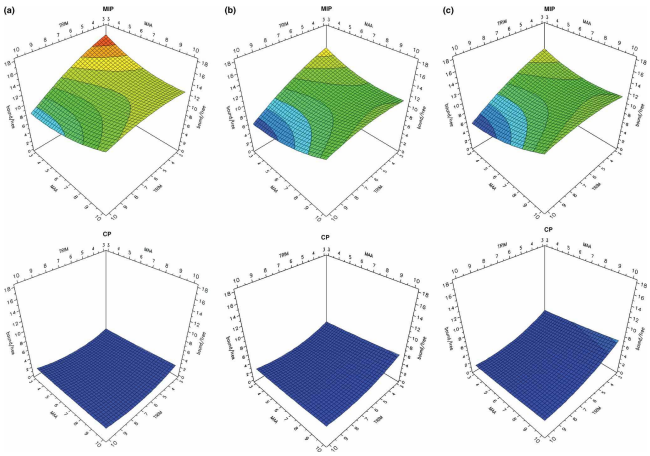

Figure 119: Binding of propranolol to MAA-TRIM polymer libraries imprinted with propranolol (top row) and Boc-L-Phe-OH (bottom row) [79]. The landscapes were measured at acetonitrile amounds of 3mL (a), 5.5mL (b), and 8mL(c). The plots are interpolated surfaces from the experimental data, and are all trap-free. Copyright Wiley-VCH Verlag GmbH & Co. KGaA. Reproduced with permission.

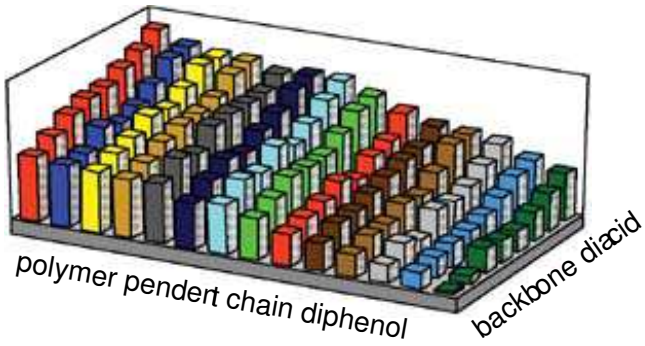

Figure 120: Glass transition temperature for polymers with a diacid backbone and diphenol pendent chains (Figure 4 from [81]). The landscape is ordered by the size of the diacid and diphenol components, resulting in a trap-free landscape. This result suggests that molecular size of the monomer units constitutes a good chemometric (rule) for determining the glass transition temperature property. Copyright Wiley-VCH Verlag GmbH & Co. KGaA. Reproduced with permission.

X_1 label	moiety	X_2 label	moiety
1	-C_6H_5	1	-CF_3
2	-OH	2	-*i*pr
3	-NH_2	3	-Cl
4	-$N(CH_3)_2$	4	-*n*pr
5	-CH_3	5	-OH
6	-*t*bu	6	-CH_2Cl
7	-$CHCH_2$	7	NH_2
8	-CH_2CH_3	8	-CH_2CH_3
9	-CH_2Br	9	-*t*bu
10	-OCH_2CH_3	10	-$N(CH_3)_2$
11	-OCH_3	11	-C_6H_5
12	-*i*pr	12	-OCH_2CH_3
13	-Cl	13	-OCH_3
14	-CH_2Cl	14	-$CHCHCH_3$
15	-*n*pr	15	-CH_3

Table 1: Integer labels for chemical moieties on the carbonyl scaffold depicted in Figure 9 of the main article.

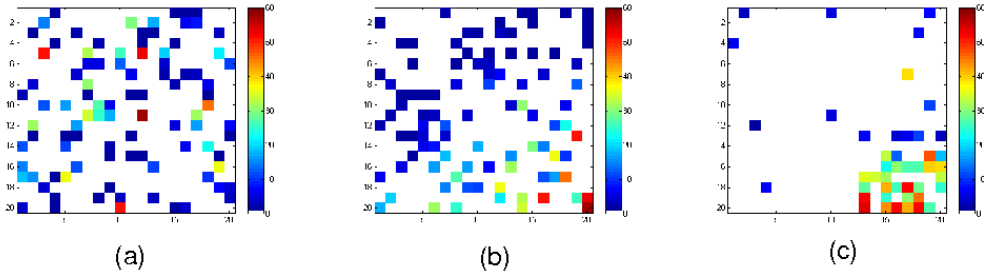

Figure 121: Percentage conversion for glycidil ether synthesis catalyzed by a library of epoxide hydrolase mutants from *Aspergillus niger* [82]. 95 mutants were randomly sampled on two positions of the enzyme's active site, giving rise to a rugged property (percentage conversion) landscape (a), which was reordered into a smooth landscape (b). Guided by the reordered landscape, 45 additional mutants were synthesized (most at the bottom right corner of (b) and some randomly at other locations). The results (c) clearly demonstrated the predictability of the reordering method.

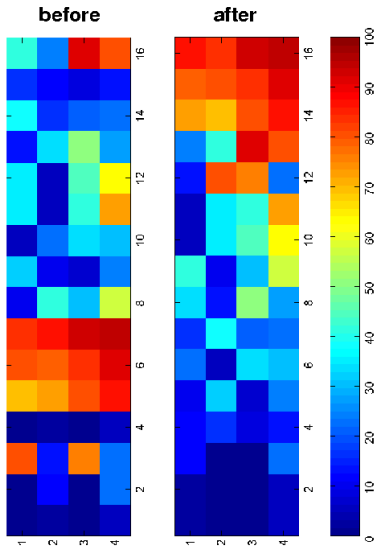

Figure 122: Percentage conversion for the formation of cyclohexenyl acetate using a library of palladium bidentate catalysts. The two substituion sites of the catalysts have 4 and 16 distinct functional groups, respectively. Left: before reordering. Right: after reordering. The reordered landscape is nearly trap-free. [83].

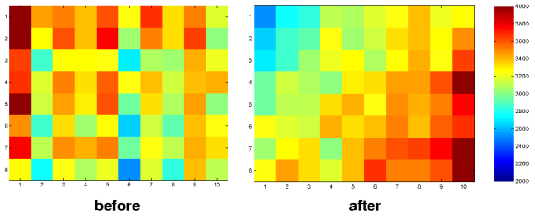

Figure 123: Reordering of a di-substituted triazine library that can effectively inhibit the early stage aggregation of the Alzheimer's peptide Aβ2 [84]. The property being measured is the fluorescence level of a fusion green fluorescence protein (GFP), which quantitatively indicates the triazine's ability to block Aβ2 aggregation. Left: before reordering. Right: after reordering. The reordered landscape is nearly trap-free.

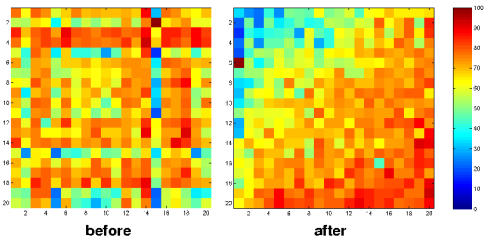

Figure 124: Reordering of a synthetic hexapeptide library where all amino acids on the first two positions were completely sampled [85]. Each peptide was measured for the percentage inhibition of the crude rate brain homogenates's binding to its natural receptor. Left: Before reordering. Right: After reordering. This landscape shows a trap-free trend with some outliers, which may be due to the fact that only two of the six amino acid sites were varied, so this landscape in fact represents a two-dimensional projection on a six-dimensional space.